

Ice Adhesion Strength and Durability of Nanostructured Coatings for Aerospace Applications

Am Fachbereich Maschinenbau
der Technischen Universität Darmstadt
zur
Erlangung des Grades eines Doktor-Ingenieurs (Dr.-Ing.)
genehmigte

Dissertation

vorgelegt von

Alexandre Laroche, M.A.Sc.

aus Montreal, Kanada

Berichterstatter:	Prof. Dr.-Ing. J. Hussong
Mitberichterstatter:	Prof. Dr. Ali Dolatabadi
Tag der Einreichung:	17.08.2021
Tag der mündlichen Prüfung:	05.10.2021

Darmstadt 2021
D17 (Diss. Darmstadt)

Alexandre Laroche:
Ice Adhesion Strength and Durability of Nanostructured Coatings for
Aerospace Applications

Darmstadt, Technische Universität Darmstadt
Jahr der Veröffentlichung der Dissertation auf TUprints: 2021
URN: urn:nbn:de:tuda-tuprints-199338
URL: <https://tuprints.ulb.tu-darmstadt.de/id/eprint/19933>
Tag der mündlichen Prüfung: 05.10.2021



Veröffentlicht unter CC BY-SA 4.0 International:
Namensnennung – Weitergabe unter gleichen Bedingungen
<https://creativecommons.org/licenses/by.nc.nd/4.0>

*For Berj, Taunte Sarah, Taunte Marie,
and for Clara,
and for Ruby, Cat, Grace, and Daniel,*

Abstract

The aerospace industry has been focused on improving the efficiency of its ice protection systems, also by supporting the systems with icephobic coatings, but lacks suitable candidate materials and processes for manufacturing such surfaces. To be able to protect its next generation aircraft and light rotorcraft without ice protection systems from icing, the industry requires research into durable and effective icephobic coatings.

In this thesis, progress toward the implementation of icephobic materials for aerospace applications has been made on two fronts: on new methods for characterizing the performance of icephobic coatings, and on the exploration of a multitude of candidates based on different working principles in terms of durability and ice adhesion strength.

The characterization of icephobic performance in this thesis consisted of durability tests and ice adhesion strength measurement. The principle qualitative durability test used was accelerated rain erosion. A step was added to the conventional test method to evaluate the change in surface functionality after erosion. Ice adhesion strength measurement was performed using an in-situ vibrating cantilever method in an icing wind tunnel.

To enhance the vibrating cantilever ice adhesion test method, an uncertainty analysis was performed according to the Guide for the Expression of Uncertainty in Measurement (GUM) for the first time. The parameter that contributed most to this uncertainty was the Young's modulus of ice. A test method was herein developed for the measurement of the Young's modulus of ice using the unmodified vibrating cantilever test method. For demonstration, the method was used for measuring the modulus of 4 different ice types produced by

the conditions used for ice adhesion strength testing. The measured Young's moduli were between 5 – 7 GPa, between 60-80% of the literature value of 9 GPa.

The superhydrophobic surfaces tested for durability and ice adhesion were prepared on aluminum alloy and stainless-steel alloy substrates. The most durable of these surfaces proved to be least icephobic, as shown by its high ice adhesion strength in comparison to non-superhydrophobic surfaces. Superhydrophobic surfaces prepared on titanium substrates showed improved icephobicity when a nano-scale roughness was present on a micro-scale roughness. This result led to the conclusion that micro-scale roughness provided enhanced durability for a nano-scale roughness which enhanced icephobicity. The icephobicity of these surfaces also relied on a hydrophobic surface chemistry, which is known to degrade on exposure to UV radiation. To address this issue, silicone nanofilament coatings with intrinsic nano-scale roughness, a hydrophobic surface chemistry, and resistance to UV were considered.

Silicone nanofilament coatings prepared on polyester fabrics were exposed to a water droplet cloud in a high-speed airflow to test their durability. Water contact angle and roll-off-angle were measured following progressively aggressive exposure (increasing airspeed). The coating was superhydrophobic until exposure to water droplet clouds in an airstream at a speed of 120 m/s. A coated fabric was also exposed to icing conditions, whereby it remained hydrophobic for 3 icing/de-icing cycles, and locally superhydrophobic in the leading-edge region. This result showed that the coating was durable enough for the exterior of light aircraft, and for controlled ice adhesion tests.

The silicone nanofilament coating was then grown on aluminum alloy and titanium alloy, resulting in nanostructured superhydrophobic coatings. As a novel characterisation of this

coating, ice adhesion strength measurements were performed, resulting in a 50-70% reduction in ice adhesion strength than the untreated surface on aluminum substrates, and a reduction between 70-80% compared to the untreated surface on titanium substrates. The infusion of lubricant into the nanoporous coating on titanium resulted in the 80% reduction in ice adhesion strength and was consistent for 4 icing/de-icing cycles in each of the 4 icing conditions tested. Silicone nanofilament coatings are therefore suitable for aircraft applications and provide a durable, easy ice-release functionality.

Kurzfassung

Die Luft- und Raumfahrtindustrie arbeitet daran, die Effizienz ihrer Vereisungsschutzsysteme zu verbessern, auch indem sie die Systeme mit eisabweisenden Beschichtungen schützt. Es fehlt jedoch an geeigneten Materialien und Verfahren für die Herstellung solcher Oberflächen. Um die nächste Generation von Flugzeugen und leichten Drehflüglern ohne Eisschutzsysteme vor Vereisung schützen zu können, muss die Industrie nach dauerhaften und wirksamen eisabweisenden Beschichtungen forschen.

In dieser Arbeit wurden an zwei Punkten Fortschritte auf dem Weg zu eisabweisenden Materialien für die Luft- und Raumfahrt erzielt: zum einen durch neue Methoden zur Charakterisierung der Leistungsfähigkeit von eisabweisenden Beschichtungen und zum anderen durch das Testen einer Vielzahl von Beschichtungen, die auf unterschiedlichen Funktionsprinzipien in Bezug auf Haltbarkeit und Eisadhäsionskraft basieren.

Die mechanische Beständigkeit von Oberflächen ist ein Hauptanliegen von Flugzeugkonstrukteuren. Daher wurden qualitative Haltbarkeitstests an superhydrophoben Oberflächen durchgeführt, die auf Aluminium- und Edelstahllegierungen hergestellt wurden. Anders als erwartet erwiesen sich einige superhydrophobe Oberflächen als weniger eisabweisend. Superhydrophobe Oberflächen, die auf Titansubstraten hergestellt wurden, zeigten eine bessere Eisabweisung, wenn eine Mikrostruktur mit einer nanoskaligen Struktur kombiniert wurde unter anderem weil eine mikroskalige Struktur die Haltbarkeit der nanoskaligen Struktur erhöht. Die Eisabweisung dieser Oberflächen beruhte auch auf einer hydrophoben Oberflächenchemie, die sich

jedoch bei UV-Strahlung verschlechtert. Um dieses Problem zu lösen, wurden Beschichtungen aus Silikon-Nanofilamenten mit nanoskaliger Struktur, einer hydrophoben Oberflächenchemie und UV-Beständigkeit untersucht.

Silikon-Nanofilament-Beschichtungen, die auf einem Polyestergewebe hergestellt wurden, wurden einer aerodynamischen Hochgeschwindigkeitsumgebung ausgesetzt. Der Wasserkontaktwinkel und der Abrollwinkel wurden unter zunehmend aggressiven mechanische Bedingungen gemessen und zeigten, dass die Beschichtung superhydrophob bleibt, bis sie Wassertropfenwolken in einem Luftstrom mit einer Geschwindigkeit von 120 m/s oder mehr ausgesetzt wurde. Ein beschichtetes Gewebe wurde auch Vereisungsbedingungen ausgesetzt, wobei es für 3 Vereisungszyklen mindestens hydrophob und im Bereich der Vorderkante lokal superhydrophob blieb.

Die Beschichtung aus Silikon-Nanofilamenten wurde dann auf Aluminium- und Titanlegierungen aufgewachsen, was zu nanostrukturierten superhydrophoben Beschichtungen führte. Erstmals wurde an diesen Beschichtung Messungen der Eisadhäsionskraft durchgeführt. Hier konnte jeweils eine 50-70% bzw. 70-80% reduzierte Eisadhäsionskraft im Vergleich zu einer unbehandelten Oberfläche auf Aluminiumsubstraten und Titansubstraten gemessen werden. Die Infusion von Schmiermittel in die nanoporöse Beschichtung auf Titan führte zu einer Reduktion der Eishaftung um 80 % und war für 4 Enteisungszyklen bei jeder der 4 getesteten Vereisungsbedingungen gleich.

Zur Verbesserung der Testmethode für die Eishaftung mit vibrierenden Auslegern wurde zum ersten Mal eine Unsicherheitsanalyse gemäß dem Leitfaden zur Angabe der Unsicherheit beim Messen (GUM) durchgeführt. Die typische Unsicherheit für einen einzelnen Datenpunkt der

Eishaftungsfestigkeit betrug 27 % mit einem Konfidenzintervall von 95 %. Der Parameter, der am meisten zu dieser Unsicherheit beitrug, war das Elastizitätsmodul des Eises. Im Folgenden wurde eine Prüfmethode zur Messung des Elastizitätsmoduls von Eis entwickelt, bei der die unveränderte Methode des vibrierenden Cantilever-Tests verwendet wurde. Um die Methode zu demonstrieren, wurde sie zur Messung des Elastizitätsmoduls von 4 verschiedenen Eistypen verwendet, die unter den für die Eishaftungsprüfung verwendeten Bedingungen hergestellt wurden. Die gemessenen Elastizitätsmodule lagen zwischen 5 und 7 GPa.

Acknowledgements

The grandest gratitude for the work in this thesis I give to Elmar Bonaccurso, who supervised the entirety of the work. He provided invaluable advice, both technical and managerial, that I hold with high value. After giving me the opportunity to carry out the work at Airbus, Elmar never failed to be responsive, insightful, and caring while giving me the freedom to be creative and satisfy my own scientific curiosities. I'd like to express gratitude to Jürgen Wehr who I see as a role model for management and creating a healthy, happy, working environment.

Much of what I learned during these few years came from Doris Vollmer. She provided me with a complementary perspective on scientific research that I will carry with me well into my career. Her level of dedication to helping her students succeed in their own individual way is unparalleled.

I would like to thank Frau Prof. Dr. Jeanette Hussong for agreeing to support me as an academic supervisor. I greatly appreciate the wholehearted effort she gave in helping me to improve this dissertation and for guiding me through the entire process. I look forward to future collaborations.

Ali Dolatabadi is one of the most valuable mentors/supervisors that I've had the pleasure to work for (during my master's degree) and with (during my doctorate). He and Dr. Hoa gave me the tools, facilities, and advice that could use to stand out as a research engineer. Then, Ali gave me the opportunity to grow my network and join the Airbus team, which led to the present work. He has

become a dear friend and colleague with whom I would love to continue working with.

There have been countless memorable team members at Airbus who contributed to making the experience so enriching. In particular, I'd like to thank my mentor, Vittorio Vercillo, and closest friends and team members, Norbert Karpen, Alexandre Bobillier, Javier Mayén Guillén, Simone Tonnichia and Simon Schelle. For their contributions to this work, their cooperation, and overall pleasure to work with. I'd like to thank Maria Grasso, Robin Wachsmann, and Linda Ritzen, who never failed to impress me with the quality of their work.

I'd like to thank all the project partners in Phobic2ICE and LubISS who provided expertise in surface modification and prepared samples for testing. In particular, Davide Bottone, who also helped to perform characterisation tests and whom I found to be an extraordinary scientific writing partner. I'd like to thank David Thompson for including us in the project with Mississippi State University and NASA.

Finally, I'd like to thank my family for encouraging me from afar and for continually giving me perspective and hope. I'd like to thank Dagmara, in particular, who stuck by my side for the long writing period, and who always gave me a means and reminder to take a break and enjoy life along the way.

This research was supported by the European Union's Horizon 2020 research and innovation programme under the Marie Skłodowska-Curie grant agreement No 722497 – LubISS. This work was also financially supported by the Canada and EU partnership project Phobic2Ice (NSERC CRDPJ 479633-15; CARIC EUCA-PHOBIC2ICE; EU G.A. 690819).

Nomenclature

Letter	Unit	Description
b	m	beam width
D	μm	droplet diameter
e	m	eccentricity of neutral axis with respect to interface
E	N/m^2	Young's Modulus
h	m	Thickness
l	m	length of cantilever
LWC	g/m^3	liquid water content
M	$\text{N}\cdot\text{m}$	bending moment
Ra	μm	average roughness
Rz	μm	average peak-to-peak roughness
T	$^{\circ}\text{C}$	temperature
t	s	time
V	m/s	airspeed
x	m	position along cantilever from fixed end
ε	m/m	strain
γ	N/m^2	surface tension
μ	cPs	kinematic viscosity
ν	-	Poisson's ratio
ρ	kg/m^3	density
σ	N/m^2	normal stress

Dimensionless Groups

Shorthand	Name	Formula	Description
Oh	Ohnesorge Number	$\frac{\mu}{\sqrt{\rho\gamma D}} = \frac{\sqrt{We}}{Re}$	Ratio of particle viscosity to inertia and surface tension.
Re	Reynolds Number	$\frac{\rho VD}{\mu}$	Ratio of particle inertia to viscosity.
St	Stokes Number	$\frac{tV}{D}$	Ratio of characteristic time of a particle to the characteristic time of a fluid flow over an obstacle.
We	Weber Number	$\frac{\rho VD^2}{\gamma}$	Ratio of particle inertia to surface tension.

Subscripts

Subscript	Description
1	Body or material 1 in a generic bi-material model. Interchangeable with subscript “ice”.
2	Body or material 2 in a generic bi-material model. Interchangeable with subscript “substrate”.
Ice	Ice material or body
Sub	Shortened designation of “substrate”
Substrate	Substrate material or body, either aluminum, titanium, or steel

Abbreviations

Abbreviation	Description
AA	Aluminum alloy
AoA	Angle of attack
CA	Contact angle
HVOF	High velocity oxygen fuel
IAS	Ice adhesion strength
IR	infrared
IWT	Icing wind tunnel
NACA	National Advisory Committee for Aeronautics (NASA after 1968)
ns	nanosecond
OAD	Oblique angle deposition
PFPE	Perfluoropolyether
RoA	Roll-Off Angle
SNF	Silicone nanofilaments
SS	Stainless steel
UV	ultraviolet

Contents

Abstract.....	i
Kurzfassung.....	v
Acknowledgements.....	ix
Nomenclature.....	xi
Dimensionless Groups	xii
Subscripts.....	xiii
Abbreviations	xiii
List of Figures.....	xix
List of Tables	xxix
1 Introduction	1
1.1 Dangers of Ice in General	1
1.1.1 Atmospheric Icing	3
1.2 Dangers of Ice Forming on Aircraft	5
1.3 Ice Protection Systems used on Aircraft	8
1.3.1 Ways to Improve Ice Protection System Efficiency & Efficacy	10
1.4 Challenges of Implementing Functional Surfaces for Ice Protection in Aerospace	11
2 State of the Art.....	15
2.1 Surfaces commonly used on Aircraft.....	15
2.2 Strategies for Making Icephobic Surfaces.....	17
2.2.1 Structured Solid Surfaces (Superhydrophobic Surfaces)	17

2.2.2 Compliant Surfaces.....	22
2.2.3 Lubricant Infused Surfaces.....	24
2.3 Qualification of Icephobic Surfaces	26
2.3.1 Mode I Tests	29
2.3.2 Mode II Tests	31
2.3.3 Mixed-Mode Flexure Tests	34
2.4 Outline of the Thesis.....	37
3 Materials and Methods	41
3.1 Surfaces & Substrates	41
3.1.1 Substrate Materials and Reference Surfaces	42
3.1.2 Hard Textured and Modified Polyurethane Surfaces	46
3.1.3 Silicone Nanofilament Coatings	54
3.2 Primary Characterisation	60
3.2.1 Contact Angle Measurement	60
3.2.2 Surface Roughness Measurement.....	60
3.2.3 Scanning Electron Microscopy	61
3.3 Icephobicity Characterisation.....	61
3.3.1 Icing Wind Tunnel	62
3.3.2 Ice Adhesion Test.....	68
3.4 Durability Characterisation	78
3.4.1 Water Droplet Cloud Exposure.....	79
3.4.2 Rain Erosion Exposure	81
4 Results & Discussion	85
4.1 Qualitative Testing of Rain Erosion Resistance.....	86

4.2	Ice Adhesion on Reference and Modified Aircraft Paint	91
4.3	Ice Adhesion on Reference and Textured Hard Surfaces	94
4.4	Influence of Ice Thickness on Ice Adhesion Strength Measurement	102
4.5	Uncertainty Analysis of the Ice Adhesion Test Method	106
4.5.1	Uncertainty Model.....	106
4.5.2	Standard Uncertainty of Strain	108
4.5.3	Standard Uncertainty of Substrate Dimensions	110
4.5.4	Standard Uncertainty of Ice Thickness.....	111
4.5.5	Evaluation of Combined Standard Uncertainty	113
4.6	Determining the Young’s Modulus of Ice Using the Ice Adhesion Test Setup.....	116
4.7	Influence of Surface Roughness on Ice Adhesion Strength.....	121
4.8	Durability of a Silicone Nanofilament Coating (SNF) on Textiles in Icing Conditions	127
4.9	Ice Adhesion and Durability of Silicone Nanofilament Coatings on Aircraft Alloys	134
4.9.1	Dry Silicone Nanofilament Coatings on Aluminum	136
4.9.2	Dry and Lubricant-Infused Silicone Nanofilament Coatings on Titanium	140
5	Summary and Conclusions	145
5.1	Improvements to the Method of Measurement of Ice Adhesion Strength.....	145
5.2	Identification of a suitable Icephobic Surface for Aerospace.....	146
5.3	Outlook.....	148

6	Bibliography	151
	Appendix A - Determination of Thermal Stress in the Ice Adhesion Test.....	173
	A.1 Context:	174
	A.2 Results:	174
	A.3 Summary:.....	177

List of Figures

- Figure 1: Photographs of (a) a frozen lake, (b) a flowing stream of water through a snowy forest, and (c) a sidewalk covered in clear ice..... 2
- Figure 2: Dry growth of rime ice (left) and wet growth of glaze ice (right). Redrawn from (Makkonen, 2000) and reprinted with permission from (Laroche, Grasso, et al., 2020). Copyright© 2020, John Wiley & Sons..... 4
- Figure 3: Illustration of a horned ice accretion on an airfoil where there is ice present on low angle of incidence areas and very little or no ice present on high angle of incidence areas. 5
- Figure 4: Rime ice left-over on a wing leading edge after de-icing boot (black component) activation. Picture reproduced from (Transportation Safety Board of Canada, 2014)..... 9
- Figure 5: Water drop on a solid surface and definition of the contact angle. Redrawn from (Zisman, 1964). Reprinted with permission from (Laroche, Grasso, et al., 2020). Copyright© 2020, John Wiley & Sons..... 19
- Figure 6: Wetting models on rough surfaces. (a) Wenzel model showing a droplet in contact with a complete surface profile, and (b) the Cassie-Baxter wetting model showing a droplet supported by asperities in the surface profile. 19
- Figure 7: Schematic example of a water droplet on a lubricant-infused textured surface, showing three possible lubrication states: overfilled, filled, or underfilled..... 25

Figure 8: General loading conditions used to measure interfacial bond strength between ice and a substrate. Direction of applied load shown by arrow, and interface shown by a red line. Reprinted with permission from (Laroche, Grasso, et al., 2020). Copyright© 2020, John Wiley & Sons.29

Figure 9: Tensile ice adhesion test method using an embedded pull-rod. Reprinted with permission from (Laroche, Grasso, et al., 2020). Copyright© 2020, John Wiley & Sons.30

Figure 10: Mode I ice adhesion test for the measurement of adhesion of impact ice in-situ. (M. Pervier, 2012). Reprinted with permission from (Laroche, Grasso, et al., 2020). Copyright© 2020, John Wiley & Sons.31

Figure 11: Rudimentary pusher test for Mode II ice adhesion tests. Adapted from (Golovin, 2017). Reprinted with permission from (Laroche, Grasso, et al., 2020). Copyright© 2020, John Wiley & Sons.32

Figure 12: Pusher test designed for testing the adhesion of impact ice to a surface in-situ. Adapted from (M. Pervier, 2012). Reprinted with permission from (Laroche, Grasso, et al., 2020). Copyright© 2020, John Wiley & Sons.33

Figure 13: Configurations of the bending test for measuring ice adhesion strength, (a) controlled applied force (C. Laforte, 2001), (b) vibrating beam with strain sensor at interface (Javan-Mashmool et al., 2006a), (c) vibrating beam with strain sensor at interface (Akitegetse et al., 2008), (d) vibrating beam with two strain gauges on substrate near interface (Hassan et al., 2010), and (e) vibrating beam with

single strain gauge on substrate behind interface (Tobias Strobl et al., 2013).....	35
Figure 14: SEM image of self-organized TiO ₂ nanotubes on a Ti6Al4V substrate.	44
Figure 15: Laser pattern produced by a nanosecond infrared laser on an aluminum substrate with (a) an SEM image above a surface roughness profile, and (b) the areal surface roughness profile taken by confocal microscope. Reprinted with permission from (V. J. Rico et al., 2019). Copyright © 2019, American Chemical Society.	47
Figure 16: SEM images of SS_SPS_SA prepared by CU, where (a) and (b) are top views, and (c) and (d) are view of the cross-section. Reprinted with permission from (Sharifi et al., 2016). Copyright© 2016, Elsevier.	49
Figure 17: PECVD coating stack produced by PM over the SPS coating prepared by CU with (a) a 1 μm stack thickness (SS_SPS_DLC1), and (b) a 2 μm stack thickness (SS_SPS_DLC2). Reprinted with permission from (Brown et al., 2020). Copyright © 2020, Elsevier.	50
Figure 18: SEM images of a HVOF-sprayed quasi-crystal coating on aluminum. Reprinted from (Mora et al., 2020) under the Creative Commons license (CC BY 4.0).	51
Figure 19: Different textures on aircraft paint rain erosion substrates with (a) rough, matte PU_TC_NP surface, and (b) shiny, smooth PU_TC_Ref2 surface, however including many bubble defects.....	52
Figure 20: SEM images of polyester fibers before coating, after a single coating process (1-step), and after a double	

coating process (2-step), each shown at two magnifications.....	57
Figure 21: Image of the icing wind tunnel used for this thesis.	63
Figure 22: Total temperature (left) and velocity (right) maps over the cross-section of the test section. Adapted from (Wachsmann, 2019).	64
Figure 23: Limits of Cassie-Baxter wetting state for an impacting droplet on a porous surface.(a) wetting state calculations based on the model of (Deng et al., 2009), highlighting droplet velocity ranges used in the present work. The pore diameter in the x-axis is that of an arbitrary porous or nanostructured surface. (b) Dimensionless droplet impact speed (u/U where u is the observed speed of an impacting droplet and U is the freestream airspeed) observed in the icing wind tunnel on various surfaces, with an overlaid line showing calculated Stokes Number for the range of droplets and speeds observed.	67
Figure 24: Ice adhesion strength measurement setup in the iCORE icing wind tunnel.	69
Figure 25: Diagram of geometric parameters used for calculating interfacial shear stress (a), and the cross-section stress distributions for shear and normal stress in a point-load scenario (b).....	70
Figure 26: Ice accretion procedure temperature and velocity cycle.	72
Figure 27: Typical ice accretions grown in the icing wind tunnel on an aluminum substrate in conditions listed in Table 4, with (a) rime, (b) mixed/rime, (c) mixed/glaze, (d) and glaze ice. Length of the iced	

cantilevers shown is 85 mm, and with an average ice thickness of 4.5 mm.....	74
Figure 28: Illustration of camera synchronization to capture sequential deflection positions during cantilever vibration. Inset figures show the cantilever deflection shape associated with maximum and minimum deflections.	76
Figure 29: Example of the determination of <i>Eice</i> using the intersection of experimental results with parametric FEA. Equations shown are those describing a power-law trendline fitting FEA curves. Experimental data points are shown as constant lines. Encircled regions show where FEA results intersect with experimental results, leading to the determination of an <i>Eice</i> for each experimental data line. The strain/deflection ratio, characteristic of a coated cantilever, is plotted on the y-axis against possible elastic moduli of ice on the x-axis. Here, the modulus determined for 4.5mm-thick ice is 6.4 GPa and that for 7.5mm is 5.6 GPa and 6.6 GPa.	78
Figure 30: Drawing of the NACA0012 support with 180 mm-chord length and labels for positions on the fabrics. LE: leading edge, or stagnation line; S1, S2: suction side; P1, P2: pressure side. Reprinted from (Laroche, Ritzen, et al., 2020) under the Creative Commons License, CC BY 4.0.	79
Figure 31: (a) Pathlines over NACA 0012 iced airfoil sample holder at 0° AoA with an arbitrarily low Reynolds Number, (b) the same with ice formed on the leading edge at 3° AoA showing slightly asymmetric pathlines with small flow separations immediately downstream of the ice, and (c) Ice formation on the fabric mounted on a NACA 0012 airfoil showing	

isolated feathery ice grains near the top side (circled) which become more dense and homogenous approaching the stagnation line. Reprinted from (Laroche, Ritzén, et al., 2020) under the Creative Commons License, CC BY 4.0.81

Figure 32: Working principle of the rain erosion test rig, P-JET, showing a single impacting jet near the substrate while the blocking wheel temporarily prevents oncoming water from getting through until the opening passes in front of the nozzle.82

Figure 33: Example of rain eroded surface with severity conditions by quadrant and by row. Each quadrant contains five repeated impact numbers (columns), one jet adjustment spot below the quadrant, and another one on the top of the quadrant.83

Figure 34: Wetting test following rain erosion on SS_SPS_DLC1, showing water droplets pinned to rain-eroded portions of the surface, and non-eroded portions completed non-wetted.84

Figure 35: Water droplet pinning test on rain-eroded (225 m/s water jet impact speed) textured superhydrophobic surfaces. Rows of spots according to number of water jet impacts between 20 and 6000. No intended variation along columns of spots. Edges of wetted areas appear shiny. Surfaces are grouped by material and type of surface treatment, described in Section 3.1.2. First three rows are laser-structured surfaces on aluminum (AA_), and stainless steel (SS_), with post-treatments after structuring such as plasma-enhanced physical vapour deposition of carbon- and fluorine-containing polymer (_CFx), an electron beam evaporation deposition of metal-oxide termed oblique angle deposition (_OAD), and in some cases,

fluorination (_F) by exposure to 1H,1H,2H,2H-perfluorooctyltriethoxysilane in a vacuum chamber, or spin-coated polydimethylsiloxane (_PDMS). Fourth row consisted of thermal spray coatings by suspension plasma spray (_SPS) or high velocity oxygen fuel. The final row consisted of diamond-like carbon (_DLC) coatings on suspension plasma sprayed titania, polyurethane aircraft paint (PU_), either unmodified (_Ref2), mixed with nanoparticles (_NP), or mixed with nanoparticles then structured by laser (_nsIR). 89

Figure 36: Ice adhesion strength on polyurethane paint formulations for rime and glaze ice. “TC” abbreviates “topcoat,” “ice” abbreviates “icephobic,” “CC” abbreviates “clearcoat,” and “NP” abbreviates “nanoparticles.” 93

Figure 37: Ice adhesion strength on reference surfaces of stainless-steel alloy 304 (SS304 Ref), aluminum alloy 2024 (AA2024 Ref), and grade 5 titanium alloy (Ti6Al4V Ref). 97

Figure 38: Ice adhesion strength of various superhydrophobic surfaces on either titanium alloy (Ti6Al4V), aluminum 2024 alloy (AA2024), or stainless-steel 304 alloy (SS304) substrates. Ice adhesion strength values measured on reference surfaces are indicated by unfilled concentric circles joined by a line to guide the eye. Data under Ti6Al4V and some under AA2024 were extracted from (Vercillo et al., 2019, 2020). 100

Figure 39: Ice adhesion strength for different ice thicknesses and ice types on aluminum. 104

Figure 40: Uncertainty model showing direct or indirect influence of each parameter on interfacial shear stress.....	107
Figure 41: Strain signal measured during ice adhesion strength experiment with mixed/rime ice on AA2024 Rough. Inset shows larger time domain view with the delamination event identified. Data labels are the extracted data. Non-zero baseline due to thermal expansion effects of ice with substrate.....	109
Figure 42: Ice thickness profile of four types of ice grown in the icing wind tunnel. Reported ice thickness for each profile provided in the legend.	112
Figure 43: Young’s Modulus variation with ice thickness for four ice types measured with the vibrating cantilever test setup.	117
Figure 44: Young’s Modulus of ice types averaged over three ice thicknesses.....	118
Figure 45: Ice adhesion strength on AA2024 Ref calculated from strain measurements with a vibrating cantilever using a constant elastic modulus, $E_{ice} = 9$ GPa from literature (light columns), or the measured elastic modulus, E_{ice}^* , different for each type of ice.....	119
Figure 46: Influence of surface roughness on ice adhesion strength for stainless steel 304 alloy and Ti6Al4V. The results of a single group of surfaces was split into two charts where (a) are plotted on average roughness, R_a , and (b) are plotted on average peak-to-trough roughness, R_z . τ symbolizes maximum interfacial shear strength. Dark circles represent stainless steel surfaces, and lighter triangles represent titanium surfaces. Adapted from (Vercillo et al., 2019).	124

- Figure 47: Wetting properties of the superamphiphobic fabric exposed to aerodynamic wear conditions. Pressure side “P2” (hollow square), pressure side “P1” (filled square), stagnation line “LE” (concentric triangles), suction side “S1” (filled circle), suction side “S2” (hollow circle) positions, equilibrium contact angle averaged over all positions (flat bar), and roll-off angle averaged over all positions (cross). (a) After exposure to a warm droplet cloud at speeds from 20 to 120 m/s, for a cumulative duration of 50 min. (b) After exposure to a warm droplet cloud at 90 m/s for up to 50 min. (c) SEM images of polyester fibers on fabrics exposed to 120 m/s (top) and 50 m/s for 3 icing cycles (bottom). (d) After exposure to 3 icing cycles at 50 m/s. Lines are shown as a guide for the eye. Reprinted from (Laroche, Ritzen, et al., 2020) under the Creative Commons License, CC BY 4.0. 129
- Figure 48: Ice adhesion strength on anodized aluminum with silicone nanofilaments, with and without fluorination..... 137
- Figure 49: High magnification SEM image of the SNF-coated aluminum surface before (a) and after (b) 16 cycles of ice adhesion testing. Reprinted from (Laroche et al., 2021) under the Creative Commons License, CC BY 4.0..... 138
- Figure 50: Low magnification SEM mage of the SNF-coated aluminum surface before (a) and after (b) 16 cycles of ice adhesion testing. Reprinted from (Laroche et al., 2021) under the Creative Commons License, CC BY 4.0..... 139
- Figure 51: Ice adhesion strength on titanium as-received (Ti6Al4V Ref), with TiO₂ nanotubes and PFPE (nTiO₂ PFPE), with TiO₂ nanotubes coated with

fluorinated silicone nanofilaments (fSNF), and with TiO₂ nanotubes coated with silicone nanofilaments and infused with 100 cSt silicone oil (LubSNF). 141

Figure 52: Development of ice adhesion strength with ice exposure time (which is a function successive icing cycles) of a lubricant-infused silicone nanofilament network grown on the anodic oxide of a Ti6Al4V. 142

Figure 53: Strain progression during mixed/rime ice accretion on a titanium substrate coated with silicone nanofilaments. Time starts when the icing cloud was introduced into the airflow..... 176

Figure 54: Strain progression during mixed/rime ice accretion on a titanium substrate coated with silicone nanofilaments infused with silicone oil. Time starts when the icing cloud was introduced into the airflow. 177

List of Tables

Table 1: Names and descriptions of standard and reference surfaces tested in ice adhesion.	45
Table 2: Names and descriptions of solid superhydrophobic surfaces tested in rain erosion.....	53
Table 3: Sample names of silicone nanofilament coatings on metallic substrates.	60
Table 4: Icing conditions used in the ice adhesion test.....	73
Table 5: Conditions used for icing wind tunnel durability testing.	80
Table 6: List of properties of polyurethane paint coatings.....	92
Table 7: Roughness and water wetting properties on standard hard surfaces.	95
Table 8: Roughness and water wetting properties of hard textured surfaces tested in the ice adhesion strength rig.....	99
Table 9: Nominal ice thickness grown on each substrate material.	103
Table 10: Data used as input for strain variable in the uncertainty model.....	110
Table 11: Measured values of substrate thickness and length and their standard uncertainty.....	111
Table 12: Standard uncertainties of parameters used for the calculation of interfacial shear stress. Values are determined based on measurements with AA2024 Rough in the mixed/rime condition.	115

Table 13: List of roughness and wetting properties for stainless steel surfaces tested.	122
Table 14: List of roughness and wetting properties for titanium surfaces tested. Data for Ti_LIPSS1, Ti_LIPSS2, Ti_ROUGH1, and Ti_ROUGH2 from(Vercillo et al., 2019).....	123
Table 15: Wettability and roughness characteristics of the SNF surfaces tested for ice adhesion strength. Fluorinated coatings are denoted “fSNF”. ^{a)} Contact angle and roll-off angle was not measurable since droplets were too mobile; ^{b)} Roughness profile is assumed to be the same as T4; ^{c)} Roughness profile is assumed to be the same as A3.....	136

1 Introduction

Humans have an intuitive obsession with natural beauty. In a forest of apparently randomly dispersed trees, a disorganized, chaotic, biological world of shapes, smells, tastes, and textures exists to our unending thirst for exploration. When all life seems to end, in the cold of winter, one may find some glimmering piece of unexplainable self-organization. The shapes of ice crystals in the form of snowflakes have been the object of study for centuries (Kepler, 1611). It is only one of the ways that the normally liquid substance, water, has puzzled humans (Nilsson & Pettersson, 2015; Stone, 2007).

1.1 Dangers of Ice in General

When the surface temperature of the Earth is below 0 °C, unheated water will freeze. Rivers tend not to freeze because the water is constantly being replaced by water from a reservoir at constant temperature (Bohren, 2004), but still-water, such as in ponds, does. Puddles freeze rapidly, and so does precipitation. Freezing lakes can have several advantages resulting from them becoming traversable. Puddles and precipitation that fall to the ground are dangerous because they act as localized low-friction surfaces, which can lead to accidents and consequently, to injury.



Figure 1: Photographs of (a) a frozen lake, (b) a flowing stream of water through a snowy forest, and (c) a sidewalk covered in clear ice.

Precipitation can also freeze on structures. Generally, if ice grows in a high place, there is potential for it to fall and cause injury or damage. This case is of particular concern when the weight of ice exceeds its adhesive strength to a tall building's surface. On power lines, excess weight due to icing can damage support structures, resulting in vast power outages (Dupigny-Giroux, 2000). In extreme cases, ice can weigh down power lines themselves which can also lead to electrical infrastructure failures (J. L. Laforte et al., 1998). On wind turbines, ice reduces their efficiency, which is not immediately dangerous, but can become so when ice is released. Ice blocks that are removed from turbines while they are spinning have both high potential and kinetic energy. They transfer that energy to the ground where they impact, which is uncontrolled, unpredictable, and can lead to loss of life (Parent & Ilinca, 2011). On ships, ice makes surfaces slippery, which can be lethal in some cases. Similarly, on ocean oil rigs, iced surfaces can lead to injury and fatality (Ryerson, 2011).

On aircraft in flight, ice grown on critical surfaces causes loss of lift and impairs manoeuvrability, which can lead to a stall and to a loss of control (Bragg et al., 1986; Cao et al., 2015; Cole & Sand, 1991; Miller & Ribbens, 1999b). In flight, ice can grow due to impacting supercooled droplets, supercooled large droplets, and ice crystals. Ice crystals are not dangerous when they impact cold surfaces if they do not encounter pressure-induced melting, but can melt and refreeze in turbofan engines (Mason et al., 2006). Supercooled droplets and supercooled large droplets freeze and grow into aerodynamically detrimental shapes (Politovich, 1989).

1.1.1 Atmospheric Icing

Once water vapor reaches a certain altitude in the atmosphere the low temperature forces it to condensate. Condensed water which remains suspended in the atmosphere exists in a supercooled state when its temperature is below the heterogeneous solidification temperature of 0 °C (Heinrich et al., 1991b). It is a metastable state, meaning that any disturbance can initiate a phase change into solid ice. The droplet sizes are in the scale of 20 μm , and the temperatures can be as low as -42 °C (homogeneous solidification temperature). When a supercooled droplet is disturbed, the phase change will initiate. Latent heat of fusion is released, bringing the droplet temperature up to 0 °C momentarily.

Suppose an airplane is flying through this cloud of supercooled microdroplets. Most droplets will move to avoid the airplane, following the airstream around it. Many droplets, however, will be struck by the fast-moving aircraft surfaces. These droplets will momentarily increase their temperature to 0°C then quickly drop to the airplane surface temperature (Aliotta et al., 2014; Messinger, 1953; Myers, 2001). The phase change is rapid ($\sim 10^{-2}$ s) and the resulting frozen droplet shape depends mostly on the temperature of the surrounding air, supercooled droplet, and impingement surface

(Yang et al., 2011). The impact frequency, air temperature, impact speed, and droplet size, and droplet cloud liquid water content all influence how compounding droplets freeze over one another. The density, appearance, and shape of ice is dependent on these conditions. At the extremes of the spectrum are rime ice and glaze ice. Rime ice is opaque, porous, and feathery in appearance, and appears at temperatures below -20°C . Glaze ice is clear, dense, wet, and appears at air temperatures between 0°C and -5°C (Makkonen, 2000) (Figure 2). Rime ice appears to be a porous columnar growth where droplets have frozen before completely coalescing. The glaze ice appears more homogenous with a superficial liquid water layer and pockets of internally trapped liquid water.

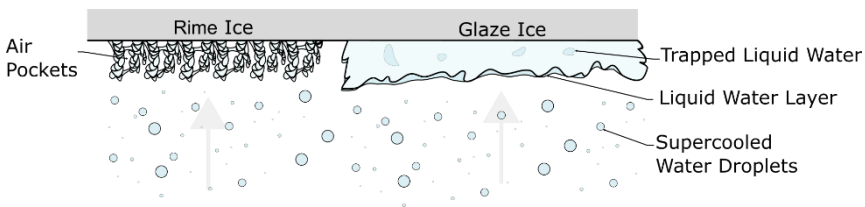


Figure 2: Dry growth of rime ice (left) and wet growth of glaze ice (right). Redrawn from (Makkonen, 2000) and reprinted with permission from (Laroche, Grasso, et al., 2020). Copyright© 2020, John Wiley & Sons.

These different ice types can grow into horned shapes (glaze ice), or bulbous shapes (rime), depending on environmental conditions, including airstream profile, velocity, temperature, and amount of water in the air. Aerodynamic surfaces on which these shapes have grown will suffer from loss or decrease of lift and increase in drag. In the case of critical control surfaces, it can be detrimental to the manoeuvrability of the aircraft and put those on-board at risk. On other surfaces, it can lead to a reduction in aircraft performance and fuel efficiency. The following section discusses several types of components on aircraft and the consequences that icing imposes on their ability to function the way they were designed to do.

1.2 Dangers of Ice Forming on Aircraft

Supercooled microdroplets suspended in a cloud will remain in a liquid state until perturbed. Once disturbed, by say, a solid surface, they will transition to a solid state in a time on the order of 10^{-6} - 10^{-3} s. Ice will grow on the first face to contact the droplets, also termed a leading surface, or leading edge. On an aircraft, surfaces whose normal vector is perpendicular to the direction of flight generally do not accrete much ice in flight. Ice accretes mainly on the surfaces whose normal vector is parallel to the freestream airflow. The angle between a surface normal vector and the freestream air velocity is termed here as the angle of incidence. The aerodynamic profile illustrated in Figure 3 shows an example of a horned ice shape grown on the leading-edge portion. Downstream of the leading-edge portion, there is no ice, since droplets tend to follow aerodynamic pathlines, and not impact those areas. In certain conditions where water is not completely frozen on the leading edge, it can remain on the surface be pushed downstream, forming what is termed “runback” ice.

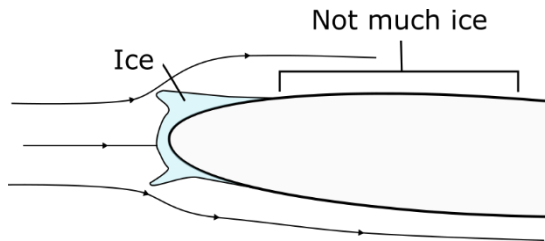


Figure 3: Illustration of a horned ice accretion on an airfoil where there is ice present on low angle of incidence areas and very little or no ice present on high angle of incidence areas.

If formed on the leading edge, ice will change the coefficient of drag due to form drag. It may lead to flow separation over the wing, and hence to a stall. Ice which forms aft of the leading edge, called runback ice, can increase the drag coefficient and therefore increase

the amount of the thrust needed to keep the aircraft aloft. Some aircraft components are at high risk of icing, and of those, some are flight critical. An overview of the icing risk of fixed-wing aircraft components has been presented by (Vukits, 2002). Vukits detailed the threat that ice contamination has on individual component systems, identifying the most critical ones and the most critical types of ice. A brief discussion of some key aircraft components and consequence of their contamination by ice is included here. The discussion includes icing on stabilizers, rotorblades, turbofan engines, external sensors, windshields, and internal fuel lines.

Stabilizers are critical control surfaces of aircraft. Similar to ice on wings, ice on stabilizers can create flow separation. Experiments have shown that ice accretion on vertical and horizontal stabilizers adversely affect the response of control surfaces to pilot input (Miller & Ribbens, 1999a; Ratvasky & Ranaudo, 1993). If the flow over a stabilizer separates, then the stabilizer is no longer able to direct airflow and the pilot may irrecoverably lose control of the aircraft. A similar situation can occur due to icing on some portions of aircraft wings. On rotorcraft, whose control and lift come from rotorblades, ice contamination of those surfaces can quickly make the craft unflyable. Lift and control of an aircraft can sometimes be compensated by adjusting the thrust level and distribution, or rotor torque (in the case of rotorcraft). When icing scenarios are encountered, however, aircraft powerplants are themselves at risk.

Ice forming on the inlet of an engine nacelle affects the flow of air into the engine. The greatest danger is that chunks of ice break off and fly into it. Impact of solid blocks of ice can severely damage a fan or compressor blades. Ice formed on engine fan blades can lead to a stall of the fan, which reduces the airflow to the compressors, and can choke or surge the engine. Fan blades tend to attract ice since sharper radii have higher droplet collection efficiencies, leading to faster ice accretion. In addition to causing costly engine damage, surging or choking the engine results in loss of thrust, loss

of lift, and possibly loss of life. Damage to an engine is usually highly visible to pilots, thanks to various sensors and alarms. Icing of the sensors themselves, however, is usually less perceivable.

Pilots rely heavily on readings from many different sensors on an aircraft to maintain or adjust flight path and level. Sensors mounted to the exterior of the aircraft are naturally exposed to harsh conditions. Those which rely on the flow of air, such as pitot tubes, can report incorrect measurements if covered by ice. For example, on a flight from Rio de Janeiro to Paris, one or more of the Pitot tubes of the aircraft was covered in ice and reported incorrect underspeed (Bureau d'Enquêtes et d'Analyses, 2012). Pitot tubes are redundant sensors, meaning many of them are expected to report the same information. The confusion between the different sensor readings on this flight eventually led to an impact of the aircraft with the ocean, and loss of all lives on board. Pilots tend to rely primarily on plain visibility for navigation. Avionics displays and sensors are there to assist in systematic navigation and in case of poor visibility. If sensors malfunction, then visibility is the only option available, meaning that in icing conditions, a clear windshield is a safety asset.

For obvious reasons, ice forming on windshields obstructs a pilot's view of the aircraft surroundings. Although fixed-wing aircraft can be flown on instruments alone, visibility of the horizon is crucial for landing an aircraft, navigating complex mountain terrain, or flying a low-altitude aircraft such as a helicopter. There is therefore little tolerance for ice or frost buildup on the windshield of an aircraft. Visibility is needed for flying intuitively. Pilots visually see where they need to direct the aircraft, and then command the aircraft to follow that trajectory. When the aircraft does not respond to those commands as expected, it can be an extremely puzzling and dangerous situation. Such a scenario can occur due to ice forming internally within an aircraft.

1.3 Ice Protection Systems used on Aircraft

Icing in aerospace is a popular topic of discussion because, even though events are infrequent compared to the number of successful flights (Cole & Sand, 1991; Isaac et al., 2001; Jones et al., 2008), it has the highest potential for fatalities as compared to ice on roads, power lines, or wind turbines. Aerospace is a risk-averse industry, and the level of risk tolerance decreases with increasing on-board population. That statement can be translated to: larger aircraft are guarded more rigorously against icing than smaller aircraft. The main reason that protection system type varies with aircraft size is the available power. Small aircraft have small engines (also termed power plants), making energy-intensive solutions impractical. For this reason, small aircraft are not allowed to fly in certain icing conditions. Active ice protection systems exist in case of light icing conditions and when severe icing conditions are unintentionally encountered (FAA, 2009). Below is a concise description of the general types of active ice protection systems: thermal, mechanical, and chemical.

Thermal ice protection systems are the most popular because they are robust. If a surface is heated to a high enough temperature, water cannot freeze on it. If the surface was first unheated and ice has accreted, heating the interface will weaken the bond and aerodynamic drag forces will remove the ice. A surface may be heated using electrothermal heating elements, or by convection with a warm gas or fluid (Heinrich et al., 1991a). The former is useful for heating small components such as sensors, and the latter for larger surface areas. Large aircraft equipped with turbofan engines (all commercial airliners that carry more than 100 passengers), use engine bleed air for convective heating of large surface areas. Turbofan engines have two general sections: a cold section including the fan and compressors, and a hot section, which is everything downstream of the combustion chamber. The air in the compressor section, although termed cold, can reach rather elevated

temperatures. This warm, pressurized air is ideal for warming surfaces, but its extraction from the engine comes at a high fuel-efficiency penalty.

Low energy-consumption active ice protection systems for small aircraft include mechanical and chemical ones. A traditional mechanical system, often used as the baseline to compare new systems to, is the de-icing boot (Goraj, 2004) – an elastomeric membrane that inflates with air on command. The method requires that ice be first accumulated such that the strain produced at the interface results in sufficient stress to break ice apart. Once broken, and the bond face weakened, aerodynamic drag force removes the ice. This method is strictly a reactive countermeasure by design since it cannot prevent ice from forming. In some cases, ice remnants can remain stuck to the membrane (Figure 4), which can simultaneously disturb aerodynamic flow and act as anchoring points for further ice accretion (Transportation Safety Board of Canada, 2014).



Figure 4: Rime ice left-over on a wing leading edge after de-icing boot (black component) activation. Picture reproduced from (Transportation Safety Board of Canada, 2014)¹.

¹ Original image available at:

A chemical system involves the secretion of a substance, normally in liquid form, from a surface (Goraj, 2004). The substance, when mixed with ice lowers the freezing temperature, thereby creating a layer of liquid water. Once the interface with ice has been weakened, aerodynamic drag removes the ice. This method can be a preventative as well as reactive countermeasure depending on when the substance is secreted.

The most effective ice protection solution discussed thus far is the thermal method. It is also the most energy-intensive system. Mechanical and chemical methods were an answer to the question of how to incorporate a practical low-energy consumption system. As a trade-off, they suffer from less-than-perfect reliability. In the next section, novel techniques for reducing the energy consumption of thermal systems and improving the effectiveness of mechanical systems are presented.

1.3.1 Ways to Improve Ice Protection System Efficiency & Efficacy

Ice protection systems that are in-service have advanced since their first iterations (Goraj, 2004; Greenly, 1963), with small increments in efficiency by improved design. Systems that use different fundamental principles of ice removal or prevention, which would dramatically reduce energy consumption, have been until now only experimental. Many have arrived at the demonstrator stage but have not been implemented into standard production.

Active systems based on vibration or microwave (Feher & Thumm, 2006) have shown promise at small scale, but they come with

peripheral complications. Concerns have been shown for the reliability of vibration systems, since experiments have shown that they do not completely shed ice after each actuation (Pommier-Budinger et al., 2018; Rouset et al., 2016). Radiation methods often require heavy, bulky, sensitive, and/or costly equipment which makes them unattractive to aircraft manufacturers (Feher & Thumm, 2006; Goraj, 2004). Since incremental iterations of in-service ice protection systems seem to have had some success in industry, the most realistic solutions become those that are based on tried-and-true systems with some variation.

A surface to which ice does not stick would solve many of the problems faced by conventional ice protection systems without requiring re-engineering of the entire system. On vibration-based systems, it would reduce the amount of deformation needed to remove ice, thereby reducing the energy consumption at the same time as increasing the probability of fully cleaning the surface from ice. On thermal systems, the icephobic surface would help to reduce the energy needed to remove ice or to keep the surface ice free, by reducing the interfacial contact area. Such hybrid systems have also been proposed as a method to provide robust but efficient ice protection (Morita et al., 2020; T. Strobl et al., 2015). The functioning principles of surfaces that can improve active ice protection methods are discussed below.

1.4 Challenges of Implementing Functional Surfaces for Ice Protection in Aerospace

Passive ice protection systems are those that prevent ice from causing the failure of a structure, device, or surface without the introduction of energy. That categorization has different meanings depending on the application. The definition of an icephobic surface as means for

passive ice protection has been debated, but certain common requirements arise:

- Low adhesion to ice (Brassard et al., 2019),
- Prevents or slows the formation of ice (Tourkine et al., 2009),
- Assists an otherwise active system in reducing the energy required to prevent or remove ice (Antonini et al., 2011).

The proposal of icephobic surfaces as an ice protection system was an answer to the applications where active systems are difficult to implement. It has been a serious goal of the aerospace community since the 1970's (Leary, 2002; NASA, 1978; Peterson & Dadone, 1980). Early works found that certain materials such as polymers will release ice with much less force than other materials such as aluminum (Makkonen, 2000). Later on, it was found that Teflon® surfaces show low ice adhesion to ice grown from sessile water (Landy & Freiburger, 1967), but not to ice grown from impacting supercooled water droplets (Stallabrass & Price, 1963).

Since then, there have been numerous efforts to create special surface topologies and chemistries to address the three points listed above (Boinovich et al., 2014; Huang et al., 2019; S. A. A. Kulinich & Farzaneh, 2009). Despite these efforts, the aerospace industry has been slow to adopt the use of any functional surfaces to improve their ice protection system efficiency (Huang et al., 2019). Close collaborations between the aerospace industry and research institutes show promising advances that could lead to such implementation. Recently, following the biological studies of hydrophobic plants such as the lotus leaf, surface microstructures have become the focus. (Milles et al., 2021; Vercillo et al., 2020) have determined optimal laser structure patterns on aircraft alloys that tend to reduce the adhesion strength of ice, and to reduce the energy demand from an electrothermal de-icing and anti-icing system. The surfaces they produced were reportedly durable in icing

conditions, but exterior aircraft surfaces are typically exposed to a broad variety of conditions that may deteriorate such surfaces.

Surfaces are the protective skin through which any mechanical component interacts with its exterior environment. Aircraft are exposed to high temperatures, low temperatures, UV-radiation, corrosive fluids, corrosive humid/salty environments, and impact to rain droplets or sand particles at high speed (Huang et al., 2019). Their exterior surfaces are therefore engineered to resist deterioration under regular exposure to such harsh environments. Accelerated aging tests are commonly used that are representative of the type of conditions an aircraft will encounter during normal usage. Some of the environments, such as those related to temperature cycling, or extended high/low temperature exposure tend not to degrade most coatings. The more aggressive environments include corrosive atmosphere, corrosive fluid, solid particle erosion, and rain erosion. The more common an environment occurs naturally, the more important it is for the surface to endure – generally, rain. Let us now examine the state of the art of existing aircraft surfaces and novel icephobic surfaces.

2 State of the Art

When it comes to icephobic surfaces, the basic physical principles have only recently been identified. An impractical number of allegedly icephobic surfaces have been introduced to the ice adhesion community, with nearly 550 publications on the topic since 2010 (Zhuo et al., 2021). A practical approach to evaluating these coatings is to first come up with auxiliary criteria. In aerospace, those criteria are mainly durability. To contextualize these requirements, an introduction to some of the most common surfaces currently in-service on aircraft is given. Then, the principles behind the different icephobic technologies are described. Finally, methods for assessing the ice-repellency of novel surfaces are presented.

2.1 Surfaces commonly used on Aircraft

The design of aircraft has always been a balance (read battle) between structural integrity and aerodynamic efficiency. Proponents of structural integrity tend towards preferring heavier, more reliable designs. Those who focus on aerodynamic efficiency opt for weight reduction wherever possible. The skin of an airplane fuselage is a good example of this compromise. The lightest materials that could be used as an aircraft skin and still produce lift are textiles. These have been used historically on early airplanes (FAA, 2012), and are still used today for hobby or extremely lightweight planes (Maule Aerospace Technology Inc., 2016). The strongest and most reliable material that can be used would be some form of steel. The compromise that has been reached, at least for large commercial aircraft, is the use of thin (on the order of a few millimeters) aluminum panels. This material is not as stiff as steel, and not as lightweight as textiles, but it is strong enough to allow for cabin pressurization and it has one third the density of steel. These are the most obvious design factors used for the selection of materials on

aircraft. The skin was chosen here as an example because it involves an additional critical design criterion, which is the ability to resist damage from corrosive and erosive environments.

As was mentioned in the previous section, ice accretion can be dangerous on aircraft for mostly aerodynamic reasons. However, the likelihood of encountering icing conditions is heavily outweighed by the likelihood of encountering other adverse conditions like rain, for example. Rain can also affect aerodynamics and it has a strong erosive tendency on surfaces (Fyall, 1966). A small amount of erosion on thick metal panels will on its own not usually cause catastrophic failure of a component. It will, however, promote the onset of corrosion, which can lead to catastrophic failure. Corrosion can be summarized as the oxidation of a metal surface and is associated with its deterioration. Metal oxides are more brittle than metals, meaning they are easier to fracture. The protection of aircraft metals from corrosion is therefore of primary importance. That is the reason for the selection of specific metal alloys for the aircraft skin and many exterior components.

A large portion of aircraft skin is made from aluminium 2024 alloy. Its main alloying element is copper, and it is well-known for its corrosion resistance when a thick oxide layer is present. When one sees an aircraft flying, one typically does not see exposed metal. Rather, airplanes have an appealing painted finish which serves a greater purpose than just airline identity. Airplane paint coatings have been in development since the early 1950's. Through trial and error, they have reached a point of robust balance between corrosion protection, erosion resistance, UV-resistance, cleanability, aesthetics, and repeatability, among other factors.

The leading edges of aircraft components are often subjected to the most abuse. Like birds' flying-V patterns, where the leading bird is the first to disturb the airflow, and it must be the strongest. Often (on many components) leading edges are reinforced by erosion

shields. Erosion shields are sometimes hard metal alloys, or metal alloys that have been hardened by anodic oxidation. One example is the use of titanium on the leading edge of fan blades on some turbofan engines. Specifically, grade 5 titanium alloy, or Ti6Al4V is one of the most commonly used on aircraft.

Lastly of interest in the context of this thesis, stainless steel alloys are used in specific places on aircraft despite their relatively high density. Stainless steel does not have a fatigue limit, unlike aluminium, and it does not need a coating for corrosion resistance. These qualities make it ideal for load-critical external components such as landing gears.

2.2 Strategies for Making Icephobic Surfaces

The ideal icephobic surface is one on which ice can never form. Through repelling of water, or impeding heat transfer, some surfaces can be engineered to resist the formation of ice, but not indefinitely – meaning they can only delay the onset of ice nucleation, but not prevent it. A more realistic solution is to create a surface that can easily release ice. One can take advantage of the brittleness of ice by designing a rather deformable surface. High deformability of an interface tends to increase stress concentrations, leading to facilitated interfacial fracture. If the surface is so deformable that it is no longer considered a solid (i.e. a liquid), then ice may never technically be adhered to it. Or at least, the adhesion strength would be limited to the adhesion or cohesion of the liquid surface. Below, each of these strategies is described in more detail, following the order of surface rigidity.

2.2.1 Structured Solid Surfaces (Superhydrophobic Surfaces)

“If a surface could repel water, then it could also repel ice.” This hypothesis has been tested by several researchers over the years

(Jung et al., 2011; Meuler, Smith, et al., 2010). It turns out that the key to ice-repellent surfaces is more complex than simply repelling water droplets (S. A. Kulinich et al., 2011; Nosonovsky & Hejazi, 2012). Nevertheless, accompanied by an active ice protection, such as a heater, a water-repellent surface can decrease the heating power needed to repel droplets, and therefore improve its efficiency (Antonini et al., 2011). To elaborate on these ideas, the working principles of wetting will first be introduced with a focus on the interaction between water and a solid surface.

The interface between a liquid and a solid surface surrounded by a gas is characterized by the angle between the edge of the liquid and the surface, known as the contact angle. Young's equation describes the thermodynamic equilibrium condition of a liquid on a surface surrounded by a gas or vapour phase. In his essay, (Young, 1805), Young described two conditions: fully wetted, or partially wetted. The partially wetted case (Figure 5) is that where a droplet exists as opposed to a uniform liquid film (fully wetted case). The arrows in Figure 5 indicate tension vectors where γ_w is that between the liquid and the vapour, γ_s between the solid and vapour, and $\gamma_{w,s}$ between the liquid and the solid. Thermodynamic equilibrium is achieved when:

$$\gamma_s = \gamma_{w,s} + \gamma_w \cos \theta \quad (1)$$

The angle, θ , here is the equilibrium contact angle, so named because it describes the state of thermodynamic equilibrium. This angle lies between the advancing and receding contact angles of the droplet on a surface. The advancing contact angle is observed when the three-phase contact line moves onto a previously dry portion of solid surface. The receding angle is observed when the three-phase contact line moves away from dry solid surface.

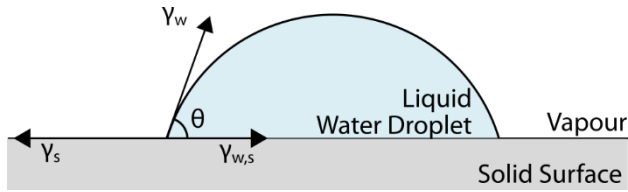


Figure 5: Water drop on a solid surface and definition of the contact angle. Redrawn from (Zisman, 1964). Reprinted with permission from (Laroche, Grasso, et al., 2020). Copyright© 2020, John Wiley & Sons.

The above equation, Young’s Equation (Young, 1805), is described for an ideal solid surface with theoretically no roughness. Real surfaces, however, always have some finite roughness. The state of wetting termed the Wenzel state is given by a droplet in contact with a surface having some roughness, and is illustrated in Figure 6a. The increased contact area between the droplet and the surface was considered through a parameter, r , which is the ratio between actual contact area to idealized contact area (Wenzel, 1936).

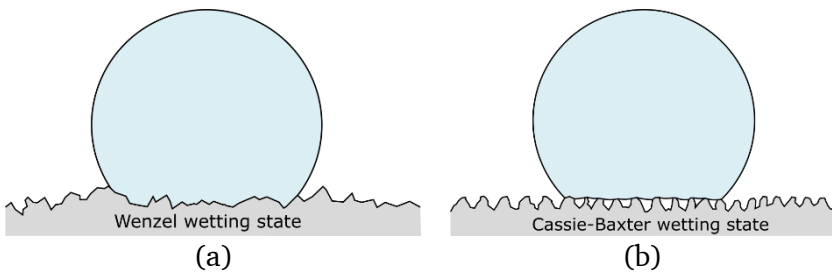


Figure 6: Wetting models on rough surfaces. (a) Wenzel model showing a droplet in contact with a complete surface profile, and (b) the Cassie-Baxter wetting model showing a droplet supported by asperities in the surface profile.

When the roughness features are large enough and spaced closely enough together, surface tension effects can result in air gaps between asperities and below a liquid droplet. This state is termed the Cassie-Baxter state after their work describing the phenomenon on textiles (Cassie & Baxter, 1944). The Cassie-Baxter wetting state,

illustrated in Figure 6b, is highly sought-after for applications related to non-wetting. A Cassie-Baxter state leads to surfaces qualified as superhydrophobic. Due to the reduced contact area between a liquid droplet and a solid surface, the droplet becomes easier to remove from the surface than in the Wenzel state. Depending on, among other factors, how a droplet was deposited, the Cassie-Baxter state can transition to a Wenzel state (Koishi et al., 2009; Patankar, 2004). If that happens, then the adhesion of the droplet to the surface becomes much higher than on a non-textured surface.

Some threshold values have been proposed in an attempt to objectify the label of superhydrophobic (Antonini et al., 2011): an equilibrium contact angle in excess of 150° , and difference between advancing and receding angle less than 10° . The values are disputed because they are somewhat arbitrary, but the general idea is that the contact angle is rather high, and the tilt angle low (Marmur, 2004). The tilt angle, roll-off angle, or sliding angle are all terms to describe the angle relative to the gravitational vector at which a droplet will begin to move on a surface.

Based on the well-documented and mostly agreed-upon physics of micro-structured superhydrophobic surfaces, the surface engineering community sought to fabricate them using scalable methods relevant for engineering applications. Laser patterning was one of the favoured methods. Micropillars produced by laser on metals were not as tailored as those produced lithography on other substrates, but they effectively produced water-repellent and ice-repellent surfaces (Vercillo et al., 2019). Laser patterning was favourable because of its versatility in terms of substrate material, its reproducibility, since the process was computer-controlled, and the wide range of patterns that could be achieved. Its primary drawback was the processing time. It could take several minutes to engrave a certain surface pattern into a square millimeter of surface. For enhanced scalability, surfaces created by thermal spray have also been explored to a large extent (Donadei et al., 2020; Koivuluoto et

al., 2020; Mora et al., 2020; Sharifi et al., 2019). Metal-oxide or ceramic coatings with certain surface structures were obtained by tuning spray parameters. The advantage of this method is that it is fast, uniform, and produces a hard coating with high adhesion to the substrate material. The wide variety of thermal spray techniques also opened the possibility for some temperature-sensitive materials to be coated.

Not all microstructured superhydrophobic surfaces proved to be icephobic. It was suggested that when microdroplets impact, they were able to spread around microscopic asperities, creating anchoring points and increasing ice adhesion strength. Focused studies on the topic of structured surfaces for aircraft ice protection concluded that nanostructures in combinations with microstructures provided the ideal icephobic surface (Vercillo et al., 2020). The capillary pressure needed to penetrate nanoscale structures is much higher than microscale structures. On their own, nanostructures are capable of keeping impacting droplets in the Cassie-Baxter wetting state. However, their small size makes them more susceptible to mechanical damage. Nano-scale structures can be protected by micro-scale structures, producing a durable surface that can repel high-speed impacting microscopic water droplets. Advanced laser-patterning techniques, and advanced thermal spray techniques such as suspension plasma spray (SPS) are both capable of producing hierarchical structures.

In summary, hard surfaces superhydrophobic surfaces in certain forms have been shown to reduce adhesion to ice. Micro-scale surface features may create anchoring points for ice formed by impacting supercooled water droplets, thereby increasing ice adhesion strength. Nano-scale topology superposed over microscopic features can prevent droplets from entering a Wenzel state on impact, and can therefore enhance ice-release properties. Microscopic features can serve as mechanical protection of the nano-

scale features from abrasion, but if they are somehow damaged by scratching, then pinning sites will form, to which ice and water will remain adhered.

2.2.2 Compliant Surfaces

Another approach to minimizing the adhesion strength of ice to a surface is to increase the deformability of the surface rather than reducing the contact area. Elastomeric surfaces are usually flat and are not necessarily superhydrophobic. Mechanical interlocking at the interface is altogether avoided. The stiffness of elastomers is at least one order of magnitude lower than conventional metals and metal oxides. Their stiffness can be modified by plasticizing them to make them softer or by increasing the cross-link density between molecules to make them more rigid. Softer elastomers tend to deform locally when in contact with water droplets (Pericet-Cámara et al., 2008). The effective roll-off angle of droplets tends to increase with increasing stiffness (Extrand & Kumagai, 1996), but is nevertheless much higher than on superhydrophobic surfaces; around 20° on dry elastomers compared to $<10^\circ$ on superhydrophobic surfaces.

Where liquid droplets tend to stick more strongly, solid ice is apparently more easily removed. The work of (Golovin & Tuteja, 2017) shows a consistent decreasing trend in ice adhesion strength with increasing plasticization of elastomeric coatings. Ice is not a tough material, meaning that it fractures at relatively low strain, and has difficulty conforming to a deformed surface. This surface engineering solution is scalable, conceptually simple, and rather inexpensive (Golovin et al., 2019). Soft surfaces are inherently damage intolerant. They are highly susceptible to abrasion and erosion, and are easily peeled off of a substrate. If surface defects can be refilled with the soft polymer, then they become more damage-tolerant (Golovin et al., 2017).

When structured, compliant surfaces can exhibit a similar Cassie-Baxter wetting state as structured solid surfaces. An example of one such surface is the silicone nanofilament coating (Zimmermann, Rabe, et al., 2008). Coatings composed of silicone nanofilaments (SNF) have shown superhydrophobicity (Zimmermann, Artus, et al., 2008), and durable superamphiphobicity (Geyer et al., 2020). They are chemically inert so they do not decompose in harsh chemical environments, nor do they degrade from exposure to UV (Zimmermann, Reifler, et al., 2007). Conceptually, they show higher toughness (can be deformed more before breaking) than hard nanostructures due to their flexibility. However, on flat glass plates, low mechanical stability of SNF coatings has been reported (Zimmermann, Reifler, et al., 2008). Enhanced durability has been achieved using fabric substrates instead of flat glass (Zhang et al., 2014). Fibers and weaves provide a microstructure to the SNF which protects the sides not facing the shear stress from abrasion, conserving superamphiphobicity. The sponginess of fabrics effectively reduces contact pressure with SNF, reducing the likelihood of them being abraded.

The durability of superamphiphobic fabrics has been evaluated by prolonged chemical exposure, and by exposure to an urban external environment on the outside of a car. The car was driven at speeds up to 120 km/h (33 m/s) and traveled a distance of more than 5,000 km. The most severely damaged fabric suffered a water roll-off-angle increase of 20° (from 5° to 25°) and hexadecane roll-off-angle increase of 40° (from 10° to 50°). Despite its degraded performance, SNF remained attached to the polyester fibers after the 257 days of exposure (Geyer et al., 2020).

If a mechanically degraded compliant surface could repair itself passively, it would then be more robust. Mechanical degradation commonly takes the form of partially removed material. Self-repair, in this case, would constitute refilling the missing portion of

material. This mechanism has been answered by un-crosslinked polymers, which behave more as a viscous liquid than as a solid and are discussed further below.

2.2.3 Lubricant Infused Surfaces

A superhydrophobic surface relies on hydrophobic surface chemistry and surface asperities to support a droplet. If a droplet is in a Cassie-Baxter wetting state, air pockets exist between asperities. With a reduced solid-liquid contact area (replaced with liquid-air contact), the mobility of the droplet is enhanced. The problem with this scenario is that the air pockets can be notoriously unstable. When the air pocket fails, the liquid-solid contact area of the droplet is increased as compared to a complete flat surface and is known as a Wenzel state. If the air pockets were more stable, it would make the superhydrophobic surface more robust. One way to increase the stability is to decrease the mobility of a gas, or in the case of a fluid, increase the viscosity. That is, if the air were replaced with a fluid or lubricant, then the droplet is less likely to fill the space between asperities. That is the concept of a lubricant-infused surface.

A lubricant-infused surface can exist in three different states: underfilled, perfectly filled, and overfilled. These states are illustrated in Figure 7. For simplicity, let us focus the discussion on the perfectly filled case. Here, lubricant fills gaps between surface asperities and covers the asperities themselves with a thin film. On these surfaces, the adhesion strength of ice is theoretically lowest. Ice can still grow on oil films but will shear off with a force which depends on the viscosity of the oil. Typically, gravity is a sufficient force. The lubricant tends to create a film over everything it comes in contact with, including liquid droplets. If damage occurs on the micro- or nano-structure of the surface in which the lubricant is infused, the lubricant would soon replenish that area, making it uniform with the un-damaged surface.

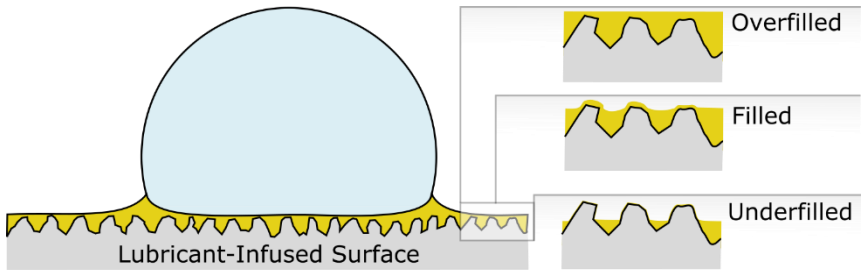


Figure 7: Schematic example of a water droplet on a lubricant-infused textured surface, showing three possible lubrication states: overfilled, filled, or underfilled.

There is therefore a competition between surfaces in contact with a lubricant. A lubricant or oil will be attracted to any surface it comes in contact with (liquid or solid). This statement means that when a dry surface comes into contact with a lubricant-infused surface, some of the lubricant will infuse into the dry surface, partially draining the initially lubricated one. For example, when ice grows on a lubricant-infused surface, some of the lubricant will be drawn into the ice, and will thereafter be removed with the ice (Hauer et al., 2021).

Niemelä-Anttonen et al. tested lubricant infused porous polymers in an icing wind tunnel at 25 m/s (Niemelä-Anttonen et al., 2018). They concluded that ice adhesion strength to these surfaces was low, but degraded after ice removal. It should be noted that they keep their iced samples for over 16 hours before ice shedding. This long-term ice contact permits enhanced drainage of oil from the porous polymers. In another instance, (Yeong et al., 2018) presented a lubricant infused porous elastomer, they termed Self-Lubricating Icephobic Coating (SLIC). They put SLIC surfaces on a rotor at 1000 rpm and exposed them to supercooled droplets at 10 m/s airspeed (total airspeed ~ 37 m/s). Later, (Tetteh & Loth, 2020) tested SLIC using a different device, but still in an airflow of 40 m/s and at -21°C .

It showed little-to-no degradation in low ice adhesion strength for 5 icing/de-icing cycles.

Alternatively, it has been shown that nanoporous surfaces will tend to retain lubricant oil in the presence of frost and ice (Wong et al., 2020). The reason being capillary forces in the nanopores are stronger than those in ice, meaning some lubricant is also retained. A SNF porous network, for example, could exhibit such lubricant retention. The discussion until now has been focused on types of surfaces that can reduce the energy necessary to remove ice from a surface. The way ice is formed and removed can influence that metric. The following section discusses the techniques for discriminating whether a surface is icephobic or not.

2.3 Qualification of Icephobic Surfaces²

The prevention of ice nucleation has only been shown in controlled laboratory conditions, where the time for a sessile water droplet to freeze was measurably extended with respect to a reference surface. In tests closer to practical icing, such as in an icing wind tunnel, some surfaces have shown a lower mass accretion of ice than a reference surface. That is an indication of delayed ice nucleation, however, ice still accreted on that surface. For in-flight icing conditions, which are broad and unpredictable, freezing-delay surfaces are not yet reliable enough to show clear advantages. More attention is therefore placed

² The basis for the contents of this section has been published in a book chapter (Laroche, Grasso, et al., 2020, DOI: 10.1002/9781119640523.ch9)

on lowering ice adhesion strength, which has practical benefits for the improved efficacy of an ice protection system.

Techniques for measuring icephobicity range from abstract to real, and from simple to complex. The general theme is that the simpler the technique, the less reliable, which holds true for the inference method. The discussion then continues in order of modes of loading. Mode I loading is perpendicular to the ice/substrate interface, and mode II loading is parallel to the interface. The focus then falls on mixed mode (combination of mode I and mode II) loading since it is the loading mode used in the rest of this thesis. Within each loading mode section, at least two techniques are described, beginning with a simple low-cost method, followed by one performed in an icing wind tunnel.

The spectrum of ice adhesion test methods covers, on one end, the evaluation of fundamental behaviour of a surface, to the evaluation of the gross behaviour of the surface when placed in near-real conditions. Two main features influence where a test method lies on the spectrum: the ice formation procedure, and the ice removal procedure.

Ice, the solid phase of water, begins to form when its temperature drops below the melting point of water. The most basic ice adhesion test relies on this principle to generate a bond between ice and a surface. Usually, a pool of water is contained by an open cuvette placed on a substrate surface. The cuvette, water, and substrate are all placed in cold air (below the melting point of water), or the substrate is cooled by an electrical surface cooler (Peltier cooler). After the water freezes, the cuvette is removed, and the measurement of ice removal force can take place. Depending on the purity of water, ice produced by this method is optically transparent.

Water can still exist in the liquid phase despite it being at a temperature lower than its melting point. This metastable state

occurs when the water has a high-purity and is undisturbed (not shaken). The reason is that a threshold energy needs to be overcome before the first nucleus of ice can form. Once ice begins to nucleate, the phase transition propagates through the rest of the body of water. The formation history of ice influences its mechanical, optical, and adhesion properties when attached to a surface.

Understandably, special equipment is needed to reproducibly create ice from a metastable, supercooled state. The most commonly used method is to generate a spray of high-purity water droplets within a cold environment. The droplets can become supercooled without freezing while they are suspended in the air. They begin to transition to solid phase after making contact with a substrate surface. At low speeds, this type of ice formation resembles that of freezing rain or freezing fog. At high droplet impact speeds, it resembles icing encountered during flight, also termed in-flight icing.

Depending on the temperature, impact speed, and concentration of droplets in the air, the resulting ice formation can be described along a continuum terminated by rime and glaze ice. Rime ice is opaque, feathery and columnar while glaze ice is optically transparent and dense. Everything in-between is termed mixed ice, where additional qualifiers such as mixed-rime or mixed-glaze help to discriminate further.

Ice delamination is an interfacial fracture problem. The sought-after results of ice delamination tests can be maximum interfacial stress before debonding, average interfacial stress before debonding, and the ratio between damaged interface (adhesion fracture) or internally damaged ice (cohesive fracture). Depending on the anticipated mode of fracture, either the interfacial normal stress, the interfacial shear stress, or both are of interest. The fracture energy has also been reported but is less common.

Every loading case uses either mode I, mode II or mixed mode loading to generate interfacial stresses. Mode III loading is rarely used. The ratio between mode I and mode II loading can be characterized by the phase angle of loading. An angle of 0° means a pure mode I loading, and 90° , a pure shear or mode II loading. The situation is complicated by the difference in modulus between the ice and substrate. In this case, the phase angle no longer directly describes the balance between mode I and mode II, but rather that between the real and imaginary components of the complex stress intensity factor. The translation between complex stress intensity factor and the mode I/mode II ratio is non-trivial, and a universal model does not exist for that relation (Rice, 1988). For simplicity of analysis, many researchers perform adhesion tests in an attempt to create pure loading, be it either mode I or mode II.

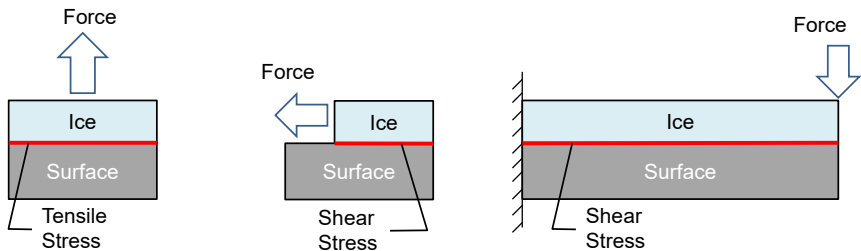


Figure 8: General loading conditions used to measure interfacial bond strength between ice and a substrate. Direction of applied load shown by arrow, and interface shown by a red line. Reprinted with permission from (Laroche, Grasso, et al., 2020). Copyright© 2020, John Wiley & Sons.

2.3.1 Mode I Tests

Loading in the direction normal to an interface creates what can be visualized as a body separation stress. For an ideally perfect contact between the two bodies, this separation stress relates to the tensile strength of the chemical bonds between atoms of the two substances. Considering real surfaces which have some roughness, and imperfect

interfacial bonding, the measurement of mode I adhesion strength reveals the tensile strength of the imperfect interface.

One of the early mode I tests published, depicted in Figure 9, involves an embedded force transmission rod. While still liquid, a high-tensile strength rod is dipped into the water pool. When the water freezes, it clamps onto the rod over a greater area than with the substrate surface. The rod is then pulled until ice separates from the substrate surface. The pulling force divided by the ice-substrate interface area reveals the interfacial normal stress.

A point to be considered in this test is the shear stress between the rod and the ice. Configured slightly differently, this test can be used to obtain the interfacial shear strength between the rod surface and the ice.

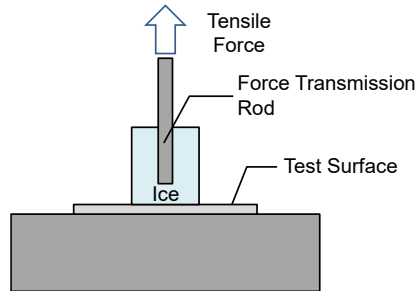


Figure 9: Tensile ice adhesion test method using an embedded pull-rod. Reprinted with permission from (Laroche, Grasso, et al., 2020). Copyright© 2020, John Wiley & Sons.

A mode I test designed for studying the adhesion of in-flight or atmospheric icing involves the use of air pressure to push an ice formation away from an interface (Figure 10). A polytetrafluoroethylene (PTFE) disk at the interface acts as a controlled initial crack size. In principle, the test method works well to determine the adhesion strength of ice to a surface, however, the ice often breaks cohesively rather than at the interface. Since the

load is concentrated near the center for the cylinder, the stress flows through the ice in such a way that it can fail cohesively in shear (M. Pervier, 2012).

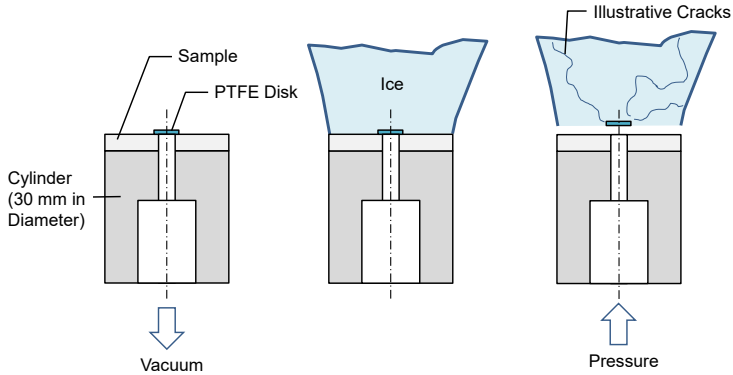


Figure 10: Mode I ice adhesion test for the measurement of adhesion of impact ice in-situ. (M. Pervier, 2012). Reprinted with permission from (Laroche, Grasso, et al., 2020). Copyright© 2020, John Wiley & Sons.

2.3.2 Mode II Tests

The rudimentary pusher test method (Figure 11), has been presented as a purely mode II test. Although it is a mixed-mode test, the analysis is simplified by assuming that shear is the principal failure mechanism. It has been used recently to propose the idea of a critical bond length, where adhesion strength transitions from being cohesive shear strength-dominated, to interfacial toughness-dominated (Golovin et al., 2019).

Keeping a constant ice height and width, the length of the ice block was varied as the force required to remove the ice was measured. The authors found that the force required to remove the ice off some surfaces plateaued after a certain length. They argued that the critical bond length on these surfaces was shorter than those of the

surfaces that did not exhibit such behaviour. The authors claim that surfaces with a short critical ice adhesion length will have a lower adhesion to ice on large length scales than surfaces with a long critical length (Golovin, 2017).

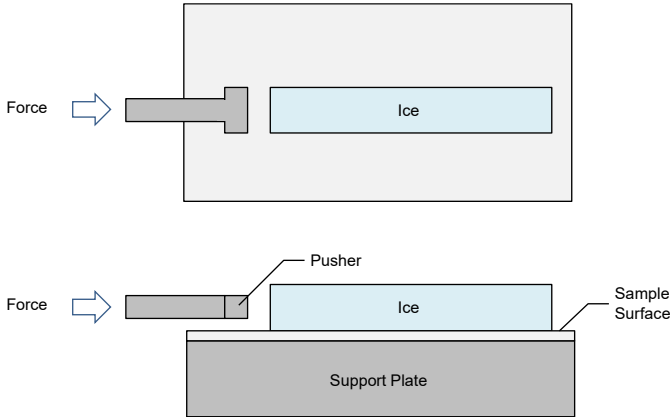


Figure 11: Rudimentary pusher test for Mode II ice adhesion tests. Adapted from (Golovin, 2017). Reprinted with permission from (Laroche, Grasso, et al., 2020). Copyright© 2020, John Wiley & Sons.

The rudimentary pusher test is instrumental for the development of icephobic coatings. The bond between water and surface prior to freezing is homogenous and the method is low-cost such that coating developers can perform the test as a generic method with results that are clear and easy to interpret. Its simplicity and controllability, however, distance it from real-life icing scenarios for which the surfaces being studied are designed.

The pusher test has been adapted for conditions resembling those of atmospheric icing, where ice accretes due to impacting supercooled water droplets (M. L. A. Pervier et al., 2019). The general difference at the ice-substrate interface is the higher proportion of porosities,

and imperfections in the impacting supercooled droplet case. The setup shown in Figure 12 includes floating shields designed to control the shape of ice accretion. Conceptually, the bond length is limited only by the available geometry of the setup. Like most impact ice adhesion test setups, the bond length is kept constant. An inflatable membrane constrained behind a pusher is how load is applied to the ice. The air pressure within the membrane is increased until the force applied to the pusher is sufficient to remove ice from the substrate. The single degree of freedom of the system forces interfacial failure, and discourages cohesive failure within the ice.

The stress state of the ice has been modeled by finite element analysis. The analysis allowed the authors to determine a critical stress concentration factor from experimental data, being the critical inflation pressure. Thus, the interfacial toughness can be calculated directly from the measurable critical inflation pressure. The initial crack size was assumed to be the ice grain size at the interface. Ice grain sizes for different ice types were measured through separate calibration experiments using an innovative technique (M. A. Pervier et al., 2017).

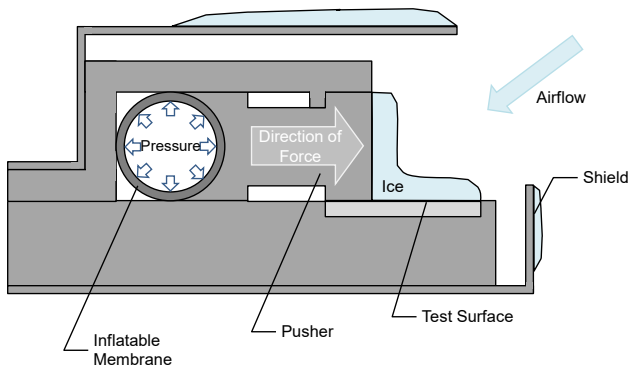


Figure 12: Pusher test designed for testing the adhesion of impact ice to a surface in-situ. Adapted from (M. Pervier, 2012). Reprinted with permission from (Laroche, Grasso, et al., 2020). Copyright© 2020, John Wiley & Sons.

2.3.3 Mixed-Mode Flexure Tests

The cantilever beam test method was first reported for ice adhesion strength measurement by (Blackburn et al., 2000). A detailed description of the test method and its usage was included in (C. Laforte, 2001, 2002). It is depicted in Figure 13a according to the latter description. Ice was accreted on long slender beams in a cold chamber. They would then be placed vertically with the bottom end fixed. The top free end would be pushed by a motor-actuated screw that would apply a controlled, steady force. A load sensor at the free-end and two linear variable differential transformer (LVDT) sensors near the base would provide the data needed to determine the point force that would cause failure of the ice-substrate interface. A sudden drop in the force measured by the load cell indicated the moment of delamination of the ice and translated to the ice adhesion strength. Since the free-end load was known and controlled, equations were derived to compute the strain release rate and interfacial toughness.

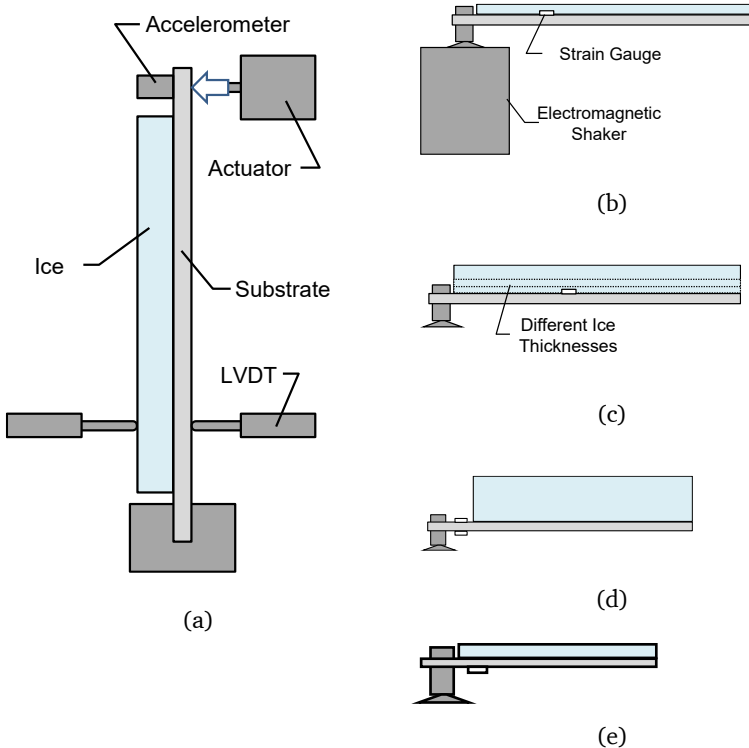


Figure 13: Configurations of the bending test for measuring ice adhesion strength, (a) controlled applied force (C. Laforte, 2001), (b) vibrating beam with strain sensor at interface (Javan-Mashmool et al., 2006a), (c) vibrating beam with strain sensor at interface (Akitegetse et al., 2008), (d) vibrating beam with two strain gauges on substrate near interface (Hassan et al., 2010), and (e) vibrating beam with single strain gauge on substrate behind interface (Tobias Strobl et al., 2013).

The theoretical framework for a variation of the system developed by Blackburn et al. using forced cantilever vibration was laid out in (Javan-Mashmool et al., 2005). The vibrating beam test method, Figure 13(b), was first reported for ice adhesion strength measurement by (Javan-Mashmool et al., 2006b). Using a piezoelectric polyvinylidene fluoride (PVDF) sensor placed at the ice-

substrate interface, they directly measured the interfacial stress during dynamic bending of the cantilever. They identified the instant of delamination from the sensor signal and deemed that value the ice adhesion strength.

In the same group, (Akitegetse et al., 2008) delved deeper into the test method with finite element simulations validated by experiments. They placed the sensor further from the fixed end of the cantilever and did ten repetitions of three different ice thicknesses (Figure 13(c)). The apparent ice adhesion strength decreased with increasing ice thickness, amounting to near-zero at a thickness of 13 mm. Among the conclusions of his work were that the rate of amplitude increase during the first phase of vibration did not influence the measured ice adhesion strength, and that the sensor measured only bending stress, and not interfacial shear stress as initially presumed.

Across the globe, (Hassan et al., 2010) used a similar method with some modifications. Namely, they replaced the PVDF sensor with commercial strain gauges, and placed them outside the ice/substrate interface (Figure 13(d)). Doing so eliminated the risk of the sensor influencing the adhesion strength because the sensor did not interact with the ice at all. They also performed a finite element analysis, showing the distribution of stress along the interface and noting that the range was within that reported in literature by different sources.

To their credit, Hassan et al.'s method included a half-bridge strain gauge configuration, which is more reliable than a quarter bridge. The disadvantage of that is in order to avoid interacting with ice, the strain gauges were placed outside the iced area. It is unclear how they could calculate ice adhesion strength using strain readings outside the vicinity of the iced area. The strain in the ice-free portion of the beam can only reveal the normal stress within the substrate itself. This stress does not represent the normal stress nor the shear stress at the interface of the iced portion. Additionally, any increase

in strain reading brought upon by delamination of the ice could not be detected by the strain readings alone. Lastly, their calculation of ice thickness was motivated by wanting to place the neutral axis of the iced beam at the interface, but they mis-used the equation and grossly over-estimated the ice thickness needed. Based on the calculation they published, it is clear that a misinterpretation of the eccentricity equation was to blame. Specifically, their calculation holds true for the case that it yielded an absolute distance with respect to the base of the system, rather than a relative distance from the interface of the two materials, which it actually was.

(Tobias Strobl et al., 2013) built a system close to that of Hassan et al. They used only one strain gauge instead of two, and placed it on the back-side of the substrate, beneath the ice formation. This placement, illustrated in Figure 13(e), allowed them to directly measure the extension of the iced section of the substrate during vibration. Their stress model was similar for calculating the ice adhesion strength.

2.4 Outline of the Thesis

Section 4.1, 4.2, and 4.3 are a summary of durability and ice adhesion tests performed on a relatively large number of superhydrophobic surfaces. They were mostly qualitative tests which gave direction to the more in-depth studies of later sections. Rain erosion tests are summarized and analyzed in section 4.1. The results of that chapter have been concisely mentioned in several publications focusing on specific surface fabrication techniques. Here, the collected results are presented and discussed in more detail. In chapter 4.2, the focus is on paint coating systems and their promise as ice-release coatings. Their ice adhesion strength properties have been determined and compared to in-service paint systems. The ice adhesion strength of hard textured coatings and flat reference surfaces is discussed at length in Chapter 4.3.

To determine the cause of the wide span of results shown in Chapter 4.3, the aim of Chapter 4.4 is to begin to narrow down method-related results. One of the biggest differences between successful and unsuccessful surface technologies was the substrate material. Therefore, this chapter is dedicated to identifying the role of the different test conditions on these different substrates.

With one parameter understood, Chapter 4.5 expands the idea of method-dependent results by analyzing the overall uncertainty of the ice adhesion strength model. Here, each measurand from the model is discussed and its criticality is calculated.

The Young's modulus of ice was the most influential parameter found using the uncertainty model. In Chapter 4.6, a method for measuring the Young's modulus of ice using the ice adhesion test setup is described, thereby reducing the overall model uncertainty.

The test method-related influences on the test have been understood so our focus in Chapter 4.7 moves to the most apparent surface influence on ice adhesion strength, roughness.

Having confirmed the importance of a mix of nano- and micro-scale roughness, surface energy, and local flexibility, silicone nanofilament coatings are selected as the ideal candidate coating for further study. Intuitively, nano-size filaments are fragile, so their durability is first experimented on in the icing wind tunnel. In Chapter 4.8, silicone nanofilaments are grown on textile substrates and placed on the leading edge of an airfoil. Their measured durability indicated that they were capable of withstanding high aerodynamic shear conditions and icing conditions.

In Chapter 4.9, the silicone nanofilament coatings are matured further. Here, they were grown on metallic substrates, specifically, aerospace grade metals. In the icing wind tunnel, they proved to withstand the abuse of 16 icing/de-icing cycles, and their ice

adhesion strength was the lowest measured using this test method. Particularly, fluorinated or lubricant-infused silicone nanofilament coatings were the best-performing.

3 Materials and Methods

The main theme of this thesis is the determination of a suitable surface for the reduction of ice adhesion strength in aerospace applications. A description of the surfaces tested is therefore given at the beginning. The majority of the surfaces were fabricated by partner institutions. To categorize the surfaces, their water contact angle and surface roughness were measured. In cases of nanostructured surfaces, scanning electron microscopy images were also recorded. Next, the surfaces were subjected to testing in the icing wind tunnel. The test of greatest importance for this thesis was the ice adhesion test. The test rig was also used for measuring the elastic modulus of ice grown in the icing wind tunnel. Tests for mechanical durability were also performed. The less aggressive one was exposure to water droplet clouds at high airspeed in the icing wind tunnel, and the second, more aggressive, accelerated rain erosion test, described in the end of this chapter.

3.1 Surfaces & Substrates

This section begins with a description of the substrate materials used. The untreated surfaces of these substrates are considered standard surfaces to which candidate icephobic coatings are compared. Included in the standard surfaces is the conventional aircraft paint system, aluminum 2024 alloy, titanium grade 5 alloy, and stainless steel 304 alloy. Following that is a description of the methods used to fabricate superhydrophobic surfaces on these substrates. Then the growth of silicone nanofilaments is specifically addressed, and the section ends with the method used for filling silicone nanofilament surfaces with silicone oil.

3.1.1 Substrate Materials and Reference Surfaces

Metal alloys in ambient environment have a thin (a few nanometers thick) oxide layer on their surface. This oxide layer is termed the “native” oxide layer. It is produced by the reaction of the metal atoms with oxygen in the air. On stainless steel alloys, this oxide layer (specifically chromium oxide) is what gives it its mirror-like appearance and what makes it “stainless”. Metal-oxides are electrochemically passive and tend to protect the bulk alloy from electrochemical corrosion. In the case of aluminum 2024 alloy, the native oxide layer is very thin and can be easily ruptured. A thicker oxide layer may be grown using a wet electrochemical process known as anodization. In this process, the native oxide layer is chemically etched, and a new one is grown with a controlled thickness and general structure (amorphous pores, columnar pores, or dense). The resulting, relatively thick, anodic oxide increases the hardness of the substrate surface. Immediately drying an anodized substrate, the surface is highly attractive to organic contaminants in the air. The reason is that free hydroxy groups are present on the oxide surface that want to bond with any carbon-based molecules in proximity. This attraction produces a time-dependent wettability behavior. Immediately after anodization, the contact angle of water with the surface may be 10° - 15° . Some hours after that, if the substrate is left in open atmosphere, the contact angle may stabilize at $\sim 60^{\circ}$.

The central reference surface to which all other surfaces are compared in this work is a polished, anodized aluminum 2024 alloy. The substrate is first mirror-polished to eliminate roughness effects to facilitate the study of material properties on ice adhesion behaviour. Substrates were cut to size, $1.6 \times 13 \times 125 \text{ mm}^3$, from a large sheet measuring $1.6 \times 2000 \times 5000 \text{ mm}^3$ (AMAG rolling GmbH, Austria) using a hydraulic guillotine. The aluminum substrates were then polished using a manual polishing device (Struers LaboSystem, Struers GmbH, Germany) with progressively finer silicon carbide

paper with abrasive particle suspension: 6 μm , 3 μm , 1 μm , then 0.25 μm (Struers GmbH, Germany). This process removed the clad layer, replacing it with a native aluminum oxide layer.

The substrates were then cleaned and etched in alkaline baths at elevated temperature, which was followed by an acidic pickling step to remove the oxide layer. They were then placed in an electrolyte bath with tartaric acid and sulfuric acid. They were anodized for 20 minutes, then dried in an air dryer. The substrate named AA2024 Ref was left to rest in atmosphere. The rest of the substrates were dipped in a commercial two-part perfluoropolyether (PFPE) solution (Episurf, Surfactis, France) for 5 minutes. Upon being retracted from that solution, the surfaces became hydrophobic (see Table 7 in Section 4.3).

Grade V titanium alloy sheets (VSMPO, Verkhnyaya Salda, Russia), also referred to as Ti-6Al-4V, with 1 mm thickness were cut to size (125 mm x 13 mm) using a hydraulic guillotine. The edges were deburred, and substrates were cleaned by scrubbing with acetone followed by propan-2-ol. The preparation of the Ti6Al4V Ref substrate was complete at this point. A superhydrophobic titanium surface was prepared by the following steps.

Substrates were suspended on a titanium rack and anodized in an aqueous solution containing 130 g/L ammonium sulphate and 5 g/L ammonium fluoride, as described in the literature (Mertens et al., 2015; Wermuth et al., 2015) to grow a layer of organized TiO_2 nanotubes on the surface. Freshly anodized titanium substrates were dipped in a two-part perfluoropolyether solution, as described for aluminum substrates, for 5 minutes. Upon retraction of the titanium substrates from the solution, they were superhydrophobic (see Table

7 in Section 4.3). The average pore diameter of the nanotubes imaged in Figure 14 was $32 \text{ nm} \pm 10 \text{ nm}^3$.

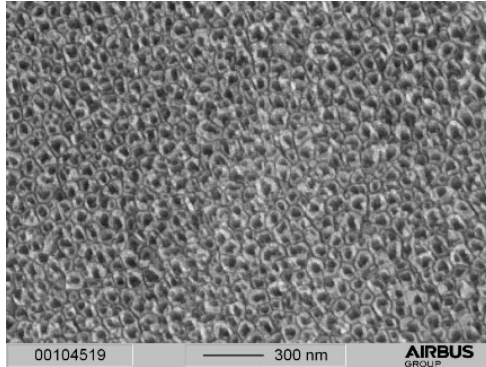


Figure 14: SEM image of self-organized TiO₂ nanotubes on a Ti6Al4V substrate.

Stainless steel alloy 304 substrates, measuring $1.5 \times 13 \times 126 \text{ mm}^3$, were obtained from a partner research institute (CSIC, Spain). Prior to testing they were degreased by scrubbing with acetone, followed by propan-2-ol, as was done on titanium substrates.

Polyurethane aircraft paint systems were applied on aluminum 2024 alloy substrates. The substrates were first anodized as described above, then sent by post to two coating providers. The first, PU TC Ref1, was applied by a commercial coating supplier (Alexit, Mankiewicz, Germany). It consisted of a primer layer, and a topcoat

³ Measured by manually fitting an ellipse to each pore using an open-source software, ImageJ (National Institute of Health, USA). The population of ellipses was 216.

layer. In this coating system, the topcoat provides both a white pigment, and a shiny, durable overcoat.

The seven reference surfaces described above are listed in Table 1. The ice adhesion strength on these reference surfaces served as a baseline to compare novel surfaces. Most of them are similar to the surfaces seen in-service on aircraft. The exceptions are AA2024 PFPE, and Ti6Al4V nTiO₂ + PFPE, which served as reference hydrophobic and superhydrophobic coatings respectively. Their surface roughness and contact angles are listed Table 7 of Section 4.3.

Table 1: Names and descriptions of standard and reference surfaces tested in ice adhesion.

Name	Substrate	Description
AA2024 Ref	AA2024	Polished and anodized.
AA2024 PFPE	AA2024	Polished and anodized, then dip coated in PFPE.
AA2024 Rough	AA2024	Roughened using 120-grit sandpaper.
Ti6Al4V Ref	Ti6Al4V	As-received.
Ti6Al4V nTiO ₂ + PFPE	Ti6Al4V	Anodized to grow TiO ₂ nanotubes, then dip coated in PFPE.
SS304 Ref	SS304	As-received.
PU TC Ref1	AA2024	Polyurethane aircraft paint system consisting of a primer and topcoat applied by a commercial supplier.

3.1.2 Hard Textured and Modified Polyurethane Surfaces

The preparation of superhydrophobic coatings by thermal spray, physical vapour deposition, or laser patterning was performed by the following institutes:

- Concordia University in Montreal, Canada (CU)
- Polytechnic University in Montreal, Canada (PM)
- Spanish National Research Council in Seville and Zaragoza, Spain (CSIC)
- National Institute of Aerospace Technology in Madrid, Spain (INTA)
- Technology Partners in Warsaw, Poland (TP)

Laser-treated stainless steel and aluminum substrates were prepared on coupons measuring 2 x 80 x 150 mm. A laser was passed over a single face of the substrate. Aluminum plates were treated with a 20W nanosecond infrared unpolarised Nd-YAG laser (Powerline E, Rofin-Baasel Inc.) with a 100 ns pulsewidth and a 20 kHz repetition rate at CSIC in Seville, Spain. The scanning parameters used included 16 W of power, 20 kHz repetition rate, 100 mm/s scanning speed, and 20 μm between scanning lines without overlap between passes. The resulting surface had an amorphous microroughness depicted in Figure 15. The average surface roughness and contact angle values for these surfaces are listed in Table 8.

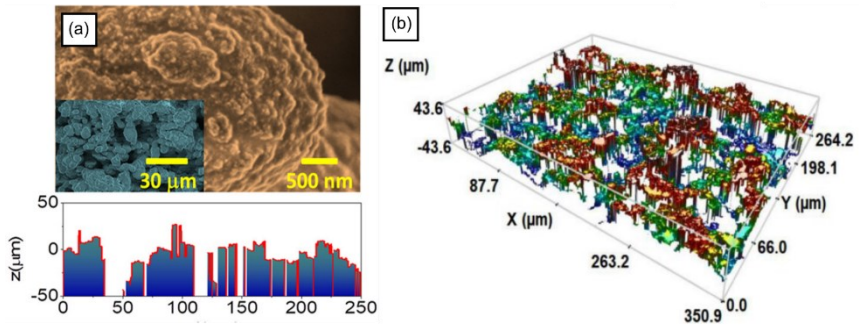


Figure 15: Laser pattern produced by a nanosecond infrared laser on an aluminum substrate with (a) an SEM image above a surface roughness profile, and (b) the areal surface roughness profile taken by confocal microscope. Reprinted with permission from (V. J. Rico et al., 2019). Copyright © 2019, American Chemical Society.

At CSIC in Zaragoza, Spain, a picosecond UV-wavelength laser was used. Here, two passes were used to produce a pillar pattern. The surfaces labelled as SS_psUVs were made using 8 Amperes laser power setting, 400 kHz repetition rate, 100 mm/s scan speed, 15 μm between scan lines with 25% overlap, and a superimposed pass with 8 A laser power setting, 400 kHz repetition rate, 20 mm/s scan speed, and 150 μm between scan lines without overlap. Those surfaces with the SS_psUVf label were made using 7 A laser power setting, 300 kHz repetition rate, 750 mm/s scan speed, 15 μm between scan lines without overlap, and an superimposed pass with 8 A laser power setting, 400 kHz repetition rate, 20 mm/s scan speed, and 150 μm between scan lines without overlap.

The Cfx treatment, performed at CSIC, given to respective laser treated surfaces consisted of a plasma-enhanced physical vapour deposition (PECVD) of a carbon- and fluorine-containing polymer with nanometric to sub-micron thickness. According to the method description in (V. J. Rico et al., 2019), a parallel-plate reactor was used with 50% C_4F_8 and 50% Ar at 0.15 mbar. A voltage was applied

to the top plate at 13.56 MHz such that a negative self-bias voltage of 100V would be created in the bottom plate, which also acted as the sample holder.

Oblique angle deposition (OAD) was another kind of post-treatment used by CSIC for coating laser-treated samples. With this technique, porous films of alumina (on aluminum substrates) or stainless steel (on stainless steel substrates) were deposited by electron beam evaporation with the substrate at an angle of 85° (V. Rico et al., 2020).

The final post-treatment techniques used by CSIC on this family of substrates were fluorination (_F) and polydimethylsiloxane (_PDMS) coatings. For fluorination, samples were first exposed to a low intensity plasma for 10 minutes in an oxygenated chamber, then they were exposed to 1H,1H,2H,2H-perfluorooctyltriethoxysilane vapor in a vacuum reaction chamber for 3 hours (V. Rico et al., 2020). The reaction chamber was placed in a thermal bath at 80°C. PDMS coating was performed by spin-coating.

Thermal spray surfaces prepared by CU were done using suspension plasma spray (SPS) (Sharifi et al., 2016, 2019). Substrates were prepared for coating by abrasive roughening via grit blasting using 80-grit Al₂O₃. They were then cleaned in acetone in an ultrasonic bath. A suspension solution of 10 wt% TiO₂ sub-micron particles (TKB Trading, Canada) in ethanol was prepared using polyvinylpyrrolidone (PVP360, Sigma-Aldrich, Canada) as a dispersing agent. The suspension was fed at a rate of 55 g/min. into a radial injection plasma torch (3 MB, Oerlikon Metco, Switzerland). Ar and H₂ were used as the plasma gas at a combined flow rate of 60L/min. The power of the plasma torch was 36 kW (600 A, 60 V), the stand-off distance to the substrate was 5 cm, the speed that the torch passed over the substrate laterally was 1 m/s, and the overlap between passes was 3 mm. Once the samples cooled to room temperature, they were removed from the SPS booth, and cleaned

by compressed dry air. They were then placed in boiling water for 10 min. and rinsed with isopropyl alcohol. The final treatment was a dip coating in 0.5% solution of stearic acid (Fisher Scientific, Canada) in 1-propanol (Fisher Scientific, Canada). The resulting coating and its cauliflower-like appearance is shown by SEM images in Figure 16.

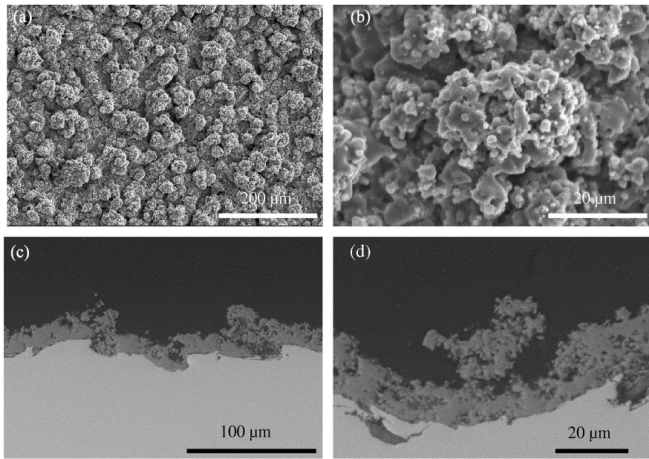


Figure 16: SEM images of SS_SPS_SA prepared by CU, where (a) and (b) are top views, and (c) and (d) are view of the cross-section. Reprinted with permission from (Sharifi et al., 2016). Copyright© 2016, Elsevier.

Diamond-like carbon (DLC) coatings were grown at PM as post-treatment to some of the SPS-coated samples produced by CU (without the stearic acid treatment) (Brown et al., 2020). The DLC coatings were grown by PECVD in a stainless steel chamber evacuated to 10^{-6} Torr prior to deposition. The SPS-coated substrates were first plasma cleaned in an Argon environment for 10 min. Then, with the substrates in the PECVD reaction chamber, gas mixtures of varying respective compositions of Ar, SiH₄, N₂, and C₂H₂ were introduced to grow a layer of SiN_x (150 nm), DLC (750 nm or 1750 nm), and plasma-polymerized hexamethyldisiloxane (PP-HMDSO,

100 nm), in that order. The resulting coating thickness above the SPS was 1 μm or 2 μm , denoted by `_DLC1` and `_DLC2` respectively. The coating stack is shown by SEM image in Figure 17. The DLC coating covered the nano-scale features of the SPS coating. The effect was more prominent in the 2 μm stack thickness than the 1 μm stack thickness.

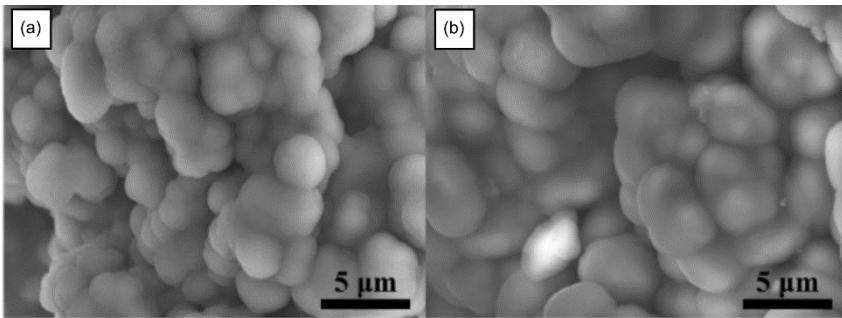


Figure 17: PECVD coating stack produced by PM over the SPS coating prepared by CU with (a) a 1 μm stack thickness (`SS_SPS_DLC1`), and (b) a 2 μm stack thickness (`SS_SPS_DLC2`). Reprinted with permission from (Brown et al., 2020). Copyright © 2020, Elsevier.

High velocity oxygen fuel (HVOF) is a thermal spray technique that was used by INTA to coat stainless steel substrates. Three types of coatings were created using this technique, `SS_QCrystal`, `SS_WCCo`, and `SS_HHS`. The first was a quasi-crystal coating. Quasi-crystals are a metallic material with properties approaching those of ceramics, such as low thermal and electrical conductivity, and high hardness. The procedure used was as described in (Mora et al., 2020), but stainless steel substrates were used here instead of aluminum. Substrates were first grit-blasted to increase roughness, then cleaned with acetone in an ultrasonic bath. Non-stick quasi-crystal powder with particle sizes ranging from 20-75 μm (Cristome A1/S, Saint-Gobain, France) were composed of Al (54%), Cu (18%), Fe (14%), and Cr (14%). The powder was dried by heating and mixing at 80°C for 2 hours using a Glass-Col stirrer (098ARD9924, Terre Haute,

USA). They were then fed through a twin rotation powder feeder to an HVOF spray gun (Diamond Jet Hybrid HVOF unit A-3120, Sulzer Metco, Switzerland) mounted to a six-axis robot (ABB, Switzerland). The spray parameters included a gas flow rate of 180 L/min. O₂, 344 L/min. H₂, 635 L/min. N₂. The powder feed rate was 25 g/min., the stand-off distance to the substrate was 360 mm, and the spray gun traverse speed was 1691 mm/s. The microstructure of the quasi-crystal coating on stainless steel, SS_Qcrystal, was similar to that shown in Figure 18 on aluminum. The HHS and WCCo coatings were applied in a similar fashion. Both high-hardness steel and WCCo were used because of their high hardness and abrasion-resistant properties. An electroless nickel-polytetrafluoroethylene coating (SS_Ni-PTFE) was also produced by INTA.

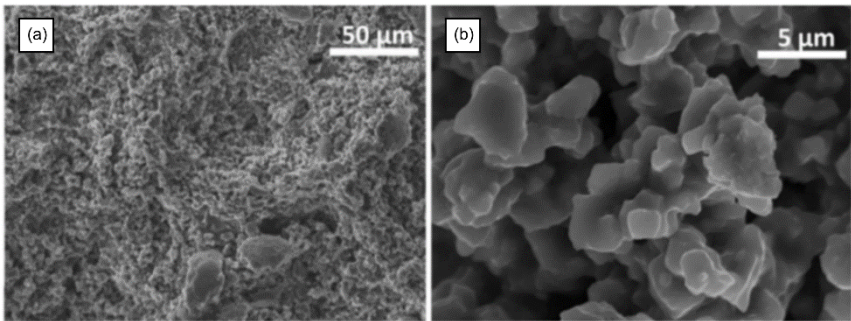


Figure 18: SEM images of a HVOF-sprayed quasi-crystal coating on aluminum. Reprinted from (Mora et al., 2020) under the Creative Commons license (CC BY 4.0).

Polyurethane (PU) paint coatings here were applied by TP with the procedure described in (Przybyszewski et al., 2019). The PU_TC_Ref2 paint was a 3-component topcoat (Aviox® finish 77702, Akzo Nobel, Netherlands) on an amine epoxy primer (Aerodur® HS370922, Akzo Nobel, Netherlands). Substrates were cleaned for 15 min. by acetone in an ultrasonic bath. The primer components were mixed then sprayed on using a spray gun (Pilot

XIII, Walther-Pilot, Germany) and dried for 3 hours. The polyurethane topcoat was prepared, sprayed over the primer using the same gun, then dried for 24 hours. The PU_TC_NP was applied in the same manner, and the topcoat was mixed with silane/siloxane blend and silica nanoparticles. Hydrophobic nano-silica particles (16 nm nominal size, Aerosil® R8200, Evonik, Germany) were mixed with the silane/siloxane blend (DC88, Dow Corning, USA) into the topcoat with 5 wt% each, and using a magnetic stirrer. The modified topcoat suspension was further mixed using an ultrasonic processor (VCX 750, Sonics and Materials Inc., USA) for 30 min. The resulting coatings (Figure 19) included bubble defects (shown by small lumps in Figure 19b). The addition of a chemical modifier and nanoparticles to the topcoat formulation also resulted in a less glossy appearance (PU_TC_NP, Figure 19a).

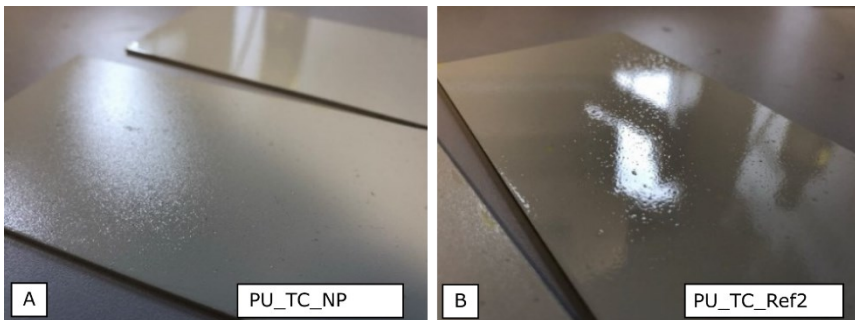


Figure 19: Different textures on aircraft paint rain erosion substrates with (a) rough, matte PU_TC_NP surface, and (b) shiny, smooth PU_TC_Ref2 surface, however including many bubble defects.

The coatings described above are listed in Table 2 with their respective name used in this thesis, substrate material, a brief description and the supplier. These surfaces were all tested in the rain erosion apparatus (described in Section 3.4.2, results in Section 4.1), with the exception of SS_HHS, due to logistical constraints. The wetting and roughness properties of the coatings among these,

tested in the ice adhesion test rig (described in Section 3.3.2, results in Section 4.3) are listed in Table 8 of Section 4.3.

Table 2: Names and descriptions of solid superhydrophobic surfaces tested in rain erosion.

Sample Name	Substrate	Description	Supplier
AA_nsIR	AA2024	Nanosecond infrared laser treatment	CSIC
AA_nsIR_CFx	AA2024	Nanosecond infrared laser treatment followed by a PECVD deposition of a C ₄ F ₈ polymer	CSIC
AA_nsIR_OAD_F	AA2024	Nanosecond infrared laser treatment followed electron beam oblique angle deposition of Al ₂ O ₃ , and finished by vapour-phase fluorination	CSIC
AA_nsIR_OAD_PDMS	AA2024	Nanosecond infrared laser treatment followed electron beam oblique angle deposition of Al ₂ O ₃ , and spin-coated PDMS	CSIC
SS_nsIR	SS304	Nanosecond infrared laser treatment	CSIC
SS_nsIR_CFx	SS304	Nanosecond infrared laser treatment followed by a PECVD deposition of a C ₄ F ₈ polymer	CSIC
SS_nsIR_OAD_PDMS	SS304	Nanosecond infrared laser treatment followed electron beam oblique angle deposition of Al ₂ O ₃ , and spin-coated PDMS	CSIC
SS_psUVs	SS304	Picosecond ultraviolet laser treatment (slow pass)	CSIC
SS_psUVs_CFx	SS304	Picosecond ultraviolet laser treatment (slow pass) followed by a PECVD deposition of a C ₄ F ₈ polymer	CSIC
SS_psUVf	SS304	Picosecond ultraviolet laser treatment (fast pass)	CSIC
SS_psUVf_CFx	SS304	Picosecond ultraviolet laser treatment (fast pass) followed	CSIC

SS_SPS_SA	SS316	by a PECVD deposition of a C ₄ F ₈ polymer Suspension plasma sprayed coating of TiO ₂ on SS304 + stearic acid coating	CU	
SS_QCrystal	SS304	A hard, non-stick quasi-crystalline coating deposited by HVOF and composed of Al Cu and Fe.	INTA	
SS_WCCo	SS304	WCCo coating deposited by HVOF	INTA	
SS_HHS	SS304	High-hardness steel coating deposited by HVOF	INTA	
SS_Ni-PTFE	SS304	Electroless Ni-PTFE coating	INTA	
SS_SPS_DLC1	SS316	Suspension plasma sprayed coating of TiO ₂ + Diamond-like coating grown by physical vapour deposition (2 μm)	CU + PM	
SS_SPS_DLC2	SS316	Suspension plasma sprayed coating of TiO ₂ + Diamond-like coating grown by physical vapour deposition (4 μm)	CU + PM	
PU_TC_NP	AA2024	Polyurethane basecoat with nanoparticles applied on AA2024	TP	
PU_TC_NP_nsIR	AA2024	Polyurethane basecoat with nanoparticles applied on AA2024 +laser patterning of the coating	TP + CSIC	
PU_TC_Ref2	AA2024	Polyurethane basecoat applied by research lab onto AA2024	TP	

3.1.3 Silicone Nanofilament Coatings

The durability of hard textured coatings was tested by exposure to high-speed water jets to simulate rain erosion. It was expected that this test would be too aggressive for silicone nanofilaments coatings, so their durability was tested by exposure to high-speed airflow and cloud droplet conditions only. Dedicated durability tested were carried out on polyester textile substrates (100 mm x 150 mm) and

ice adhesion tests on metallic substrates (1.6 x 13 x 125 mm³ AA2024, and 1.0 x 13 x 125 mm³ Ti6Al4V).

Silicone nanofilaments can be grown on surfaces by a hydrolysis reaction. The reaction can take place in vapour phase, or in solution. Here, the in-solution method was used to grow SNF on polyester textile sheets. The vapour-phase method was for metallic substrates. The fabrication of SNF coatings and their post-treatment took place at:

- Max Planck Institute for Polymer Research in Mainz, Germany for coatings on textiles, and
- University of Zurich in Zurich, Switzerland for coatings on metal substrates.

3.1.3.1 Fabrication of Superamphiphobic Fabrics⁴

Plain weave polyester fabrics (poly(ethylene terephthalate) or PET), purchased from Karstadt, Germany, were immersed in a solution of trichloromethylsilane (Sigma-Aldrich, 0.4% vol.) in toluene (Fisher Chemical) containing water at 150 ppm, for 3 hours (1-step). To increase the thickness of the coating, the solution was exchanged and replaced by a fresh solution (2-step). In the following they are referred to as a 1-step and 2-step procedure. Upon removal from the solution, they were rinsed with n-hexane (Fisher Chemical) and dried with nitrogen. This process was used to grow a SNF network on the fabrics, making them superhydrophobic.

⁴ The following methods description was reprinted from (Laroche, Ritzen, et al., 2020) under the Creative Commons license CC BY 4.0.

Superamphiphobicity was achieved by binding fluorine groups to the surface of the SNF. Coated fabrics were activated in an oxygen plasma chamber (Diener Electronic Femto, 120 W) for 2 minutes. They were then immersed in a solution of 1H,1H,2H,2H-perfluorodecyltrichlorosilane (PFDTs, 0.05% vol.) in n-hexane for 20 minutes. Upon removal, they were rinsed in n-hexane and dried with nitrogen gas. The procedure has been detailed in (Geyer et al., 2017, 2020).

The fabrics were imaged before and after coating by scanning electron microscopy (SEM), Figure 20. SEM images were taken with a Zeiss LEO 1530 Gemini SEM at gun voltages of 3 kV using the in-lens detector. To avoid charging, samples were sputtered with Pt before measurement using a BalTec MED 020 modular high vacuum coating system (with an argon pressure of $2 \cdot 10^{-5}$ bar and a current of 30 mA, 7 nm Pt). The bare fibers in the fabric were smooth with frequent but random minor defects. The fabrics that were coated once (1-step) show a slightly more uniform coverage of SNF on the fibers than those coated twice. The average thickness of the coating increases from approximately $1.5 \mu\text{m}$ after the first step to approximately $2.5 \mu\text{m}$ after the second step. The thickness of the nanofilaments varied between 50 and 100 nm and the spacing between filaments ranged from 100 nm to $2 \mu\text{m}$ (2 step).

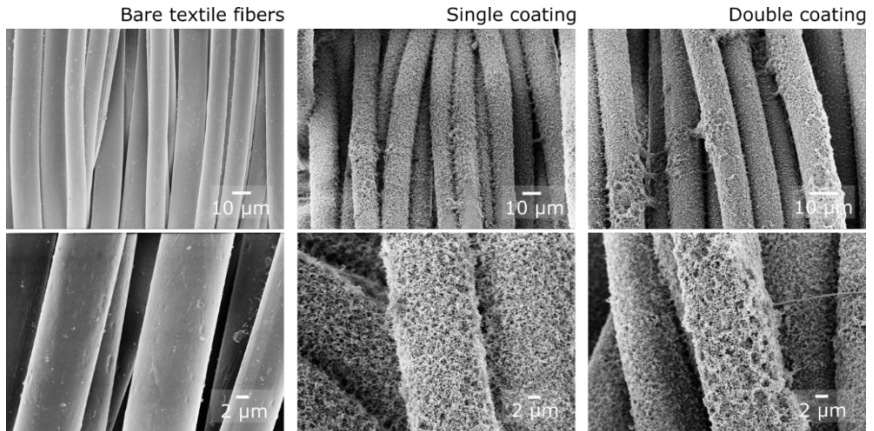


Figure 20: SEM images of polyester fibers before coating, after a single coating process (1-step), and after a double coating process (2-step), each shown at two magnifications.

3.1.3.2 Coating of Metal Alloys with Silicone Nanofilaments⁵

Anodized titanium cantilevers (as described in Section 3.1.1) were first rinsed with acetone and deionized water; samples were then rinsed for 30 minutes in an ultrasound bath in a 10% v/v aqueous solution of Deconex 11 Universal (Borer Chemie AG, Switzerland), an alkaline detergent, at 40 °C. After this step, the cantilevers were abundantly rinsed with deionized water and dried using a dry N₂ stream. Samples were introduced into a custom 6.6 L reaction vessel (G. R. J. J. Artus et al., 2006; Zimmermann et al., 2004), and were exposed to a relative humidity RH = (36 ± 2)% at room temperature

⁵ The following methods description was reprinted from (Laroche et al., 2021) under the Creative Commons license CC BY 4.0.

$T = (22 \pm 1) \text{ }^\circ\text{C}$ for 1 hour, after which a mixture of 2.25 mmol of trimethoxymethylsilane (TMMS, 98% purity, Sigma-Aldrich Chemie GmbH, Germany) and 0.75 mmol of trichloromethylsilane (TCMS, 98% purity, Sigma-Aldrich Co., USA) was introduced. The mixture was left to react for 4.5 hours following the DAGS mechanism (G. R. J. Artus et al., 2017). Samples that would not undergo subsequent fluorination were annealed at $200 \text{ }^\circ\text{C}$ for 16 hours.

Anodized aluminum cantilevers (as described in Section 3.1.1, but anodized as-received instead of after polishing) were rinsed with acetone and deionized water, after which they were immersed for 30 s in a 1 M NaOH aqueous solution to obtain hydrophilic $\text{Al}(\text{OH})_3$ on their surface. Surface pH was then brought below the isoelectric point of $\text{Al}(\text{OH})_3$ ($\text{pH} = 7.7$) (Gayer et al., 1958) by immersing the samples in deionized water for 10 s. Samples were then abundantly rinsed with running deionized water and dried using a dry N_2 stream. Similar to the process for titanium substrates, aluminum samples were introduced into a custom 6.6 L reaction vessel (G. R. J. Artus et al., 2006; Zimmermann et al., 2004), and were exposed to a relative humidity $\text{RH} = (36 \pm 2)\%$ at room temperature $T = (22 \pm 1) \text{ }^\circ\text{C}$ for 1 hour, after which a mixture of 2.25 mmol of TMMS and 0.75 mmol of TCMS was introduced. The mixture was left to react for 2 hours following the DAGS mechanism (G. R. J. Artus et al., 2017). Samples that would not undergo subsequent fluorination were annealed at $200 \text{ }^\circ\text{C}$ for 16 hours.

SNFs are non-reactive to most chemical functionalization, and therefore need to be activated to introduce reactive groups on their surfaces. Surface activation was accomplished by introducing OH functionalities through exposure of the samples to O_2 plasma (Femto plasma chamber, Diener Electronics, Germany) at 50 W power for 5 min. Fluorination was then carried out utilizing the same setup and procedure used for SNF growth: samples were exposed to a N_2 atmosphere with $\text{RH} = (25 \pm 3)\%$ and $T = (22 \pm 1) \text{ }^\circ\text{C}$ for 1 h, after which the reaction vessel was sealed and an amount of

trichloro(1H,1H,2H,2H-perfluoro-1-octyl)silane (97% purity, Sigma-Aldrich Co., USA) corresponding to 0.26 mmol per cantilever was introduced and left to react for 16 hours. The same procedure was followed for both titanium and aluminum cantilevers.

Lubricant infusion on one of the surfaces was performed after the sample was instrumented and placed in the ice adhesion testing setup (described in detail in Section 3.3.2), since the slipperiness of the surfaces could have prevented an appropriate fastening of the samples and strain gauge attachment. During ice adhesion testing, lubricant replenishment was carried out in the same fashion between each icing condition (every fourth icing/de-icing cycle). Over-filled lubricant-infused surfaces were fabricated by dropwise application of excess lubricant (PDMS oil, 100 cSt at 25 °C, Sigma-Aldrich Co., USA) on the top edge of the vertically held samples, allowing for gravitational spreading, which was facilitated by localized compressed air. A homogeneous layer of lubricating oil was achieved within minutes. Once the lubricated sample was subjected to airflow in the wind tunnel, the excess lubricant would be sheared off by aerodynamic forces (Howell et al., 2015). This method, while entailing loss of the excess lubricant, was much closer to what might be employed in a real-world scenario compared to other commonly reported infusion methods, such as hemi-wicking or dip-coating.

The names of the samples used in this thesis are listed in Table 3. SNF were grown on AA2024 and Ti6Al4V alloys, and tested either as-received (Ti6Al4V SNF, and AA2024 SNF), after fluorination (denoted by fSNF), or after lubricant infusion (denoted by LubSNF).

Table 3: Sample names of silicone nanofilament coatings on metallic substrates.

Name	Substrate	Description
Ti6Al4V SNF	Ti6Al4V	Anodized with TiO ₂ nanotubes, coated with SNFs
Ti6Al4V fSNF	Ti6Al4V	Anodized with TiO ₂ nanotubes, coated with SNFs, fluorinated
Ti6Al4V LubSNF	Ti6Al4V	Anodized with TiO ₂ nanotubes, coated with SNFs, infused with silicone oil 100 cSt
AA2024 SNF	AA2024	TSA anodized, coated with SNFs
AA2024 fSNF	AA2024	TSA anodized, coated with SNFs, fluorinated

3.2 Primary Characterisation

The metrics of interest for the study of icephobic surfaces to date have been primarily how a surface interacts with water, and its topology. Common techniques for studying both are employed here, including contact angle goniometry, stylus profilometry, and scanning electron microscopy.

3.2.1 Contact Angle Measurement

Wetting characterization of samples was carried out with a Krüss DSA25 goniometer (Krüss GmbH, Germany), using deionized water as a test liquid. Contact angle (CA) and roll-off angle (RoA) were evaluated using a constant droplet volume of 10 μL and, for RoA, a constant tilting speed of 1°/s. All wetting measurements took place in air at a controlled relative humidity and temperature of (50 ± 2) % and (22.4 ± 1) °C, respectively.

3.2.2 Surface Roughness Measurement

A stylus profilometer (Bruker Dektak XT, Bruker Corporation, USA) was used with its accompanying software (Bruker Vision 64). At least three independent measurements were taken at distant and random

locations on the substrates. The values reported are an average of those three or more measurements and the error is the standard deviation. Signal filters and length settings were according to ISO 4288:1998 and ISO 3274:1998. Specifically, the stylus tip radius was $2\ \mu\text{m}$, cut-off length was 0.8 mm, length considered was 4 mm, travel length was 4.8 mm, and the short cut-off length was $2.5\ \mu\text{m}$. A stylus force of 1 mg was used with the software's N-Lite feature for minimizing surface scratches from the stylus. The spatial resolution was $0.05\ \mu\text{m}/\text{point}$. The measurements were done in a lab with a controlled relative humidity and temperature of $(50 \pm 2)\ \%$ and $(22.4 \pm 1)\ ^\circ\text{C}$, respectively.

3.2.3 Scanning Electron Microscopy

Surface morphology was evaluated with Scanning Electron Microscopy. Samples were cut to shape (approximately 13 mm by 13 mm square pieces), mounted on aluminum stubs with Leit-C conductive carbon glue (Sigma-Aldrich, USA) and coated with a layer of Pt of nominal thickness 12 nm using a Safematic CCU-010 sputter coater (Safematic GmbH, Zizers, Switzerland). A rotating planetary stage ensured uniform coating of the nanostructure. SEM micrographs were then captured with a Zeiss GeminiSEM 450 microscope (Carl Zeiss AG, Germany), using an accelerating voltage of 5 kV. Brightness and contrast of images was uniformly adjusted after acquisition.

3.3 Icephobicity Characterisation

The measurement of ice adhesion strength as a basis for the quantification of icephobicity begins with a method to form ice. The method used here to generate ice is the impact of a cloud of accelerated supercooled water microdroplets. The tool to create this condition for ice formation is an icing wind tunnel. After a general introduction to the icing wind tunnel, some details are provided

about the test section uniformity and the expected size profile of impacting droplets. Then, the ice adhesion strength measurement equipment is described along with the testing protocol. The ice adhesion strength measurement setup's use was expanded to include measurement of the elastic modulus of ice. That protocol is also described hereunder.

3.3.1 Icing Wind Tunnel

The properties of ice encountered in flight is different from that which is frozen from a steady pool of water. Ice formed by steadily decreasing the temperature of water will vary according to the purity of the water. Ice encountered in flight is formed by high-purity water, but an additional mechanism is present, accretion. Impacting supercooled droplets accrete on a surface because the droplets freeze on impact in a timescale comparable to its contact time with the surface. Depending on the speed, frequency, and temperature of impact, as well as the size of individual droplets, the accreted ice can become highly porous and opaque (rime ice) or dense and clear (glaze ice). Rime and glaze ice are at two extremes of the ice-type spectrum with all types of mixed ice between them. With that knowledge, and with the pioneering work of (Lewis, 1947), in-flight ice could be simulated on-ground thanks to wind tunnels that could mimic flight airspeeds and temperatures. These wind tunnels are known as icing wind tunnels. Their size and performance capabilities depend largely on their purpose, the smallest for educational purposes, and the largest for certification and applied research.

Aircraft icing research debuted in an effort to address safety issues with postal service aircraft. Once a suitable mitigation system had been developed, the topic was largely abandoned for many years. It had once again gained momentum with the encounter of different ice types and with the need to understand how ice shapes affect the aerodynamic performance of an airfoil. Nowadays, the focus is on novel ice protection systems, modelling of glaze ice, ice crystal icing,

and supercooled large droplet icing. Novel ice protection systems are of particular interest to commercial aircraft manufacturers because of their potential to reduce the energy consumption of current IPS. Specifically, passive IPS consume no energy as stand-alone systems, and can provide protection to non-critical surfaces to where heat is not normally supplied.

The icing wind tunnel used for the work in this thesis is depicted in Figure 21. The test section measures $10 \times 15 \times 30 \text{ cm}^3$ and can produce airflow conditions up to speeds of 140 m/s and at temperatures down to -40°C . The test section is composed of an aluminum frame with removable polycarbonate walls. The walls are typically machined with holes to support various test fixtures. The wind tunnel is primarily made of wood because of its insulating properties and for facile modification. A horizontally aligned spray manifold holds three air atomizing nozzles upstream of the test section. These nozzles produce clouds of water microdroplets with a mean volumetric diameter (MVD) of $20 \mu\text{m}$ and resulting in a liquid water content (LWC) of up to 2.0 g/cm^3 .



Figure 21: Image of the icing wind tunnel used for this thesis.

Airspeed is measured in the test section by a Prandtl-Tube. The sensor has one total pressure port, five static pressure ports, and a total temperature K-type thermocouple. The variation of airspeed in

test section has been measured by taking sensor measurements in a grid of points within the cross section. The pressure profile is shown in Figure 22. The velocity was uniform across the horizontal axis. It was also uniform in the vertical direction except in proximity to the top wall. The presence of an aerodynamic boundary layer caused that non-uniformity. The same boundary layer is believed to exist at the bottom wall, but the sensor could not be placed close enough due to geometrical factors of the sensor. Similarly, due to the design of the test section walls, the probe could not be placed close enough to the side walls to measure the boundary layer thickness.

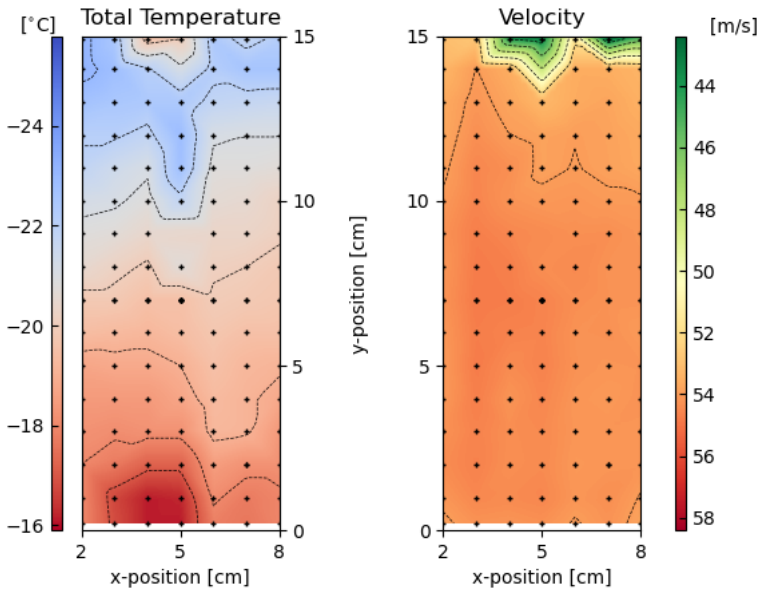


Figure 22: Total temperature (left) and velocity (right) maps over the cross-section of the test section. Adapted from (Wachsmann, 2019).

The total temperature profile, plotted in Figure 22, shows a temperature gradient most prominently in the vertical direction. The

temperature gradient is caused by the loss of pressure along the heat exchanger pipeline. The center portion of the test section is regularly used, where the temperature range is within 1 °C.

The liquid water content in the test section is measured prior to a testing campaign. The conditions that produce a desired liquid water content are the same that are used during testing. The measurement of liquid water content is done by the icing blade method, described in the SAE icing wind tunnel calibration best practices report (SAE Aerospace, 2003). All tests are done at a temperature of -17°C. For each wind speed and water/air injection flow rate, ice is accreted on the edge of a metal ruler for a measured amount of time. The average ice thickness grown over a length of interest on the blade after a certain time is used to calculate the liquid water content in the test section. The advantage of this method is that it is repeatable and allows for the measurement of many different conditions in a short amount of time, with little equipment. By relying on this method, it is assumed that the entire test section, or at least the entire area of interest in the test section experiences the same liquid water content.

3.3.1.1 High Speed Impact of Supercooled Picolitre Droplets

Airborne microdroplets in a high-speed flow may or may not impact a stagnation surface near the freestream velocity, depending on their momentum, hence, their mass. Larger droplets will tend to impact at a higher velocity, and smaller droplets may not impact at all due to their inability to cross streamlines. Surfaces exposed to a supercooled droplet cloud in an icing wind tunnel will therefore experience a range of droplet impact speeds, limited by the freestream velocity.

(Deng et al., 2009) have proposed a model to predict whether a textured surface will be completely wetted, partially wetted, or completely un-wetted by an impacting droplet. Since it is expected that the wetting state of an impacting droplet will influence ice adhesion strength, their model is considered here. Figure 23a shows

the limits for total non-wetting, partial wetting, and total wetting depending on the pore diameter of a generic porous surface and droplet impact speed. For a pore diameter smaller than 100 nm, the total non-wetting regime is limited to droplets impacting at 5 m/s. Any droplets impact at speeds above 75 m/s are predicted to completely wet the structure, resulting in an expected increase in ice adhesion strength. Such was observed experimentally for the case of superhydrophobic titanium, Ti6Al4V nTiO₂ + PFPE, where the ice adhesion strength for glaze ice (freestream velocity of 80 m/s) was nearly twice as high as for the other ice types (freestream velocity of 50 m/s) and is discussed in greater detail in Section 4.3 below.

The impact area is a stagnation region, which means that air in the vicinity decelerates to null. Heavy particles in the flow will break away from the flow and continue to impact the surface at a speed near the freestream velocity. Lighter particles in the flow will follow air pathlines more closely and will either impact at a much lower speed or will go around the obstacle entirely. The Stokes number ⁶ is a useful indicator of whether a particle is light enough to follow airflow pathlines closely. Conventionally $St < 1$ means that the particles will follow pathlines, whereas $St > 1$ means that they will likely not.

With consideration for the ice adhesion test setup in the icing wind tunnel test section, Figure 23b reveals that droplets below 10 μm in diameter will not impact the surface. Impacting droplets above 13

⁶ $St = \frac{tv}{l}$ where t is the relaxation time of the droplet, v is the freestream velocity of the fluid upstream of the obstacle, and l is the characteristic size of the obstacle. The relaxation time is defined as $t = \frac{\rho D}{18\mu}$ where ρ is the droplet density, D is the droplet diameter, and μ is the kinematic viscosity of the surrounding fluid.

μm in size have been visualized experimentally, and their actual impact velocities vary as a function of their size; larger droplets tend to be faster. Due to their higher momentum, larger droplets skip over air velocity isolines, eventually crashing into the obstacle. Since there are very few droplets in excess of $50\ \mu\text{m}$ in size in our setup, one can conclude that all of the droplet impacts occur at between 50-75% of the freestream air velocity. For 50 m/s airspeed, the range is 25-36 m/s and for 80 m/s airspeed, the range is 40-60 m/s. According to the plot of Figure 23a, impacting droplets will remain in a total non-wetting state even in glaze ice conditions for a surface pore size of 15 nm or less. For the case of Ti6Al4V nTiO₂ + PFPE, whose pore size is around 70 nm, the model predicts droplets will partially wet the structure in both rime and glaze conditions, but closer the total wetting regime for glaze.

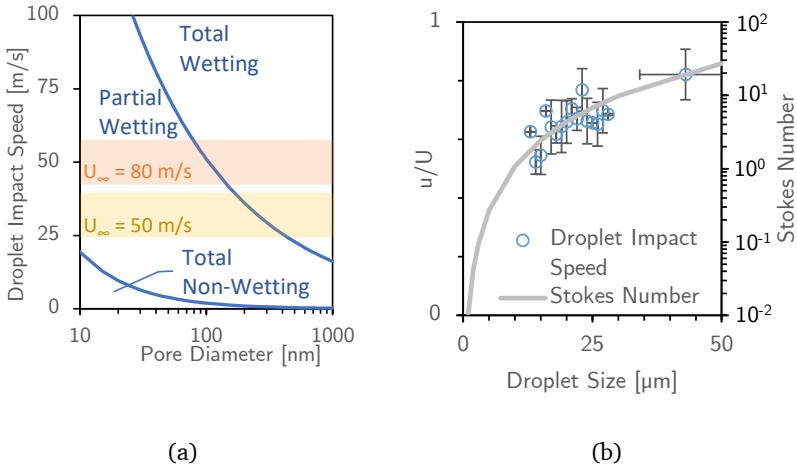


Figure 23: Limits of Cassie-Baxter wetting state for an impacting droplet on a porous surface. (a) wetting state calculations based on the model of (Deng et al., 2009), highlighting droplet velocity ranges used in the present work. The pore diameter in the x-axis is that of an arbitrary porous or nanostructured surface. (b) Dimensionless droplet impact speed (u/U where u is the observed speed of an impacting droplet and U is the freestream airspeed) observed in the icing wind

tunnel on various surfaces, with an overlaid line showing calculated Stokes Number for the range of droplets and speeds observed.

3.3.2 Ice Adhesion Test

The ice adhesion strength test method used by (Raps et al., 2012; Tobias Strobl et al., 2013) has been implemented into an icing wind tunnel test section. The purpose was to test the adhesion strength of a surface to impact ice similar to that seen in-flight but under controlled conditions. With the load actuator mounted directly to the test section, as shown in Figure 24, no manipulation of the ice is needed between accretion and removal, meaning the ice and interface properties are not artificially influenced. Such would have been the case if, for example, the iced specimen needed to be moved from the test section to a fixture in a location, where mishandling could occur, thermal shock from changing environments, or other.

The test consists of a cantilever substrate with a coated surface, held at one end by a clamping plate fixed to an electromagnetic shaker. The coated face of the cantilever is held within the test section of the icing wind tunnel, facing the airflow. The icing wind tunnel is used to create an atmospheric icing environment, resulting in an ice formation on the front face of the cantilever. A counter-drag block behind the cantilever holds the substrate in place against aerodynamic drag forces. A flow deflector located near the substrate entry port of the test section controls the length of ice formed on the cantilever substrate. Once sufficient ice has been grown, the icing wind tunnel is shut off, and the electromagnetic shaker vibrates the iced cantilever at its first resonant frequency. The vibration amplitude is steadily increased until the ice breaks off. A strain gauge mounted to the back face of the cantilever monitors the vibration amplitude. That reading is later used for calculating the interfacial shear stress at the moment of ice delamination.

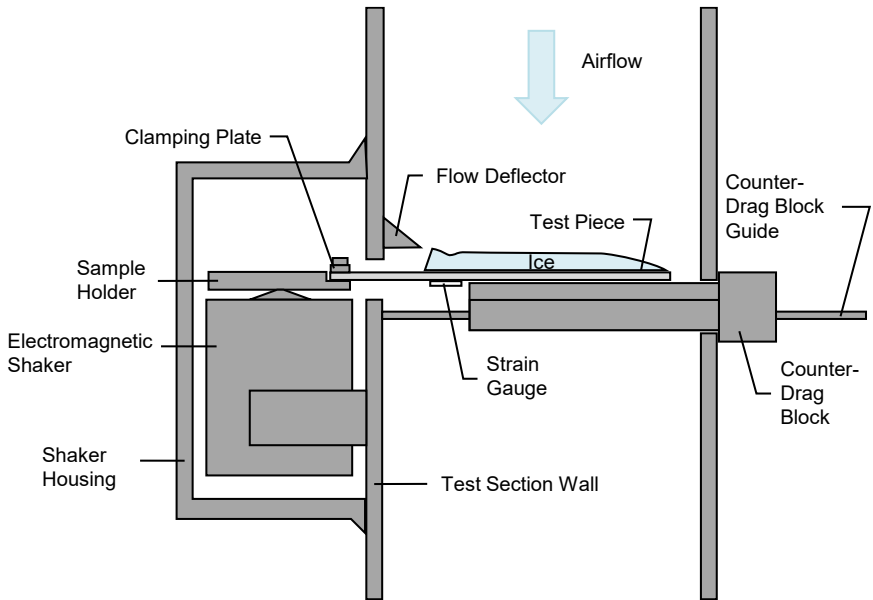


Figure 24: Ice adhesion strength measurement setup in the iCORE icing wind tunnel.

The system can be modelled as a bi-material cantilever beam. The deflection of the cantilever is dependent on the type and magnitude of the load on the beam. The stress state within the beam is revealed by its deflection. The deflection of a cantilever beam vibrating at its first natural frequency resembles that of a beam subject to a static end-point load. Figure 25a illustrates the distribution of shear stress, τ , and bending stress, σ , as a function of through-thickness position in a bi-material cantilever under end-point loading. The maximum shear stress and minimum bending stress are at the neutral axis. For an ideal ice adhesion strength test, the neutral axis would be at the bi-material interface. The position of the neutral axis can be expressed as eccentricity (or distance from the interface), e , as shown in Figure 25b, along with other experimental parameters used for calculating the interfacial shear stress.

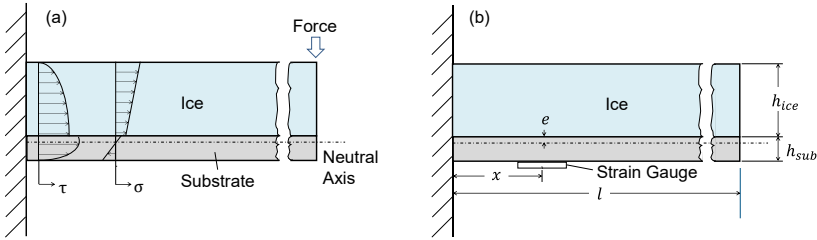


Figure 25: Diagram of geometric parameters used for calculating interfacial shear stress (a), and the cross-section stress distributions for shear and normal stress in a point-load scenario (b).

Under a point-load at the free end of a cantilever beam, the Euler-Bernoulli beam model leads to a description of the interfacial shear stress at the interface of a bi-material beam as:

$$\tau_{interface} = C \times \varepsilon_a \quad (2)$$

Where C is a geometric parameter described below, and ε_a is the strain along the x direction at a point, a , along the beam.

$$C = \frac{E_{ice}(h_{ice}^2 + 2h_{ice}|e|)}{2(x-l)(h_{substrate} - e)} \quad (3)$$

Where E_{ice} is the Young's Modulus of ice, h_{ice} is the thickness of the ice layer, e is the eccentricity of the neutral axis with respect to the interface, x is the position of the strain gauge as a distance from the fixed end, l is the length of the cantilever, and $h_{substrate}$ is the thickness of the substrate. The eccentricity is computed according to:

$$e = \frac{\left(h_{substrate}^2 - \frac{E_{ice}}{E_{substrate}}h_{ice}^2\right)}{2\left(h_{substrate} + \frac{E_{ice}}{E_{substrate}}h_{ice}\right)} \quad (4)$$

Where $E_{substrate}$ is the Young's Modulus of the substrate material.

The equation presented in this format because for a given combination of substrate and ice material and thickness, the parameter, C , is ideally constant for every test. The main variable is the strain at position, x . That strain is measured by a commercial strain gauge (Hottinger Baldwin Messtechnik, Germany). The 120 Ω , 4-wire resistor was connected in a quarter-bridge to a strain gauge amplifier (Hottinger Baldwin Messtechnik, Germany), linked by a commercial software to a computer. Actuation was given by an electromagnetic shaker to which the substrate was fastened. The shaker was controlled by a vibration amplifier. Early experiments included a closed-loop feedback vibration controller, but with time the accelerometer frequently detached. The system was replaced by an open-loop analog vibration controller for all experiments on AA2024 Rough and the results in Section 4.9.

The testing procedure, plotted on a timeline in Figure 26, included 9 phases:

1. Preparation of the substrate without airflow and at room temperature.
2. Ramp up of the air speed and cooling of the air.
3. Steady test conditions.
4. Introduction of atomized water droplets into the airflow upstream of the test section.
5. Cessation of the flow of water droplets into the air.
6. Holding the test conditions for 2 minutes to allow for the ice to stabilize.
7. Ramp down of the air flow and cooling power.
8. Ice detachment measurement by vibration of the substrate.
9. Removal of ice remnants on the substrate and in the test section.

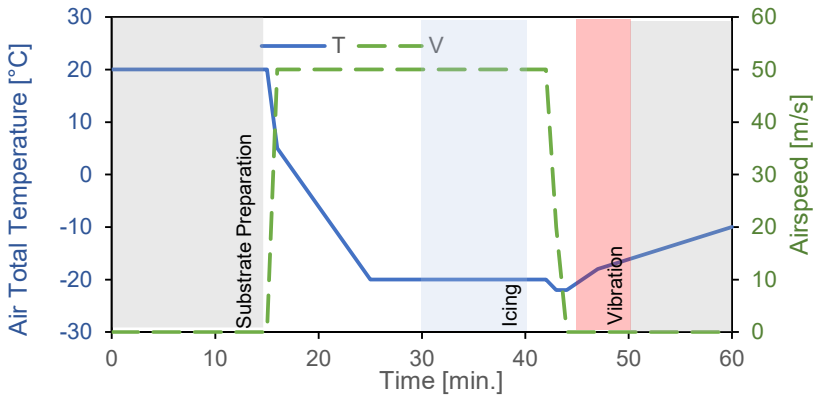


Figure 26: Ice accretion procedure temperature and velocity cycle.

During Step 8, a gradually increasing voltage was supplied to the electromagnetic shaker. The amplitude of vibration, monitored by the strain gauge mounted to the substrate, was increased steadily until a sharp spike was detected. The increase in amplitude was for early test sequences due to a frequency sweep, where the amplitude would naturally increase as the first harmonic frequency was approached. In later tests, a constant frequency (the first natural frequency of the system) was selected based on prior experiments, and the voltage supplied to the shaker was simply increased. After delamination of the ice was detected, the test was complete. The substrate would then be cleaned from remaining ice and moisture by compressed air. The rest of the test section, including flow deflectors, Prandtl tube, and the walls of the converging section upstream of the test section were also cleaned from ice. The calculation of ice adhesion strength was done after a series of measurements were taken.

The calculation of ice adhesion strength, through the above equations, required two experimental observations: the thickness of the ice, and the strain reading just prior to ice delamination. It was

previously stated that the geometric parameter, C , was constant for a given system. Nominally, that is true, however, the thickness parameters are to the third power and are therefore highly influential in the final shear strength calculation. Small differences in accreted ice thicknesses needed to be considered. They were measured post-test by images taken from a calibrated top-view camera. The strain at interfacial failure was taken as the half-amplitude of an average of the 5 peaks and valley leading up to the sudden spike in strain reading.

Four types of ice were typically tested, obtained by four icing conditions listed in Table 4. They cover two temperatures, two airspeeds, and three liquid water contents. The test matrix was first used in the European project, STORM, and then reused for the Canadian-European project, Phobic2Ice. The ice types, also described in Section 1.1.1, are a function of these parameters. Colder conditions lead to rime ice, warmer conditions lead to glaze ice, and temperatures in-between lead to mixed ice. Total temperature is reported here because that is the expected temperature of impacting droplets (that is, the temperature of air when it comes to a stop such as at the stagnation point of an obstacle in the airflow).

Table 4: Icing conditions used in the ice adhesion test.

Ice Type	Total Temperature, Air [°C]	Airspeed [m/s]	Liquid Water Content [g/m ³]
Rime	-20	50	0.3
Mixed/Rime	-20	50	0.8
Mixed/Glaze	-5	50	0.3
Glaze	-5	80	1.0

The resulting ice accretions from these conditions are shown in Figure 27. Opaque, reflective surfaces appear bright and transparent surfaces appear dark in the figure. Rime ice appears slightly darker than mixed/rime because different exposure settings were used to

avoid oversaturating pixels in the camera sensor for the case of rime ice. For aerodynamic reasons, the ice shape is non-uniform along the length of the beam, especially near its edges. The left edge includes a slope and a thickness overshoot as a consequence of the flow deflector illustrated in Figure 24. The accretion rate was highest near the center-span and was compensated by sequential closing of the spray nozzles, i.e. the center-nozzle was the first to be closed. The influence of ice shape on the measurement of ice adhesion strength is discussed in Section 4.5.4 below.

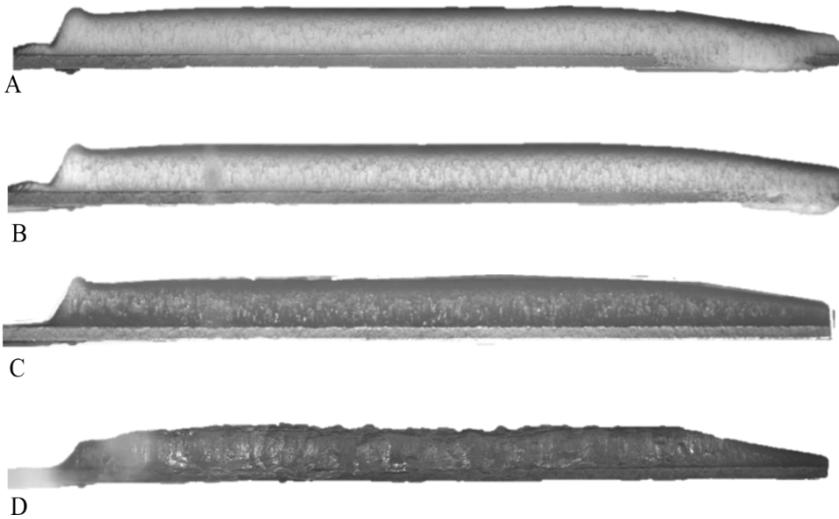


Figure 27: Typical ice accretions grown in the icing wind tunnel on an aluminum substrate in conditions listed in Table 4, with (a) rime, (b) mixed/rime, (c) mixed/glaze, (d) and glaze ice. Length of the iced cantilevers shown is 85 mm, and with an average ice thickness of 4.5 mm.

To summarize the ice adhesion strength measurement setup is a cantilever that is shaken at its first natural mode. The peculiarity of this setup is that the cantilever thickness is non-uniform. It includes

two heterogeneous materials with different mechanical and thermal properties. One of the materials' properties are known (the substrate's), however those of ice are only approximated from literature. Using the conveniently simple concept of cantilever bending, one can determine some of the mechanical properties of the ice component.

3.3.2.1 Measurement of the Young's Modulus of Ice

The Young's modulus of impact ice was measured by cantilever flexure. Ice was grown onto a rectangular aluminum prism-cantilever. The ratio of strain measured on the aluminum to total deflection of the iced aluminum was used to implicitly determine the Young's Modulus of ice.

The use of a cantilever to determine the elastic modulus of a coating has been reported previously (Rybicki et al., 1995). This method, however, requires that the multiple strain gauges be installed on both the substrate and the coating, and that the coating have a uniform thickness. The nature of ice grown in the icing wind tunnel exceeds these thickness limits in magnitude and uniformity. The installation of a strain gauge onto ice would modify the properties of the ice due to unavoidable melting of the ice and would thereby defeat the purpose of the measurement.

A cantilever made from aluminum 2024 alloy, measuring $125 \times 13 \times 1.6 \text{ mm}^3$, and bearing a linear strain gauge along its length axis at the 45 mm position, was installed in the ice adhesion test rig described in Section 3.3.2. A CCD camera with a 35 mm lens was placed directly above the cantilever at a height of 50 mm, looking down onto it. The main measurements necessary for the calculation of Young's Modulus came from image data from this CCD camera, and from strain readings. After ice was accreted on the front face of the cantilever, an image would be taken. The image would be later analyzed to extract a precise ice thickness profile. Once this first

image was captured, the fixed end of the iced beam would be vibrated by means of the electromagnetic shaker to which it was fastened. During the constant-frequency vibration, the strain reading would be recorded at a rate of 2400 Hz, while the camera would capture a video at a frame rate slightly offset from the vibration frequency. For example, if the cantilever was vibrating at 60 Hz, the camera frame rate was set to 60.1 Hz. The offset created the illusion of a few continuous vibration cycles; however it was in reality a compilation of different instants during many vibration cycles. The strategy is shown graphically in Figure 28, where the hypothetical strain gauge signal is shown with a frequency of 60 Hz, and the times at which images were captured at 65 Hz. A large difference in frequency is shown here merely for clarity of illustration, but the actual difference used during measurements was on the order of 0.25 Hz.

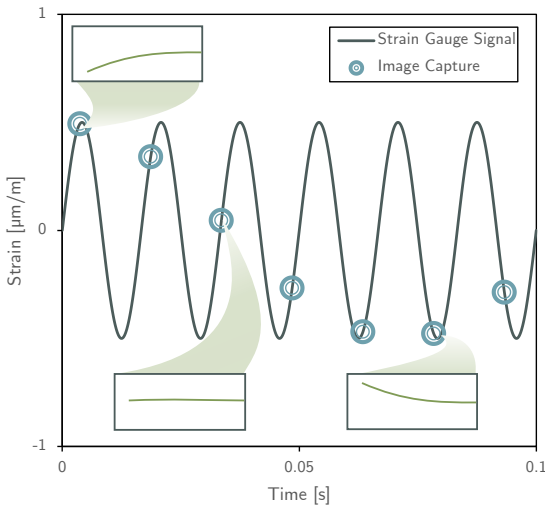


Figure 28: Illustration of camera synchronization to capture sequential deflection positions during cantilever vibration. Inset figures show the cantilever deflection shape associated with maximum and minimum deflections.

The software, ImageJ (NIH, Bethesda, MD), was used to calibrate the image special resolution, then get the coordinates of points placed along the ice profile. The free edge of the cantilever was used as the reference where $x = L = 125\text{ mm}$, and the front-facing surface of the cantilever on a bare section was the $z = h_{\text{substrate}} = 1.6\text{ mm}$ reference. Once the ice thickness coordinates were extracted, they were compared to the reference coordinates to convert them to the coordinate system with the origin at the rear, fixed corner of the cantilever.

The profile coordinates were used to create the geometry in a finite element analysis (FEA). COMSOL Multiphysics® was used to solve the finite element model based on the static structural mechanics module with a Multifrontal Massively Parallel Sparse direct Solver (MUMPS). Probes were placed at the position of the strain gauge during the experiment ($x = 45\text{ mm}$ from the fixed end). The probe monitored the x -component of strain, and the y -component of displacement. Another probe was placed on the substrate at the rear corner of the free end to monitor the y -component of displacement. A parametric solver was used to cycle through several values of E_{ice} . The strain, and deflection values for each E_{ice} were extracted from the results and processed in Microsoft Excel. Here, the same calculation was done as that during experiment.

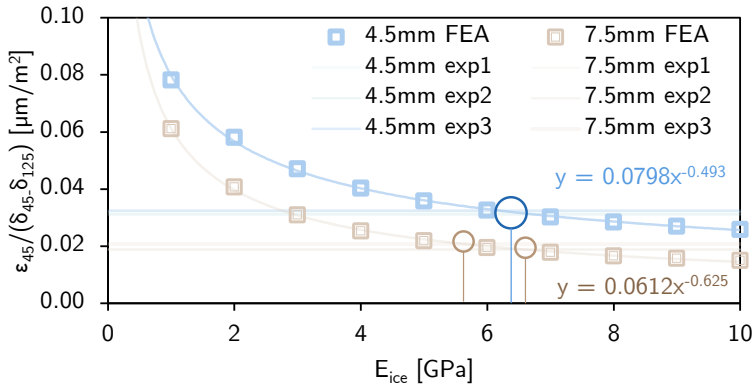


Figure 29: Example of the determination of E_{ice} using the intersection of experimental results with parametric FEA. Equations shown are those describing a power-law trendline fitting FEA curves. Experimental data points are shown as constant lines. Encircled regions show where FEA results intersect with experimental results, leading to the determination of an E_{ice} for each experimental data line. The strain/deflection ratio, characteristic of a coated cantilever, is plotted on the y-axis against possible elastic moduli of ice on the x-axis. Here, the modulus determined for 4.5mm-thick ice is 6.4 GPa and that for 7.5mm is 5.6 GPa and 6.6 GPa.

3.4 Durability Characterisation

Aircraft exterior surfaces are exposed to conditions generally considered aggressive for surface coatings. Large temperature fluctuations, high speed particle impacts (liquid and solid), UV exposure, and corrosive environments are typical for such a surface. For evaluating potential aircraft coatings, accelerated durability tests are used. These tests consist of exposure to typical conditions for a long period of time, or exposure to more severe conditions for a shorter period of time with the purpose of getting an indication of whether a coating will fail within the typical maintenance period of an aircraft. In this thesis, only accelerated rain erosion tests on superhydrophobic coatings are presented. Coatings that were

expected to be more sensitive to mechanical damage were only subject to water droplet clouds in the icing wind tunnel for extended periods.

3.4.1 Water Droplet Cloud Exposure

A NACA 0012 shape was used for exploring the effect of different pressure sites, such as stagnation, suction, and pressure on the durability of silicone nanofilament-coated textiles. This configuration was tested only in a 0° -angle of attack, and the absence of any camber meant the pressure and suction sides were not effective as such; they were just for designation and labeling. Fabrics were placed mid-span of the airfoil and covered up to the 45-mm chord-wise position. Three identical superamphiphobic fabrics were tested in this configuration, illustrated in Figure 30.

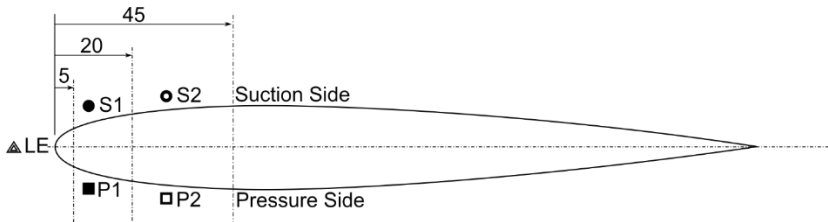


Figure 30: Drawing of the NACA0012 support with 180 mm-chord length and labels for positions on the fabrics. LE: leading edge, or stagnation line; S1, S2: suction side; P1, P2: pressure side. Reprinted from (Laroche, Ritzen, et al., 2020) under the Creative Commons License, CC BY 4.0.

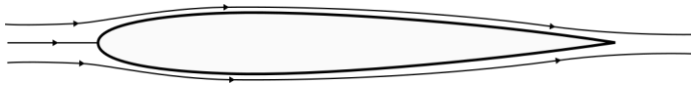
The environmental conditions that the fabrics were exposed to are listed in Table 5. For the two used configurations, above freezing and below freezing air temperatures were tested. Airspeeds ranged from 20 to 120 m/s for the airfoil. The airfoil shape made it such that the fabric's effective incident angle with air ranged from 0° at the maximum airfoil thickness (S2 and P2 in Figure 30), to 90° at the

stagnation line (LE in Figure 30). The total duration of exposure was in intervals of 10 minutes, and cumulatively until 50 minutes. Instead of using a fixed liquid water content (conventional metric for the concentration of water droplets in clouds), a fixed volume flow rate of water of 10 cm³/min was introduced into the air through the air atomizing nozzles. In doing so, the resulting mass impingement rate of water droplets remained constant despite variations in airspeed. The difference in droplet impact rate between a constant liquid water content and constant feed rate is subtle for the range of conditions tested (liquid water content was between 0.25 and 0.36 g/m³). The leading-edge portion of the airfoil was subjected to an impact rate of 4 to 10 droplet impacts/second airspeeds of 50 and 120 m/s respectively, which for an exposure of 10 minutes accumulated to 2500 and 6200 impacts respectively. For the total of 50 minutes of exposure at progressively increasing airspeeds, the number of droplet-impacts over the leading edge of the airfoil is estimated at 18000.

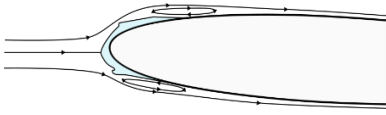
Table 5: Conditions used for icing wind tunnel durability testing.

Total Air Temperature [°C]	Air Velocity [m/s]	Angle of Attack [°]	Duration of Cycle [min.]	Total Duration of Exposure [min.]	Volume Flow Rate Water [cm ³ /min.]
+20	20-120			50	
+20	95	0 ± 2	10	50	10
-3	50			40	

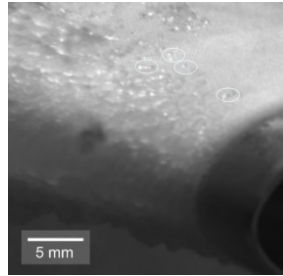
The pathlines around the NACA profile were expected to be as shown in Figure 31a. With a tolerance of 2° on the angle of attack, it is more likely that they appeared as in Figure 31b after some ice had accreted. An image of the experimental condition using icing is included in Figure 31c.



(a)



(b)



(c)

Figure 31: (a) Pathlines over NACA 0012 iced airfoil sample holder at 0° AoA with an arbitrarily low Reynolds Number, (b) the same with ice formed on the leading edge at 3° AoA showing slightly asymmetric pathlines with small flow separations immediately downstream of the ice, and (c) Ice formation on the fabric mounted on a NACA 0012 airfoil showing isolated feathery ice grains near the top side (circled) which become more dense and homogenous approaching the stagnation line. Reprinted from (Laroche, Ritzen, et al., 2020) under the Creative Commons License, CC BY 4.0.

3.4.2 Rain Erosion Exposure

The working principle of the rain erosion device is that a jet of water accelerated by a pump to a set velocity is chopped into short segments by a disc with two openings rotating at a set speed. The front heads of the water jets acquire a semi-spherical shape due to surface tension. The jets then impinge on the sample surface that can be tilted at a desired angle of incidence. The number of impacts at the same location can be varied depending on the need and the

coating type: for these tests presented here, the number of impacts ranged between 20 and 6,000. It is operated according to AITM 1-0027, and DEF STAN 00-35, and has been certified ISO/PDTS 19392-2.

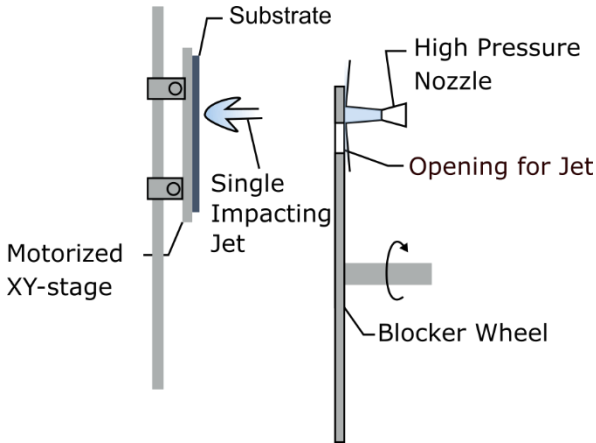


Figure 32: Working principle of the rain erosion test rig, P-JET, showing a single impacting jet near the substrate while the blocking wheel temporarily prevents oncoming water from getting through until the opening passes in front of the nozzle.

The rain erosion durability test is normally meant for paint systems. The typical observational criteria are noticeable cracks in the paint surface, whether the primer beneath the paint is visible, and whether the base material below the primer is visible. Conventionally, a paint with noticeable cracks may marginally pass the test, but it will have failed if the primer beneath it is visible. The test is also comparative since it is difficult to estimate the number of rain droplet impacts an aircraft will be subject to in its lifetime. The coating being tested is compared to a reference, typically an already-certified aircraft paint which has been applied to an aluminum substrate by a coating supplier.

Four quadrants, shown in Figure 33 were tested on each surface-treated plate. The quadrants corresponded to water impact speeds of: 160 m/s, 185 m/s, 200 m/s, and 225 m/s. Five points per row of each quadrant suffered the same number of impacts. The number of impacts changed at each row. The purpose of the five repeated conditions was to measure the effective uniformity of the surface treatment.

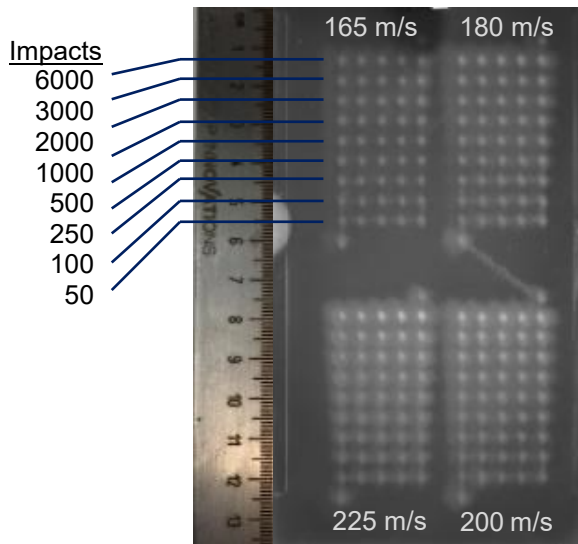


Figure 33: Example of rain eroded surface with severity conditions by quadrant and by row. Each quadrant contains five repeated impact numbers (columns), one jet adjustment spot below the quadrant, and another one on the top of the quadrant.

Most of the surface treatments listed in Table 2 are not categorized as paint systems and therefore could not be compared directly to the certified reference paint. Therefore, the criteria of evaluation were:

- Visible damage, and
- Change in wettability.

Visible damage was any change in colour or texture. Change in wettability was whether any water remained stuck to an eroded surface after the substrate was withdrawn from a beaker of water.

As an example of the wettability test, a rain-eroded diamond-like coating on suspension plasma-sprayed TiO₂ (SS_SPS_DLC1) is shown in Figure 34. The highest number of impacts at the lowest speed is located at the bottom-left of the image. The highest impacting speed is in the rightmost quadrant in the image. Pinned water droplets are shown as shiny bulges. On the quadrant with highest speed impacts, pinned droplets bridge between columns, showing the most extensive surface damage. Undamaged portions do not have water on them because the surface was originally superhydrophobic. The lowest-speed quadrant (bottom-left), the least aggressive condition, shows pinned droplets down to the row with 1000 impacts on each point. To show durability, one would expect no change in wettability (pinned droplets) at this lowest speed.

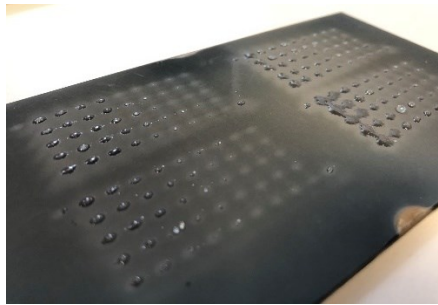


Figure 34: Wetting test following rain erosion on SS_SPS_DLC1, showing water droplets pinned to rain-eroded portions of the surface, and non-eroded portions completely non-wetted.

4 Results & Discussion

The aerospace industry has placed focus on improving the efficiency of ice protection systems on aircraft. In particular, existing ice protection systems can be enhanced with the use of icephobic coatings, but there is a lack of suitable candidate materials and processes for manufacturing such surfaces. To be able to protect the next generation aircraft from icing, the industry requires research into durable and effective anti-icing surfaces.

The following sections show the results of durability and ice adhesion strength tests on novel surfaces for aerospace applications. The focus is on substrates of aluminum alloy 2024, stainless-steel alloy 304, and titanium alloy Ti6Al4V. The first 3 sections cover a large number of different surface technologies. The approach was therefore to get qualitative data that would serve as a guide for more in-depth studies in later sections.

The accuracy of the results of ice adhesion strength tests verified through an uncertainty analysis of the test method. The test method was then enhanced by developing a method for the measurement of the Young's modulus of ice, a critical parameter for minimizing the uncertainty of ice adhesion strength measurements.

The sections continue with a deeper look at the influence of surface properties on ice adhesion strength. The importance of a nano-scale roughness was validated. Novel surfaces that incorporate elements of durability and functionality, silicone nanofilaments, were then tested for durability in the icing wind tunnel, and finally for ice adhesion strength.

4.1 Qualitative Testing of Rain Erosion Resistance

Research has shown that ice adhesion strength is directly correlated to receding contact angle on flat surfaces (Meuler, Smith, et al., 2010). Tuning the chemistry of a flat surface can produce a maximum achievable receding contact angle of 120° . If the surface topography is also tuned, the receding contact angle can surpass 120° , producing a superhydrophobic surface (Meuler, McKinley, et al., 2010). Since an aircraft exterior is regularly exposed to erosive conditions such as rain droplet impacts, it is important to see whether a coating can remain superhydrophobic following exposure to such conditions. The underlying assumption, of course, is that the ice adhesion results of Meuler et al., 2010 are generally valid for superhydrophobic surfaces as they were for flat hydrophobic surfaces.

High velocity impacting water jets can severely damage a surface. Attempts have been made to predict a material's liquid impingement erosion properties from primary characteristics, but they have proven inconsistent (Heymann, 1970). The only way to accurately determine a material's rain erosion characteristics is to expose it to a simulated rain erosion environment. The rain erosion resistance on many types of materials has been studied before from a mechanical perspective (Busch et al., 1966), but the materials' wetting properties have never been evaluated following rain erosion exposure. Since superhydrophobicity is closely tied to a surface's micro-scale topography, it would be expected that a change to this topography may alter the surface's anti-wetting properties.

To test this hypothesis, superhydrophobic surfaces prepared by laser patterning, thermal spray, and physical vapour deposition were subjected to accelerated rain erosion, as described in Section 3.4.2.

A pulsating jet erosion test (PJET) (Jonsson, 2007) was used for simulating high-speed rain droplet impacts. To test the effects of rain erosion on the surfaces' anti-wetting properties, tested substrates were dipped in a beaker of de-ionized water and slowly pulled out. Those surfaces to which water remained pinned after the surface was pulled out were considered to have lost their superhydrophobicity. The surfaces that were not wetted by water retained their superhydrophobicity and were considered to have passed the erosion test.

Figure 35 shows an example of a rain erosion quadrant on the series of surfaces tested. Water appeared as a protrusion from the surface accompanied by a shadow and a brighter portion reflecting light. For example, AA_nsIR_CFx showed several pinned water droplets even at the lowest number of impact points (lowest row in the erosion grid), meaning that the coating shows poor durability in rain erosion. The laser-patterned surfaces without post-treatment appeared to be severely damaged by the rain erosion test, even after only 20 impacts (lowest row of the erosion grid). Only SS_nsIR was still superhydrophobic following erosion. SS_psUVs had a few portions of the high impact number areas with water sticking to them, but SS_nsIR was completely non-wetted by water during the post-rain erosion water dip test. Oblique angle deposition (OAD) surfaces, and those with a PDMS coating were completely wetted by water. Structures produced by OAD have a mechanical weakness, since they are columnar and grown at an angle. Their tips are narrow, and therefore susceptible to breakage, in addition, their oblique angle induces a bending stress whenever a load is applied normal to the surface. PDMS coatings generally have weak adhesion to their substrate unless they are covalently grafted, which was not the case here.

When water repetitively impacts a spot on a surface, it can cause cracks. Once water leaks into those cracks, it can locally lift the

coating off of the surface (delamination), which tends to propagate through to a larger area. Therefore, if a coating is easily lifted off a surface, it will be destroyed by rain erosion. Such was the case for the PDMS coating. The OAD surfaces had sharp protruding oxide peaks, which were most likely overstressed during droplet impact. Damage to the OAD microstructure was likely the cause for the surface's subsequent hydrophilicity.

The modified polyurethane topcoat appears to be completely removed by the water erosion jet. All that remained was the primer at up to 3000 impacts. The unmodified polyurethane coating failed in the same way as the modified one. During previous measurements on similar coatings, they were unaffected by this rain erosion test (Edmond F. Tobin et al., 2012). The damage to the control and the modified coatings was due to defects from improper application of the coating.

For all the superhydrophobic surfaces tested in rain erosion, five of them consistently surpassed the test in terms of retaining their superhydrophobicity. These five were: AA_nsIR, SS_nsIR, SS_psUVf, SS_psUV_CFx, and SS_nsIR_CFx. Only the laser-patterned surfaces showed the highest durability. The superhydrophobicity of thermal sprayed coatings deteriorated possibly due to the mechanical fragility linked to their porosity (dense thermal spray coatings are known for their durability, but porous ones are not). Ideally, these durable surfaces also show low ice adhesion strength, which will be explored in Section 4.3 below.

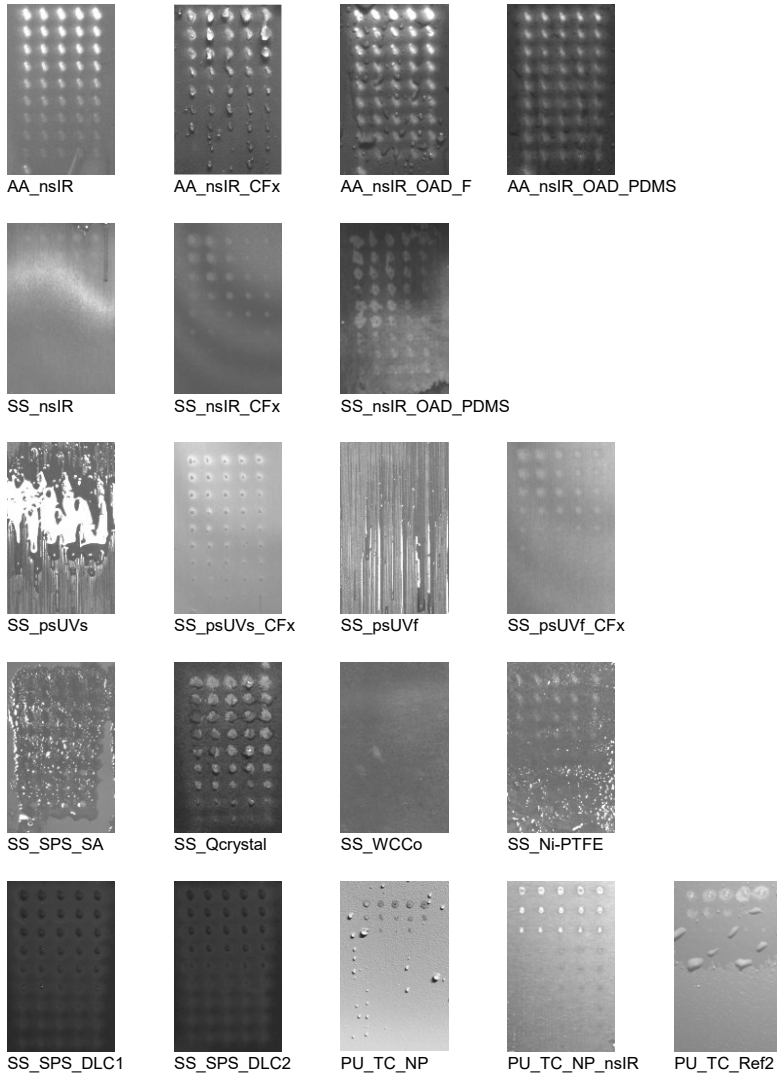


Figure 35: Water droplet pinning test on rain-eroded (225 m/s water jet impact speed) textured superhydrophobic surfaces. Rows of spots according to number of water jet impacts between 20 and 6000. No intended variation along columns of

spots. Edges of wetted areas appear shiny. Surfaces are grouped by material and type of surface treatment, described in Section 3.1.2. First three rows are laser-structured surfaces on aluminum (AA_), and stainless steel (SS_), with post-treatments after structuring such as plasma-enhanced physical vapour deposition of carbon- and fluorine-containing polymer (_CFx), an electron beam evaporation deposition of metal-oxide termed oblique angle deposition (_OAD), and in some cases, fluorination (_F) by exposure to 1H,1H,2H,2H-perfluorooctyltriethoxysilane in a vacuum chamber, or spin-coated polydimethylsiloxane (_PDMS). Fourth row consisted of thermal spray coatings by suspension plasma spray (_SPS) or high velocity oxygen fuel. The final row consisted of diamond-like carbon (_DLC) coatings on suspension plasma sprayed titania, polyurethane aircraft paint (PU_), either unmodified (_Ref2), mixed with nanoparticles (_NP), or mixed with nanoparticles then structured by laser (_nsIR).

Fluorination appears to increase the resistance of laser-patterned surfaces to damage by accelerated rain erosion. Inasmuch, polyurethane basecoats were removed by this erosion test. The excellent durability of polyurethane top coat systems has been shown in previous studies (E. F. Tobin et al., 2011), so it is expected here that the basecoat failed due to the lack of sufficient topcoat, and due to fabrication defects. In any case, the implementation of a new coating in aerospace is a costly and lengthy process. The more novel the coating, the more accurately it must be tested. Therefore, if a coating is needed more urgently, it has a better chance of passing rigorous testing if it is based on an already proven technology, such as it is the case for polyurethane topcoat and clearcoats. The ice adhesion strength investigation begins with modified polyurethane coatings.

4.2 Ice Adhesion on Reference and Modified Aircraft Paint⁷

To be considered for use on a commercial aircraft, coatings need to pass rigorous testing, including among others, durability. Durability testing covers a range of accelerated exposure to aggressive environment meant to deteriorate materials, for example, by erosion, corrosion, or thermal effects. Polyurethane paint is the typical aircraft coating. It is one of the few surface coatings that successfully passed the rigorous durability testing for aircraft exteriors including, temperature cycling, extreme temperature exposure, UV exposure, salt-fog corrosion, erosive chemical exposure, rain erosion, sand erosion, consistency in quality, low flammability, scalability, and aesthetic appeal. The quickest way for a new coating to reach maturity (i.e. for use on a prototype, or Technology Readiness Level (TRL) of 6 (Mankins, 1995)) would be if it were based on the same fundamental engineering of these already mature polyurethane paints. Therefore, a first inspection of conventional polyurethane coatings and some that were reformulated to be icephobic is presented in this section. The purpose of these tests is to obtain a rough estimation of whether it is a direction worth pursuing, for both the coating supplier and for the aircraft manufacturer. For that reason, not all material and surface properties are known.

The road to develop the correct formulation that would meet all those criteria was strenuous and costly. Such would be required of any newly developed icephobic coating destined for the exterior of an aircraft. If legacy coating formulation could be tweaked to make it more icephobic, then the likelihood of the new coating of reaching

⁷ The results in this section have been presented in (Laroche, 2018).

the aircraft production stage would be much higher than for a completely new coating.

Table 6: List of properties of polyurethane paint coatings.

Name	Ra [μm]	Rz [μm]	CA [$^\circ$]	RoA [$^\circ$]
AA2024	0.01 ± 0.01	0.16 ± 0.02	59 ± 1	Pinned
PU_TC_Ref1	0.22 ± 0.07	1.40 ± 0.05	71 ± 1	Pinned
PU_TC_Ref2	0.26 ± 0.06	1.39 ± 0.28	111 ± 1	Pinned
PU_TC_ice	0.01 ± 0.00	0.06 ± 0.00	102 ± 1	Pinned
PU_CC_ice	0.01 ± 0.00	0.05 ± 0.01	99 ± 1	Pinned
PU_TC_NP	2.08 ± 0.39	9.20 ± 1.67	62 ± 6	Pinned

New formulations of polyurethane coatings (PU_TC_ice, and PU_CC_ice) were developed and applied by a commercial aerospace coating supplier (PPG Aerospace, Germany) and were tested for ice adhesion in the present study. Their roughness and water wettability properties are listed in Table 6. To save time, only two icing conditions were tested, rime and glaze, since they represent the two ends of the impact ice spectrum tested in this work (Table 4). The results, plotted in Figure 36, show that the two novel commercial coating formulations tested did not show significantly lower ice adhesion strength than the controls. PU_TC_ice showed slightly lower ice adhesion strength for rime ice as compared to all the controls and PU_CC_ice. Both icephobic coatings shared similar IAS in glaze ice, which was lower than the other paints, but higher than on bare aluminum. PU_TC_NP showed slightly lower ice adhesion strength (2-8%) than PU_TC_Ref2 in both conditions.

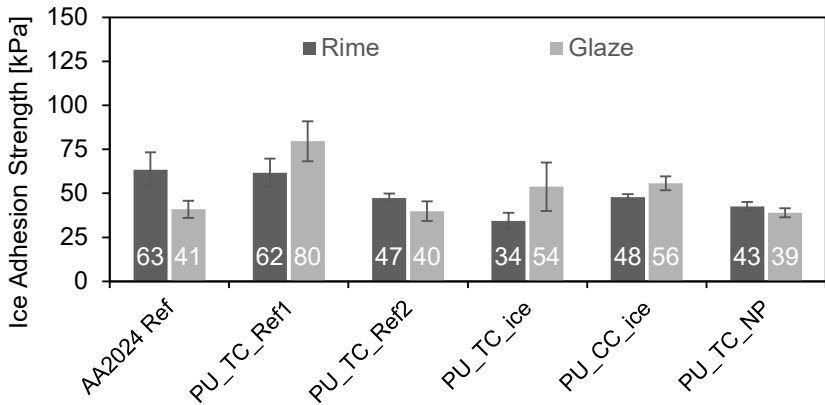


Figure 36: Ice adhesion strength on polyurethane paint formulations for rime and glaze ice. “TC” abbreviates “topcoat,” “ice” abbreviates “icephobic,” “CC” abbreviates “clearcoat,” and “NP” abbreviates “nanoparticles.”

Modified polyurethane paint would be ideal for an icephobic coating for aerospace applications, but until now, the small reduction in ice adhesion does not warrant the effort to replace existing coatings. None of the polyurethane-based coatings tested measured an ice adhesion strength below 20 kPa, which has been selected by some groups as the threshold for low ice adhesion strength (Kreder et al., 2016).

The reformulated polyurethane topcoats showed an improvement in ice adhesion strength as compared to legacy coatings by 30%. Since it is close to the uncertainty margin of ice adhesion strengths, the reduction is considered small. The small advantage in ice adhesion strength is insufficient to warrant re-certification efforts. For lower ice adhesion strength, novel coatings must be considered.

4.3 Ice Adhesion on Reference and Textured Hard Surfaces

Superhydrophobicity is obtained using a combination of low surface energy and a topology that promotes a Cassie-Baxter wetting state. The stability of a Cassie-Baxter wetting state on a surface tends to enhance low ice adhesion strength (S. A. Kulinich & Farzaneh, 2009; Vercillo, 2020). Uniform pillars on a surface can be fabricated by conventional photolithography techniques. These pillars are ideal for fundamental experimental studies that demand precise control over pillar spacing and size. For practical use, these pillars and their substrates are far too fragile. Mechanically stable materials are therefore preferred, such as metals, ceramics, oxides, and some polymers. Techniques such as direct laser writing (Ta et al., 2015) and thermal spray (Sharifi et al., 2016) have been proven as viable methods for producing surface textures that can support a Cassie-Baxter wetting state given a hydrophobic surface chemistry.

Testing a library of different coatings has revealed which surfaces have inherently strong resistance to certain types of durability tests. Hard surfaces show little erosion during rain erosion tests, whereas elastomeric surfaces are the best in sand erosion. Silicone surfaces do not react to UV-exposure and most other chemical exposure tests. Each of these types of potentially icephobic coatings could be useful in particular areas on the exterior of an aircraft.

On manned aircraft, the leading edges of wings and propellers are typically uncoated. One of the reasons is because the leading edges are the areas most susceptible to erosion, and therefore need to be hardened for enhanced durability. Another reason is related to the heat transfer characteristics and enhanced anti-icing efficiency when the surfaces are heated. Since the standard for leading edges is an uncoated metal, that should be the reference for ice adhesion studies focused on in-flight applications. The wetting and roughness properties of reference hard surfaces and a reference

superhydrophobic surface (Ti6Al4V nTiO2 PFPE) are listed in Table 7.

Table 7: Roughness and water wetting properties on standard hard surfaces.

Surface	Ra	Rz	CA	RoA
AA2024 Ref	0.01 ± 0.01	0.16 ± 0.02	59 ± 1	Pinned
AA2024 PFPE	0.02 ± 0.01	0.15 ± 0.04	122 ± 3	Pinned
AA2024 Rough	1.67 ± 0.15	12.38 ± 0.30	57 ± 11	Pinned
Ti6Al4V Ref	0.50 ± 0.03	3.97 ± 0.17	51 ± 1	Pinned
Ti6Al4V nTiO2 PFPE	0.58 ± 0.03	4.40 ± 0.17	166 ± 1	15 ± 6
SS304 Ref	0.17 ± 0.01	1.63 ± 0.15	70 ± 5	Pinned

Three different metals are used here as the controls for comparison. Aluminum 2024 is the most common metal for large aircraft skin or exteriors. Since the skin is typically not load-bearing, this alloy provides the optimal strength-to-weight ratio. More importantly this alloy can be made highly resistant to corrosion, namely when a thick aluminum oxide layer has been grown anodically. Ti6Al4V, also known as grade 5 titanium alloy, is one of the most common titanium alloys found on aircraft. It also has a strong resistance to corrosion, but it stands out mostly for its hardness and therefore resistance to solid-particle erosion. It is commonly used on the leading edges of turbofan blades and on some helicopter rotor blades. Finally, stainless steel is also presented here, although it is not the most common metallic alloy on aircraft, its most notable feature apart from corrosion resistance is its lack of fatigue limit. It is commonly used on highly strained components such as landing gears. The ice adhesion strength on these surfaces was measured by the vibrating cantilever mixed mode test in an icing wind tunnel (detailed in Section 3.3.2).

Figure 37 shows the ice adhesion strength on each of these surfaces as received, except for the aluminum surface which has been polished and anodized. The comparative results for rime, mixed/rime, and mixed/glaze conditions were consistent: stainless steel had the highest ice adhesion strength, followed by aluminum

and titanium. In the glaze icing condition, stainless steel and aluminum both showed decreased ice adhesion strength whereas that of titanium increased with respect to the other conditions. The surfaces were all relatively flat ($R_a \leq 0.5 \mu\text{m}$), meaning that surface roughness did not play a dominant role in the differences of ice adhesion strength, except for in the glaze ice condition. The ice adhesion strength appeared to increase with increasing static contact angle, although the variation in both measurands was within 30% and 18% respectively, making it difficult to confidently draw any conclusion from this trend. (Meuler, Smith, et al., 2010) showed that ice adhesion strength on flat surfaces decreased with increased receding contact angle, equilibrium contact angle, and advancing contact angle. Since the static contact angle typically falls between advancing and equilibrium contact angles, one could expect a similar relation in ice adhesion strength for the mentioned contact angles as with the static one reported here in Table 7. The main message that should be taken from Figure 37 is that the dominant influencers of ice adhesion strength may vary among ice types. Additionally, given that the flat surfaces of different substrates exhibit inexplicably different ice adhesion strengths suggests that there are parameters that influence the test results which have not yet been well understood. These parameters, such as the properties of ice, are studied in greater detail in Sections 4.4 and 4.6. For the remainder of this chapter, the evaluation of ice adhesion strength of novel superhydrophobic surfaces is discussed in the context of reference surfaces of the same substrate material.

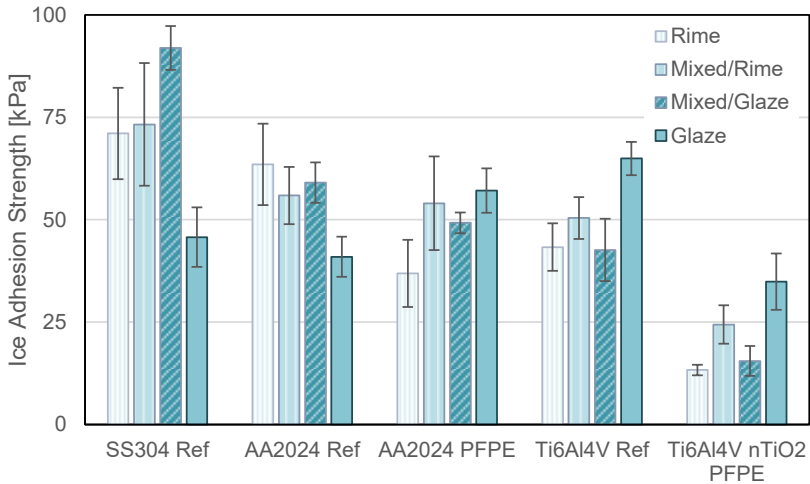


Figure 37: Ice adhesion strength on reference surfaces of stainless-steel alloy 304 (SS304 Ref), aluminum alloy 2024 (AA2024 Ref), and grade 5 titanium alloy (Ti6Al4V Ref).⁸

AA2024 Ref and AA2024 PFPE had the same surface roughness, R_a , of $0.01 \mu\text{m}$. The only difference between them was their surface chemistry. The PFPE coating reduced the surface energy, increasing its repulsion to water (increased static contact angle by 107%). That water repulsion had a measurable effect on ice adhesion strength for rime and mixed/glaze ice. As the air temperature or LWC increased, the reduced surface energy became less effective at reducing ice adhesion strength.

⁸ These results have been presented in (Laroche et al., 2019).

Titanium alloys such as Ti6Al4V are ideal for aerospace applications due to their hardness, strength-to-weight ratio, and corrosion resistance. They are more costly than aluminum alloys both for the raw material and for processing, which is why they are usually reserved for specialty applications. Their most prominent role is on the leading edge of spinning components such as fan blades or helicopter rotor blades. It is possible to grow an anodic oxide in the shape of nanotubes on titanium surfaces (Figure 14, Section 3.1.1). Titania nanotubes, once coated in a perfluoropolyether solution, identical to that mentioned for aluminum, will create a superhydrophobic surface. The combination of the nanotube structure and the low surface energy from the perfluoropolyether make the surface superhydrophobic (Table 7). Figure 37 shows that the ice adhesion strength on Ti6Al4V nTiO₂ PFPE decreased by at least 50% over each condition tested compared to the as-received titanium alloy (Ti6Al4V Ref). In comparison to the anodic oxide grown on aluminum, that on titanium is more robust (Vercillo et al., 2019).

The average surface roughness of the two titanium surfaces was the same. The difference between the two surfaces was in the chemistry and nano-porosity. The fluorination of the nanotube surface decreased the surface free energy, thereby decreasing the equilibrium contact angle. All else barred, the increased contact angle of fluorinated chemistry has been shown to hold for picoliter droplets (Lau et al., 2003), unlike for some natural metal-oxide surfaces (Méndez-Vilas et al., 2009). Next, the nano-porous structure reduced the effective contact area between impacting droplets and the substrate. Reduced contact area on impact has two effects: decreased heat transfer efficiency between droplet and the surface, and less bonding area thereby decreasing the adhesion strength. Heat transfer impedance is normally useful for repelling incoming droplets. Clearly, since ice formed on the surface, the droplets were not repelled. It has been observed that superhydrophobic surfaces can repel some droplets, but microscopic

pinning sites prevent that state from being held (Lengaigne et al., 2019). In any case, a longer dwell time until droplet freezing allows the droplet to fully recoil and perhaps begin to bounce off the surface, reducing its contact area with the substrate. The impeded heat transfer process on an un-heated surface slows supercooled droplet freezing because latent heat of fusion cannot be conductively dissipated into the substrate as quickly as on a highly diffusive surface. The increased ice adhesion strength observed for glaze ice is likely caused by the higher rate of droplet impact, which promoted more complete surface coverage before freezing than in the rime and mixed conditions.

Many of the hard textured surfaces were not severely damaged by rain erosion tests. Of these, several were selected for ice adhesion strength measurements. Some surfaces that showed damage during rain erosion tests were also selected for ice adhesion testing to act as additional data. The samples were selected based on either RoA > 10°, or high durability demonstrated during rain erosion testing. The surface roughness and wetting properties of these surfaces are listed in Table 8.

Table 8: Roughness and water wetting properties of hard textured surfaces tested in the ice adhesion strength rig.

Surface	Ra [μm]	Rz [μm]	CA [°]	RoA [°]
Alu_nsIR_CFx	6.48 ± 0.74	2.84 ± 0.09	175 ± 2	8 ± 2
Alu_nsIR_GLAD_F	9.55 ± 0.35	53.55 ± 3.65	175 ± 2	4 ± 2
SS_nsIR	2.33 ± 0.08	13.47 ± 1.49	114 ± 12	Pinned
SS_nsIR_GLAD	0.19 ± 0.12	2.22 ± 0.15	118	Pinned
SS_psUVs	0.93 ± 0.04	9.97 ± 0.33	175 ± 4	4 ± 0
SS_SPS_SA	8.3 ± 0.11	8.1 ± 1	160 ± 1	1 ± 0
SS_QCrystal	1.6 ± 1.9	76.8 ± 8.9	167 ± 3	5 ± 2
SS_WCCo	1.8 ± 0.6	10.7 ± 2.7	51 ± 3	Pinned
SS_HHS	7.6 ± 1.4	40.8 ± 9.7	159 ± 3	Pinned
SS_SPS_DLC1	14 ± 1	72 ± 5	155 ± 0	3 ± 1
SS_SPS_DLC2	13 ± 1	77 ± 6	156 ± 1	3 ± 1
PU_TC_nanoIR	2.08 ± 0.39	9.20 ± 1.67	62 ± 6	Pinned
PU_TC_laserIR	1.78	10.14	175	38

PU TC Ref	0.26 ± 0.06	1.39 ± 0.28	111 ± 1	35 ± 5
-----------	-----------------	-----------------	-------------	------------

The ice adhesion strength measured on the surfaces and coatings listed in Table 8 were on average higher than untreated substrate surfaces. To compare these to surfaces from other studies (Vercillo et al., 2020) done on titanium substrates, the ice adhesion strength data are plotted collectively in Figure 38. It includes the results from 272 ice adhesion strength measurements on 37 different surfaces. The horizontal axis categorizes the surfaces by substrate, either grade 5 titanium alloy, aluminum 2024 alloy, or stainless steel 304 alloy. The results are also separated by icing condition, rime, mixed/rime, mixed/glaze, and glaze detailed in Table 4. Each substrate had a reference, untreated or in other words, standard, surface with which to compare all other surfaces. The results from reference surfaces are in black concentric circles joined by a faint gray line. Values above the gray lines are interpreted here as an undesirable result because it means that ice adheres more strongly to those surfaces.

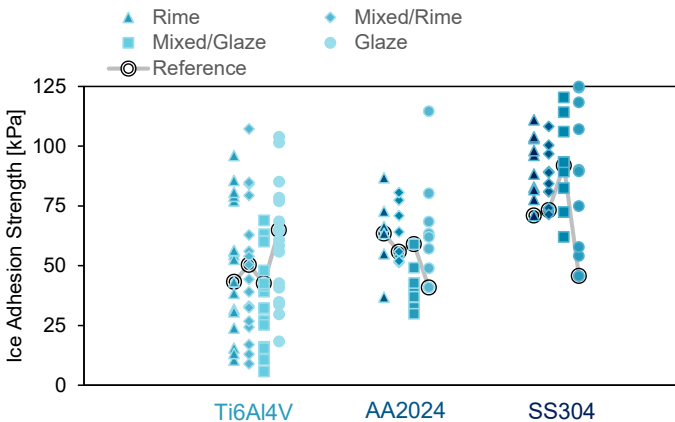


Figure 38: Ice adhesion strength of various superhydrophobic surfaces on either titanium alloy (Ti6Al4V), aluminum 2024 alloy (AA2024), or stainless-steel 304 alloy (SS304) substrates. Ice adhesion strength values measured on reference

surfaces are indicated by unfilled concentric circles joined by a line to guide the eye. Data under Ti6Al4V and some under AA2024 were extracted from (Vercillo et al., 2019, 2020).

A notable feature of the datapoints in Figure 38 is the disproportionate number of surfaces below the reference value of titanium compared to the aluminum and especially to stainless steel. Specifically, surfaces on titanium alloy substrates were the only ones to fall below 20 kPa ice adhesion strength, which has been selected, although somewhat arbitrarily, by some authors as the threshold for low ice adhesion strength (Kreder et al., 2016). Several questions arise about the exact cause of this unexpectedly favorable result for titanium. Namely, is it an effect of material properties? Or more directly, is it due to an assumption made in the ice adhesion strength model? The latter must be answered before the first, to verify the validity of the results. One must address the effect of ice thickness, substrate stiffness, ice stiffness, and other sources of uncertainty on the measurement of ice adhesion strength.

4.4 Influence of Ice Thickness on Ice Adhesion Strength Measurement

The deflection model for a bi-material cantilever under bending tells us that the maximum shear stress will occur at the interface when the neutral axis is at the interface of the two materials. The position of the neutral axis is dependent on the flexural stiffness of each material, and therefore on their modulus of elasticity and their thickness. On the ice adhesion strength test setup, each substrate with a different thickness or stiffness warrants a different ice thickness to ensure a neutral axis in proximity to the interface. The equation to determine the matching ice thickness is that to find the zeroes of neutral axis eccentricity:

$$h_{ice} = \sqrt{\frac{E_{substrate}}{E_{ice}}} h_{substrate} \quad (5)$$

The resulting ice thicknesses from this equation for the specific substrates used in this thesis are listed in Table 9. The extremes vary by a factor of two, meaning that the change in thickness is significant. One would expect that thicker ice would separate from the substrate at a lower stress state than thinner ice, since its bending stiffness is higher. Experimental observations from the previous section did not match these expectations. Ice on stainless steel, although thicker than on other substrates, required a larger interfacial shear stress to separate from the substrate surface.

4.4 Influence of Ice Thickness on Ice Adhesion Strength Measurement

Table 9: Nominal ice thickness grown on each substrate material.

Material	E_{sub} [GPa]	α_{sub} [10 ⁻⁶ /°C] ⁹	h_{sub} [mm]	E_{ice} [GPa]	h_{ice} [mm]
SS304	200	17	1.6	9	7.0
AA2024	73	21	1.6	9	4.5
Ti6Al4V	113	11	1.0	9	3.5

A series of experiments were performed varying the average ice thickness from 3 to 7.5 mm (Figure 39). An exponential decrease of strain at ice delamination with ice thickness was observed (Figure 39a). The data from Figure 39a was input into Equation (2) to compute the ice adhesion strength and plotted in Figure 39b. Here, the best fit line was linear instead of a power function, and the fit, R^2 , was 34% lower than on the strain data. A negative linear slope means that less deformation was needed to initiate an interfacial crack when the ice was thicker. Logically, a thicker beam produces higher stress at a given curvature than a thinner beam. The interfacial strength at fracture was expected not to vary with ice thickness, but it did slightly (Figure 39b). The fact that the fitted line was not flat meant that there are still some factors that have not been accounted for in the ice adhesion strength model. Despite that, the model helped to normalize the data to some extent by reducing the power function trend to a linear one.

⁹ Coefficient of thermal expansion. $\alpha_{ice} = 50 \times 10^{-6} / ^\circ\text{C}$

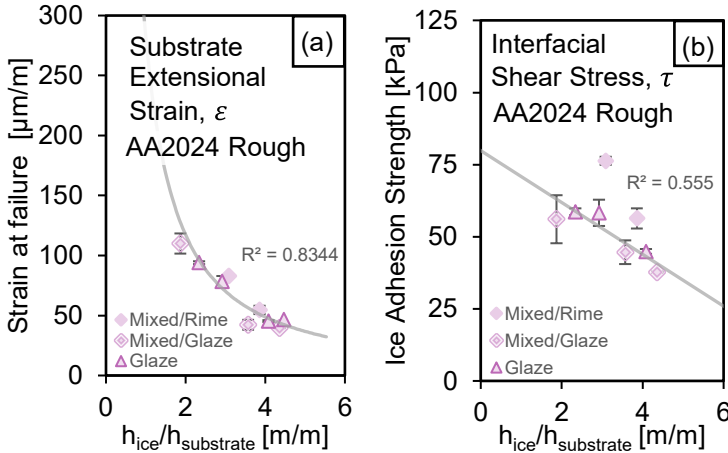


Figure 39: Ice adhesion strength for different ice thicknesses and ice types on aluminum.

The ice adhesion strength on different substrates shown in Figure 38, does not match the trend of Figure 39b, considering that the highest thickness ratio used was on stainless steel substrates, but its ice adhesion strength measured was the also the highest. The lowest ice adhesion strength was measured for titanium, where the thickness ratio was lowest. A possible cause for this discrepancy between substrate materials is the influence of thermal expansion on the measurement. As the ice thickness increases, so does the thermal stress in the system as the ice cools to the ambient temperature (either -20°C or -5°C). The increased stress at higher thicknesses could have contributed to the overall shear stress at the interface, meaning less applied stress was needed to cause delamination. Another perspective is that the stress concentration was more significant for thicker ice, resulting in a lower apparent shear stress.

The conclusion of this section is that the observed difference between ice adhesion strength values on reference surfaces is not primarily an effect of ice thickness, but rather of material properties. Evidence points to thermal properties as the dominant material properties:

4.4 Influence of Ice Thickness on Ice Adhesion Strength Measurement

coefficient of linear thermal expansion, thermal conductivity, or heat capacity. These properties influence the residual stress after ice has accreted, and the ice formation behaviour at the interface respectively. This explanation can also be used to compare differences in ice adhesion strength among different types of ice. Especially when the ice and the interface cool down to the ambient air temperature after freezing, which mostly took place close to 0°C, except for rime ice, where it can be assumed that all water freezes upon impact and the latent heat of crystallization is insufficient to increase the ice temperature to 0 °C. One would need to isolate whether bulk ice properties or the interfacial ice layer dominate the adhesion strength measurement with the cantilever setup. If bulk ice properties are a major influence on ice adhesion strength, then the substrate coefficient of linear thermal expansion is also of major influence, since it is the major difference between substrate materials which could lead to different residual interfacial stresses. If interface properties dominate, then the thermal diffusivity of the substrate is critical since it affects how droplets retract after impact and can affect the effective bonding area between ice and the surface. The next step is an uncertainty analysis of the ice adhesion test method, which will reveal the extent to which test parameters influence the measurement of ice adhesion strength using the vibrating cantilever method.

4.5 Uncertainty Analysis of the Ice Adhesion Test Method

An evaluation of the ice adhesion strength on 37 surfaces (Figure 38) revealed that titanium surfaces are more icephobic than stainless steel or aluminum. To keep the neutral axis of the iced beams close to the interface (see Figure 25), different ice thicknesses were used for each substrate material. The resulting nominal ice thicknesses were 4.5 mm for aluminum, 3.5 mm for titanium and 7.0 mm for stainless steel. Evidently, the average ice adhesion strength on each of these substrates increased with thickness of ice used. The question then arose: is the ice adhesion strength measurement influenced by ice thickness? The answer, shown in the preceding section, was that ice thickness influences the strain measured at the onset of ice delamination. However, after inputting that strain into the model (Equation (2)) the ice adhesion strength appeared to be independent of ice/substrate thickness ratio. Ice thickness is only one of the seven measurands used as input into Equation (2). Therefore, one should evaluate the influence of all seven parameters on the model. Instead of doing a costly set of swept parameter experiments an uncertainty analysis is used to reveal the sensitivity of the model to variations in each input parameter.

The analysis begins with an exploration of each of the model's parameters, beginning with the most controllable, the placement of the strain gauge. That is followed by the most easily measured parameters, being the thickness of the substrate and of the ice. Finally, an uncertainty model is built considering the contributions of individual parameters. The most critical parameters are identified and are explored further in the next chapter.

4.5.1 Uncertainty Model

Beginning with the mathematical formula for the calculation of interfacial shear stress, the compounded standard uncertainty of each parameter can be estimated. As illustrated in Figure 40, the

uncertainty of the strain gauge position, x , substrate length, l , strain, ε , ice and substrate thickness, h_{ice} and $h_{substrate}$ respectively, and ice Young's modulus, E_{ice} , contribute directly to the standard uncertainty of interfacial shear stress, τ . Young's modulus of the substrate, $E_{substrate}$, contributes indirectly, through the eccentricity, e .

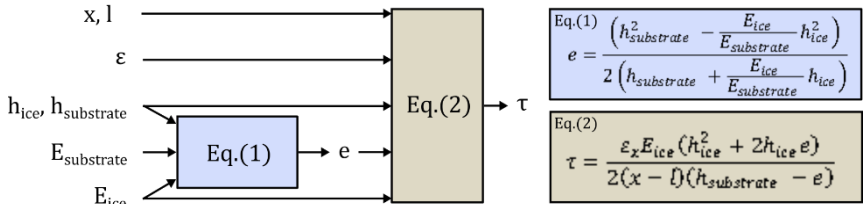


Figure 40: Uncertainty model showing direct or indirect influence of each parameter on interfacial shear stress.

The uncertainty of each parameter is estimated differently and is a combination of measurement limitations, controlled factors (x , L , h_{ice} , $h_{substrate}$, temperature, airspeed, and liquid water content) or uncontrolled environmental factors (humidity, and atmospheric pressure), and random effects. The following is a discussion detailing the estimation or exact calculation of the uncertainty of the parameters listed in the left-hand side of Figure 40, with the exception of Young's Modulus, E , which is taken from manufacturer specifications or from scientific literature. A summation of the individual uncertainties is thereafter provided, with the resulting model uncertainty.

The uncertainty analysis will be that of a single ice adhesion strength measurement data point. As a representative measurement, the third run of the mixed/rime condition on AA2024 Rough will be used. The approach used for the evaluation of standard uncertainty was that laid out by (Working Group 1 of the Joint Committee for Guides in Metrology, 2008)..The term “standard uncertainty” will be used per

the definition from the guide as “the uncertainty of a measurement expressed as a standard deviation.” For an experimentally observed pool of measurements, the standard uncertainty, $u(\chi_i)$, is the variance of that pool (squared standard deviation, $s(\chi_i)$) divided by the number of measurements in that pool (or the population, n).

$$u(\chi_i) = \frac{s(\chi_i)}{\sqrt{n}} \quad (6)$$

4.5.2 Standard Uncertainty of Strain

During vibration of an iced cantilever, the useful information given by the strain gauge is during delamination, shown in Figure 41. The placement of the strain gauge was on the ice-free face of the cantilever (explained in Section 3.3.2). The mean-line of the signal is non-zero as an effect of temperature variation; the signal was tared at 20°C. The five positive and negative peaks prior to a sudden spike in signal are averaged and used as input into Equation (2).

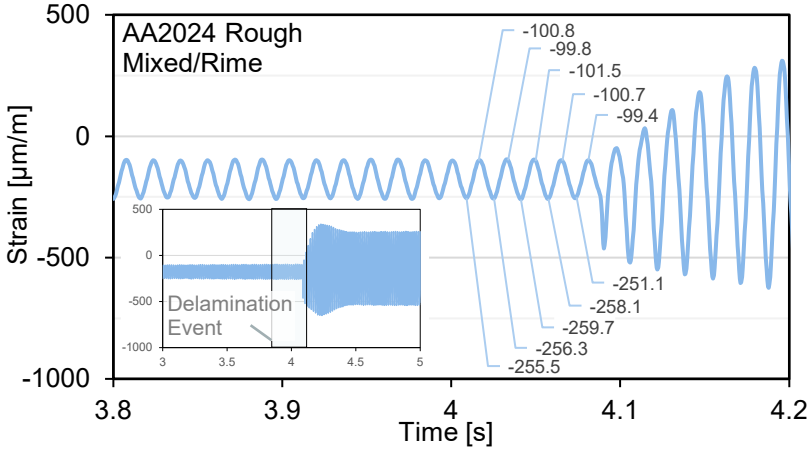


Figure 41: Strain signal measured during ice adhesion strength experiment with mixed/rime ice on AA2024 Rough. Inset shows larger time domain view with the delamination event identified. Data labels are the extracted data. Non-zero baseline due to thermal expansion effects of ice with substrate.

These ten points extracted from the strain signal are processed as follows.

$$\varepsilon_{center} = \frac{1}{N} \sum_{i=1}^N \frac{\varepsilon_i^- + \varepsilon_i^+}{2} \quad (7)$$

Where ε_{center} is the centerline of the sine wave computed as the average of the mean between the valley, ε_i^- , and the peak ε_i^+ , over N periods; in this work, $N = 5$. The strain used as input in the stress model is then computed as the average of the absolute difference between the peaks and center:

$$\varepsilon_{delamination} = \frac{1}{N} \sum_{i=1}^N |\varepsilon_i^+ - \varepsilon_{center}| \equiv \frac{1}{N} \sum_{i=1}^N |\varepsilon_i^- - \varepsilon_{center}| \quad (8)$$

The output of Equation (8) using data from Figure 41 are written in Table 10. These values were used as input in the evaluation of the combined standard uncertainty in Section 4.5.5. Here, the average strain amplitude was 78.9 $\mu\text{m/m}$, with a standard deviation of 2.10 $\mu\text{m/m}$ (3%). Since there were technically five data points, the standard uncertainty was obtained by dividing 2.10 $\mu\text{m/m}$ by $\sqrt{5}$, yielding 0.775 $\mu\text{m/m}$, or 1%. Such low uncertainty is owed to the mechanical simplicity of the vibrating cantilever system and the stability of the environmental conditions within which the measurements took place.

Table 10: Data used as input for strain variable in the uncertainty model.

$\varepsilon_{delamination}$	Standard Deviation, $s(\varepsilon)$	Standard Uncertainty, $u(\varepsilon)$
78.9 $\mu\text{m/m}$	2.10 $\mu\text{m/m}$	0.775 $\mu\text{m/m}$

4.5.3 Standard Uncertainty of Substrate Dimensions

Substrate length, width, and thickness are subject to typical manufacturing and machining tolerances. The length of the substrate, l , had the largest tolerance and has the smallest influence on the shear stress measurement. The width of the substrate is also not critical, since as long as it is relatively uniform, it is below a length-to-width ratio of 10. Thickness, $h_{substrate}$, is the most relevant substrate dimension, since small variations change the position of the neutral axis, leading to a strong error propagation. This uncertainty was minimized by using a stock sheet with a nominal thickness controlled by the supplier. Using a Vernier calliper (digital, Mitutoyo, Japan), the average thickness and length of AA2024 Rough were measured (Table 11).

Table 11: Measured values of substrate thickness and length and their standard uncertainty.

Input Variable, χ_i	Centre Value	Standard Deviation, $s(\chi_i)$	Standard Uncertainty, $u(\chi_i)$
$h_{substrate}$	1.625 mm	0.01 mm	0.01 mm
l	125 mm	0.19 mm	0.11 mm

The substrates were stable at room temperature, meaning the measurement of their dimensions and strain gauge position was uncomplicated. That cannot be said of ice grown on the substrate, which required an in-situ, contactless measurement technique, such as optical.

4.5.4 Standard Uncertainty of Ice Thickness

The thickness of thick spray coatings is often difficult to precisely control, at least more so than by adhesive bonding, chemical vapour deposition or physical vapour deposition. For ice grown by supercooled droplet spray, the precision intuitively decreases with the rate of deposition and solidification. In the iCORE icing wind tunnel, the uniformity of a coating of ice is controlled by varying the volume flow rate of water through each of three horizontally placed nozzles. The measurement of ice thickness is done through a calibrated top-view camera. In the camera viewer software, a line is placed to mark the nominal ice thickness. The image of the iced cantilever is later measured more precisely using an image analysis software, ImageJ. The measured contours of exemplary ice shapes are plotted in Figure 42.

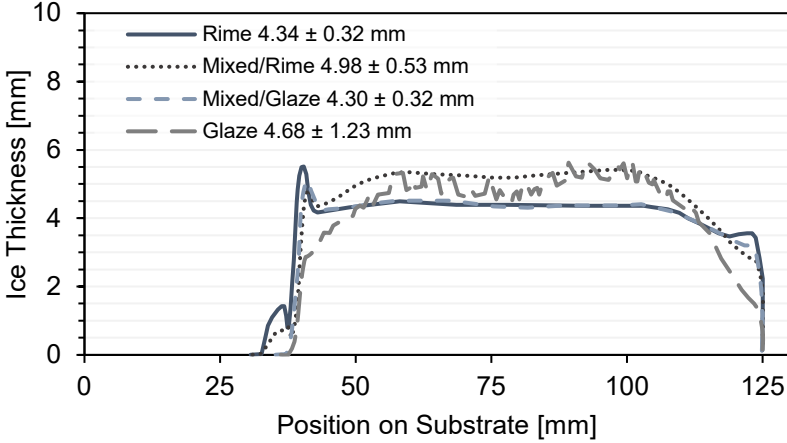


Figure 42: Ice thickness profile of four types of ice grown in the icing wind tunnel. Reported ice thickness for each profile provided in the legend.

The determination of the average thickness of ice can be expressed mathematically as in Equation (9). The boundaries a and b are approximate in their selection and are based on the most representative thicknesses. Here, a was chosen as the point where the thickness reached 75% of its maximum thickness, and b was chosen at 120 mm, 5 mm near the free end, and before the ice thickness began to decrease suddenly. Equation (10) and (11) were used to compute the average ice thickness and the standard deviation of the profile, respectively.

$$h_{ice,average} = \int_a^b h_{ice}(x) dx \quad (9)$$

$$h_{ice,average} = \frac{\sum_{i=a}^b 1/2 [h_{ice}(x_i) + h_{ice}(x_{i-1})][x_i - x_{i-1}]}{x_b - x_a} \quad (10)$$

$$h_{ice,St.Dev.} = \sqrt{\frac{\sum_{i=a}^b 1/2 [(h_{ice}(x_i) - h_{ice,average})^2 + (h_{ice}(x_{i-1}) - h_{ice,average})^2] [x_i - x_{i-1}]}{x_b - x_a}} \quad (11)$$

4.5.5 Evaluation of Combined Standard Uncertainty

In reality, each parameter comes with its own uncertainty based either on approximations, instrument precision, signal noise, or a combination of all. The uncertainties for each parameter are listed in Table 12. The combined standard uncertainty can be calculated by the sum of the squared product of the respective sensitivity coefficient and standard uncertainty of each parameter.

$$u_c^2(y) = \sum_{i=1}^N [c_i u(\chi_i)]^2 \quad (12)$$

The sensitivity coefficient of an input variable is defined as the change in the output value, $Y = f(\chi_1, \dots, \chi_i, \dots, \chi_N)$, for a unit change in the respective variable.

$$c_i \equiv \frac{\partial f}{\partial \chi_i} \quad (13)$$

The combined standard uncertainty can be solved numerically by replacing $c_i u(\chi_i)$ with Z_i , where:

$$Z_i = \frac{1}{2} \{f[\chi_1, \dots, \chi_i + u(\chi_i), \dots, \chi_N] - f[\chi_1, \dots, \chi_i - u(\chi_i), \dots, \chi_N]\} \quad (14)$$

The combined standard variance then becomes:

$$u_c^2(y) = \sum_{i=1}^N Z_i^2 \quad (15)$$

As an indication of relative sensitivity of the input variables, their respective contribution to the combined standard variance can be calculated and compared.

$$\text{Contribution to Combined Variance} = \frac{Z_i^2}{u_c^2(y)} \quad (16)$$

Finally, the expanded uncertainty can be calculated by multiplying the combined standard uncertainty by a coverage factor. A coverage factor of 2 corresponds to a confidence of 95% that the value lies within the expanded uncertainty (Working Group 1 of the Joint Committee for Guides in Metrology, 2008). A summary of the calculation of the combined standard uncertainty of ice adhesion strength can be found in Table 12. The eccentricity, e , and interfacial shear stress, τ , are calculated based on the centre-values listed as “value.” The combined standard uncertainty of both results is expressed as the expanded uncertainty with a coverage factor of 2 (95% confidence). The most influential input variables are h_{ice} at 29% and E_{ice} at 65%. A reduction in the standard uncertainty of E_{ice} would therefore play the largest role in reducing the overall uncertainty of τ .

4.5 Uncertainty Analysis of the Ice Adhesion Test Method

Table 12: Standard uncertainties of parameters used for the calculation of interfacial shear stress. Values are determined based on measurements with AA2024 Rough in the mixed/rime condition.

Name	Value	$u(\chi_i)$	Z_i [kPa]	c_i [kPa/_]	Contribution
h_{ice}	4.98 mm	0.53 mm	4.60	8.68 mm	29%
$h_{substrate}$	1.625 mm	0.01 mm	0.11	11.40 mm	0.02 %
ε	79 $\mu\text{m}/\text{m}$	0.8 $\mu\text{m}/\text{m}$	0.61	0.78 μm	1 %
l	125 mm	1.1 mm	-0.77	-0.77 mm	1 %
x	45 mm	0.5 mm	0.77	0.77 mm	1 %
$E_{substrate}$	73 GPa	3 GPa	1.67	0.56 GPa	4 %
E_{ice}	9 GPa	2.8 GPa	6.87	2.45 GPa	65 %
e	-90 μm	500 μm	-	-	-
τ	62 kPa	17 kPa	-	-	-

The Young's Modulus of ice is expected to vary depending on the density and grain size of ice, mainly stemming from the conditions in which ice was grown. Since such a wide range of values has been reported in literature, it would be advantageous to be able to measure a calibrated value of E_{ice} for ice produced by our icing wind tunnel in the conditions of Table 4. A method for doing so is presented in the next chapter.

4.6 Determining the Young's Modulus of Ice Using the Ice Adhesion Test Setup¹⁰

The Young's Modulus of materials must be known for the determination of the adhesion failure in a bi-material system. In the vibrating cantilever ice adhesion test the elastic modulus of the ice grown on the substrate is taken from literature. However, values from literature vary by more than 50% (M. Pervier, 2012). A method for the determination of an unknown E of a coating has been reported for thermal spray coatings (Rybicki et al., 1995). In the present study, a new indirect method is reported for coatings of non-uniform thickness. The method is demonstrated on four types of ice grown by impacting supercooled water microdroplets.

The measurement was done using four nominal ice thicknesses (3, 4.5, 6, and 7 mm) and plotted in Figure 43. Deflection measurements were done while the beam was in its first mode of forced vibration, meaning that the measurements averaged tensile and compressive normal stresses in the ice. The modulus was more consistent at higher thicknesses. Since fundamentally, E does not vary with thickness, values with the lowest thickness were discarded because it seems that their characterization is affected by limitations of the test method. For larger ice thicknesses (above 4 mm), on the other hand, the method provides robust and reproducible results. (Waki et al., 2014) reported a similar trend of larger error in Young's modulus measurement with decreasing coating thickness for their thermal spray coatings using four different measurement methods. In comparing measurement methods, they recommended the use of

¹⁰ The contents of this section have been published in (Laroche et al., 2021).

those with less error at small coating thicknesses but did not rationalize the presence of the error.

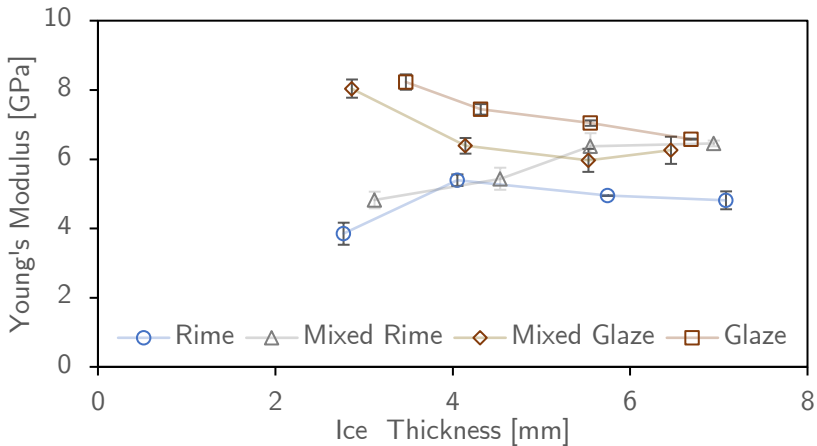


Figure 43: Young's Modulus variation with ice thickness for four ice types measured with the vibrating cantilever test setup.

The average Young's Modulus for each ice type defined by conditions listed in Table 4 is plotted in Figure 44. The values ranged between 5 and 7 GPa, nearly half of that reported in (Gammon et al., 1983; M. Pervier, 2012). The random uncertainty of the values was between 1-5%, representing one standard deviation.

If liquid water content (LWC) was an important factor in the E of accreted ice, then it can be seen by comparing that of rime (LWC = 0.3 g/m^3) and mixed/rime (LWC = 0.8 g/m^3), since the temperature and airspeed were the same in both these conditions. At lower droplet impact rates, the droplets were more likely to stack in a columnar fashion, without remelting. For higher droplet impact rates, it was more likely for intercolumnar joints to appear due to

remelting of already frozen droplets from newly impacting droplets. The result was an overall increase in E .

A similar explanation can be given for the difference between rime and mixed/glaze. Here the impact velocity and droplet impingement rate were the same, but the ambient temperatures were different. At the warmer temperature, in mixed/glaze, droplet freezing time was increased, granting them some mobility before solidifying, likely creating the same intercolumnar bridges as in mixed/rime ice.

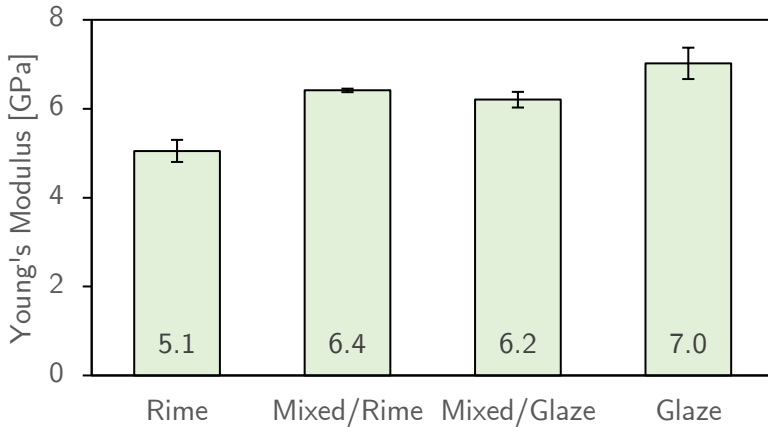


Figure 44: Young's Modulus of ice types averaged over three ice thicknesses.

Glaze ice had the highest E , but also the lowest porosity, therefore fewest defects, and typically the strongest adhesion. The other ice types were characterized by higher porosities, leading to more structural defects and to smaller Young's moduli. The modulus seemed to be a function of homogeneity and perhaps isotropy of the ice. The most columnar and porous ice formed with the lowest liquid water content and at the lowest temperature had the lowest elastic modulus. Increasing the liquid water content produced columns with many interconnections, thereby increasing the modulus. When the

low liquid water content was used, but at much higher temperature, it produced much denser ice with a higher modulus. Finally, for glaze ice, the modulus was the highest, and close to that measured by growing ice in a freezer.

When the measured elastic moduli are used for calculating the critical average interfacial shear stress on the reference aluminum surface, the result looks like those presented in Figure 45. Generally, the ice adhesion strength was lower than for the 9 GPa elastic modulus. The values for rime, mixed/rime, and mixed/glaze were all roughly the same. The relative value of glaze ice adhesion strength changed by only 3 kPa (7.5%).

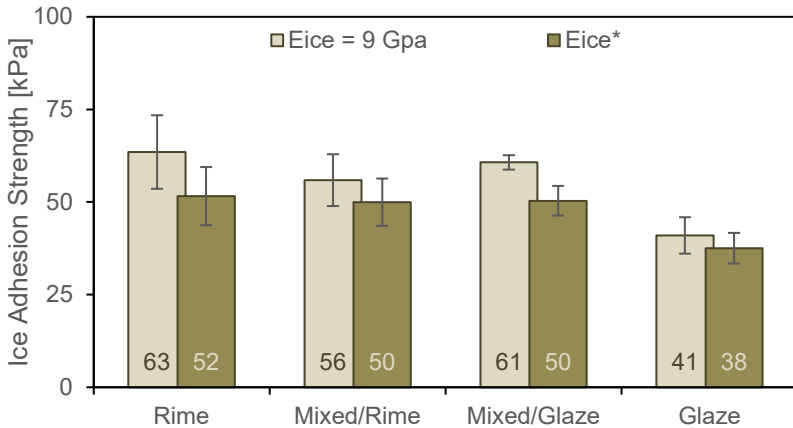


Figure 45: Ice adhesion strength on AA2024 Ref calculated from strain measurements with a vibrating cantilever using a constant elastic modulus, $E_{ice} = 9 \text{ GPa}$ from literature (light columns), or the measured elastic modulus, E_{ice}^* , different for each type of ice.

Using measured values of the elastic modulus of ice can help to improve the uniformity of ice adhesion strength across icing conditions. Figure 45 shows that glaze ice was the only condition

with ice adhesion strength different from the others. E_{ice} did not vary considerably between ice types (<35%) and therefore does not explain the large differences seen between rime and glaze ice adhesion strength. Glaze ice was the only condition tested here with an airspeed of 80 m/s. Droplet impact speed and, hence, droplet spreading must therefore be a dominant parameter to determine the adhesion strength of ice to this surface.

The uncertainties inherent to the ice adhesion measurement method have been addressed and explained, revealing the most critical parameters. Where possible, the uncertainties have been reduced through additional measurements. It can be concluded that differences in measured ice adhesion strength in Figure 38 of Section 4.3 were due to material properties of the substrates and their surfaces rather than the properties of the ice itself. The ice thickness and mechanical properties appear to only play minor roles in the identification of low ice-adhesion surfaces. With this improved model for determining ice adhesion strength, focus can be placed on different substrate surface parameters, such as surface roughness.

4.7 Influence of Surface Roughness on Ice Adhesion Strength

Superhydrophobic surfaces owe their exceptional water-repellent ability to their micro- and nano-topology in addition to low surface free energy. From reports of numerous ice adhesion studies, superhydrophobicity does not always carry over into low ice adhesion strength (Maitra et al., 2015). The results of Section 4.3 above agree with that observation. What is then the exact dependence of ice adhesion strength on surface topology? Are the shortcomings of microstructures mended by the presence of nanostructures?

The influence of surface roughness on the adhesion strength of ice has been the focus of many studies over the past 70 years or more. The general consensus is that a higher roughness leads to higher ice adhesion strength. The reasoning for that collective observation has most often been that ice mechanically binds to surface asperities. The trend becomes complicated by factors such as morphology of surface asperities, their periodicity, uniformity, and scale – to name a few. Surface topology can be engineered such to achieve a robust Cassie-Baxter wetting state, in which water droplets have a reduced contact with a solid surface. The shape of such topology can backfire if droplets transition from a Cassie-Baxter wetting state to a Wenzel wetting state because the effective contact area would be higher than on a flat surface. Several environmental factors can lead to such a transition, in particular, droplet size and impact speed, as discussed in Section 4.3.

Several studies have been published showing the relation between surface roughness and ice adhesion strength (Balordi et al., 2019; M. L. A. Pervier et al., 2019; T. Strobl et al., 2012; Vercillo et al., 2020). The exact relation depends grossly on icing conditions, substrate material, and ice adhesion measurement methods. Here, the trend of ice adhesion strength with arithmetic mean surface roughness

(Rz) and maximum profile height (Rz) are presented. Ice adhesion strength was measured in the iCORE icing wind tunnel using a vibrating cantilever ice adhesion measurement system. Two substrate materials are shown in Table 13 and Table 14. Table 13 is a list of stainless-steel substrates and shows surface roughness and wetting properties of a reference, as-received surface, and two laser treatments. The line-peaks of the patterns ran parallel to the length of the cantilever in the ice adhesion test. The patterned surfaces can be considered hydrophobic due to their water contact angles above 90°. The roll-off-angle of 90° indicates that droplets were pinned to the surface.

Table 13: List of roughness and wetting properties for stainless steel surfaces tested.

Name	Ra [μm]	Rz [μm]	CA [°]	RoA [°]
SS_ref	0.170 ± 0.012	1.632 ± 0.154	70 ± 5	Pinned
SS_nsIR	2.328 ± 0.081	13.466 ± 1.491	114 ± 12	Pinned
SS_psUVs	0.926 ± 0.044	9.969 ± 0.332	123 ± 4	Pinned

Table 14 lists a series of grade 5 titanium (Ti6Al4V) surfaces. Two reference surfaces are included: an as-received surface with its native oxide layer, and nanotube-shaped, anodic oxide layer on an unpolished surface. The laser induced periodic surface structures (LIPSS) consist of long peaks that run parallel to the length of the cantilever. The ROUGH surfaces consist of sharp peaks microscopic, periodic in two dimensions. All the titanium surfaces listed were dip-coated in a perfluoropolyether compound, except for the as-received surface. The combination of patterning and modified surface chemistry gave them superhydrophobic properties at room temperature.

4.7 Influence of Surface Roughness on Ice Adhesion Strength

Table 14: List of roughness and wetting properties for titanium surfaces tested. Data for Ti_LIPSS1, Ti_LIPSS2, Ti_ROUGH1, and Ti_ROUGH2 from (Vercillo et al., 2019).

Name	Ra [μm]	Rz [μm]	CA [$^\circ$]	RoA [$^\circ$]
Ti6Al4V Ref	0.50 ± 0.03	3.97 ± 0.17	51 ± 2	Pinned
Ti6Al4V nTiO2 PFPE	0.58 ± 0.03	4.40 ± 0.17	166 ± 1	15 ± 6
Ti_LIPSS1	0.45 ± 0.01	3.41 ± 0.21	169 ± 3	9 ± 4
Ti_LIPSS2	0.47 ± 0.01	3.75 ± 0.28	163 ± 3	8 ± 7
Ti_ROUGH1	2.43 ± 0.05	14.40 ± 0.08	168 ± 2	2 ± 2
Ti_ROUGH2	3.28 ± 0.06	19.47 ± 0.25	169 ± 2	4 ± 3

The average and standard deviation of their ice adhesion strength for all conditions and repetitions are plotted in Figure 46. Stainless steel typically shows higher ice adhesion strength than titanium for reasons previously discussed. The slopes of the trendlines in Figure 46a and Figure 46b are similar for stainless steel and for titanium, suggesting a universal relation with surface roughness and maximum profile height. The superior fit for the stainless-steel data group is because only three data points are available. The deviation from the trendline for titanium testifies to the influence of chemistry and type of surface features. The higher-roughness surfaces fall in very close proximity to the trendline, suggesting that surface roughness can play a dominant role when the range of comparison is high enough.

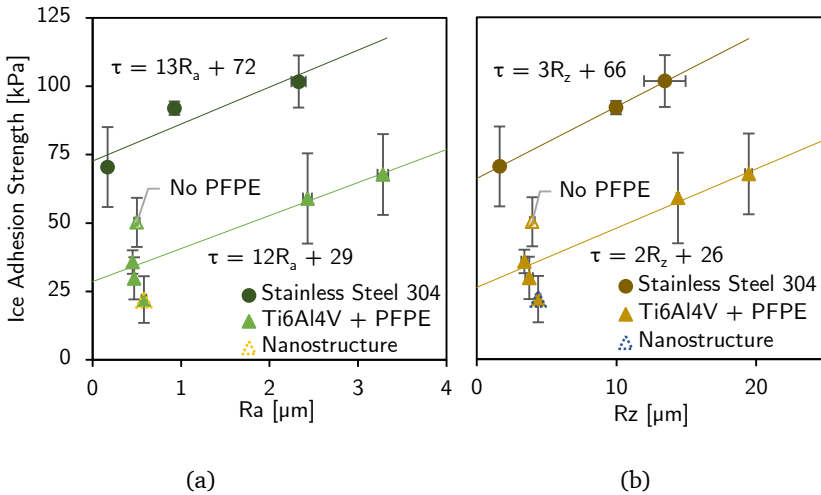


Figure 46: Influence of surface roughness on ice adhesion strength for stainless steel 304 alloy and Ti6Al4V. The results of a single group of surfaces was split into two charts where (a) are plotted on average roughness, Ra, and (b) are plotted on average peak-to-trough roughness, Rz. τ symbolizes maximum interfacial shear strength. Dark circles represent stainless steel surfaces, and lighter triangles represent titanium surfaces. Adapted from (Vercillo et al., 2019).

Ice adhesion strength and surface roughness are strongly correlated, independently of material properties and ice thickness. Stylus profilometry is limited by the stylus radius, and therefore does not capture the presence of nanoscopic surface features very well. The cluster of data points for titanium at low roughness represents the existence of nanotopology of varying prominence. The lowest ice adhesion strengths were obtained with the most prominent (intentional) nanotopology.

(Vercillo et al., 2020) showed that with proper tuning of surface structures, low ice adhesion strength on titanium surfaces is achievable, when the surface chemistry provides low surface free energy. Those surfaces are represented in Figure 46 as the lowest ice

adhesion strengths obtained for titanium. He also showed that structures on the softer of the hard materials (aluminum alloy as the softer, compared to titanium alloy) could be modified or damaged just by ice adhesion testing (Vercillo et al., 2019).

Structured superhydrophobic surfaces rely on air pockets between pillars or within porous structures to ensure that a liquid droplet remains in a Cassie-Baxter wetting state. Air, being a gas, is compressible and fluid, and can therefore be displaced with the right conditions. The concept of water hammer pressure has been used to explain why an impacting water droplet may penetrate these pores and cause a partial or total wetting state. If a droplet takes on a total wetting state on a structured surface, its adhesion to that surface becomes greater than if the surface were flat.

The hard surfaces that were determined to have low adhesion to ice were all coated with a perfluoropolyether compound. The lowest ice adhesion strengths were conclusively due to the hierarchical structures on the surface, but without the fluorinated compound, the structures would not have been so effective. After exposure to UV, this compound tends to break down. Since aircraft are regularly exposed to high dosages of UV radiation, it does not seem logical to use such a chemistry industrially. A non-organic surface chemistry that exhibits the same or better low ice adhesion performance is therefore highly sought-after. If such a compound can be applied to a hard structured surface, then it would meet certain aircraft surface durability requirements.

Decreasing micro-scale surface roughness appears to decrease ice adhesion strength in dynamic bending. The presence of nano-scale features on a surface further decreases ice adhesion strength but is difficult to measure by stylus profilometry. The low surface energy given by the perfluoropolyether coating on titanium led to the lowest ice adhesion strength reported by this method. It is however known that such a coating on titanium dioxide will deteriorate in the

presence of certain bands of UV. Can some alternative coatings be proposed which will provide or maintain a nanostructure while remaining stable after exposure to UV light?

4.8 Durability of a Silicone Nanofilament Coating (SNF) on Textiles in Icing Conditions¹¹

In previous chapters, it has been shown that ice adhesion strength on a superhydrophobic surface is lowest when a nano-scale topology is present in combination with a low surface free energy. The most effective combination happens to be on titanium. The caveat is that low surface free energy compounds on titania destabilize after exposure to UV. Silicone is a material with intrinsically low surface free energy, it is chemically inert, and does not react to UV exposure. Recent advances have made it possible to grow silicone as a nanofilament network in a controlled, repeatable, and up-scalable method. Some abrasion tests have shown that a silicone nanofilament network is likely to be damaged when grown on a hard flat surface (Zimmermann, Reifler, et al., 2008). On the other hand, when grown on a flexible micro-textured surface such as a textile, a silicone nanofilament coating has been shown to be considerably durable. Attached to various exterior automobile components, a silicone nanofilament-coated polyester textile remained mostly hydrophobic even after ~250 days in four-season weather (Geyer et al., 2020).

Fabric aircraft skins have been historically important in aviation. A fabric taught over rigid wing spars provides a smooth aerodynamic surface with minimal weight, ideal for small and ultralight aircraft. Due to its low cost and light weight, this concept is still being used to this day on some small aircraft. Although more robust light aircraft are built using carbon fiber composites, many recent home-built or

¹¹ The contents of this chapter have been published in (Laroche, Ritzen, et al., 2020).

experimental aircraft make use of fabric-covered wings (FAA, 2012). These small aircraft typically fly at airspeeds not exceeding 80 m/s or 300 km/h (EASA, 2011; Maule Aerospace Technology Inc., 2016). If a superamphiphobic¹² silicone nanofilament (SNF) coating grown on a polyester fabric is stable enough to endure conditions resembling those of small aircraft, then they are potentially relevant for commercial use.

The wetting properties of superamphiphobic fabrics measured following exposure to a warm cloud of droplets at airspeeds up to 120 m/s on a NACA 0012 profile are plotted in Figure 47a. The water contact angle remained constant within experimental accuracy after exposure to clouds at speeds between 20–100 m/s. At the highest airspeed, 120 m/s, the contact angle on the suction side (S1, S2) and leading-edge region (LE) decreased sharply to 130° whereas the pressure side (P1, P2) continued the flat trend to 160°. Within experimental accuracy, the water roll-off angle was almost constant until exposure to clouds at 100 m/s, after which complete pinning (plotted as 90°) was observed. The roll-off angle slightly increased after exposure to 100 m/s. The sudden decrease in contact angle and increase in roll-of angle indicate damage to the coating on the fabric, mainly on the suction side and the leading-edge region of the airfoil. Further evidence of this damage is given by the top SEM image of Figure 47c. The coating was finally damaged after exposure to 120 m/s but for a cumulative duration of 50 min, since a single piece of fabric was used for testing the progressive airspeed exposure.

¹² Superamphiphobic: repels both polar and non-polar liquids.

4.8 Durability of a Silicone Nanofilament Coating (SNF) on Textiles in Icing Conditions

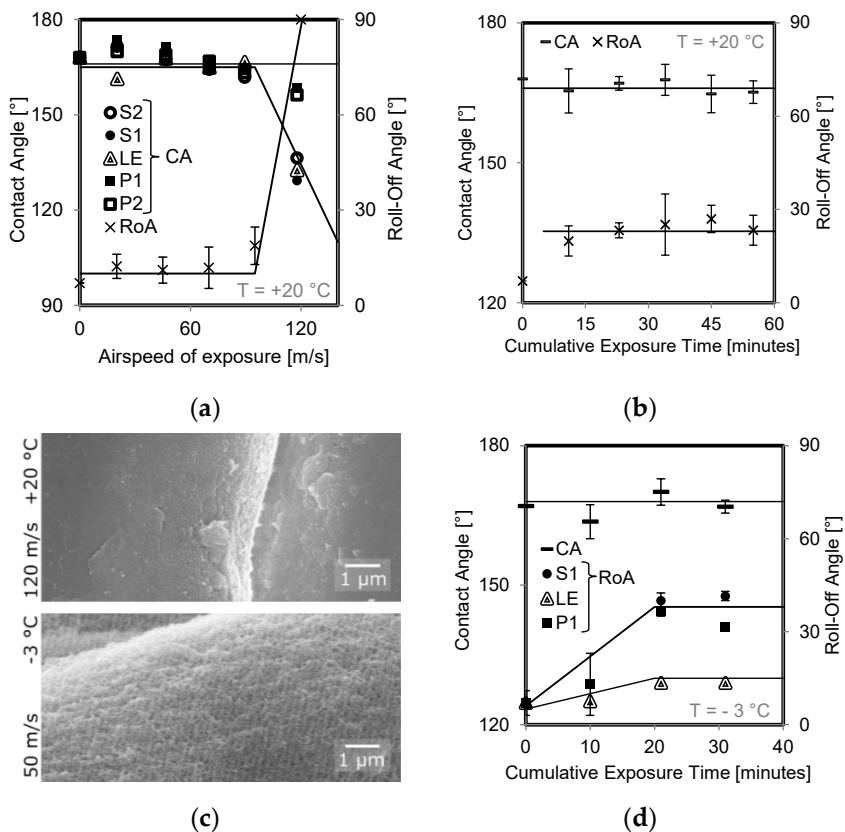


Figure 47: Wetting properties of the superamphiphobic fabric exposed to aerodynamic wear conditions. Pressure side “P2” (hollow square), pressure side “P1” (filled square), stagnation line “LE” (concentric triangles), suction side “S1” (filled circle), suction side “S2” (hollow circle) positions, equilibrium contact angle averaged over all positions (flat bar), and roll-off angle averaged over all positions (cross). (a) After exposure to a warm droplet cloud at speeds from 20 to 120 m/s, for a cumulative duration of 50 min. (b) After exposure to a warm droplet cloud at 90 m/s for up to 50 min. (c) SEM images of polyester fibers on fabrics exposed to 120 m/s (top) and 50 m/s for 3 icing cycles (bottom). (d) After exposure to 3 icing cycles at 50 m/s. Lines are shown as a guide for the eye. Reprinted from (Laroche, Ritzen, et al., 2020) under the Creative Commons License, CC BY 4.0.

The angle of attack of the airfoil was meant to be at 0° (Figure 31a), however, contact angle measurements presented in Figure 47a suggest that tests were done at a non-zero angle of attack. The pressure-side boundary layer and suction-side boundary layer create different wall friction stresses. Direct numerical flow simulations (DNS) of a NACA 0012 profile at an angle of attack of 5° and Reynolds number, $Re = 5 \times 10^4$, showed that the coefficient of pressure along the airfoil suction side is higher in magnitude near the leading edge than that on the pressure side (Balakumar, 2017) (Reynolds number (Re) is the ratio between inertial forces and viscous forces of a fluid in motion). Wall friction shear forces are dependent on the flow velocity, and since the flow was faster over the suction side, the wall shear stresses were higher. The more intense of the stresses was evidently on the suction side, where flow separation is likely to occur. It is expected that the pressure difference between the bottom and the top of the airfoil was due to a small angle of attack tolerance during installation of the profile in the test section, and due to manufacturing tolerances, which led to a slightly shorter bottom side. These small geometric deviations were amplified by the high Reynolds number at 120 m/s ($Re = 1.6 \times 10^6$), which forced the airfoil to pitch upwards slightly. The only resistance to this pitching was contact friction with the test section walls, governed by the hand-tightness of the screws used to fasten the airfoil along a single axis. A small angle of attack at such high Reynolds numbers can lead to wall shear stress differences over the top and bottom surfaces (8 Pa difference), and flow instabilities (McDevitt & Okuno, 1985), especially in a straight, fixed-size test section. According to (Balakumar, 2017), the skin friction coefficient along the airfoil peaks near the leading edge and decreases rapidly toward the trailing edge.

To isolate the duration of exposure from airspeed, separate tests were done at a constant speed but increasing exposure time (Figure 47b). An airspeed of 95 m/s was used since it was suspected that the same damage seen at 120 m/s could be observed at a lower speed,

but with longer exposure time. Contact angle measurements exceeded 160° ($165^\circ \pm 3^\circ$) for the full 50 minutes showing no measurable change with increasing exposure time. Roll-off angle measurements slightly increased after the first 10 minutes of exposure, and then remained constant at $22^\circ \pm 5^\circ$. This indicates that the full damage occurred within the first 10 minutes of testing and did not increase with increasing exposure time. This result suggests that SNF were removed or broken when wall shear stresses (roughly 6 kPa for an airflow at 120 m/s) exceeded their tensile strength. The absence of time-dependent damage suggests that they did not show signs of creep for the durations tested. Cloud exposures were in 10-minute intervals, and the SNF had time to resettle between exposure sessions. The main knowledge gained here is that maximum damage at a certain airspeed occurred within the first 10 minutes of exposure and that the coating was removed only beyond a critical shear stress threshold—independently of exposure time.

The damage done to the silicone nanofilament coating following exposure to harsh aerodynamic conditions while covering a NACA 0012 profile is shown by SEM images in Figure 47c. The top image is that of the fabric after 120 m/s cloud exposure. It shows two smooth PET fiber surfaces with well-defined boundaries. The smoothness of the fibre is evidence that the coating was removed from the top and sides of the polyester fibers. During water droplet roll-off angle measurements, these damaged areas acted as pinning sites. The bottom image is that of another sample that was tested in icing conditions. It appears to have a porous surface with filamentous features sizing an order of magnitude less than the scale bar of $1 \mu\text{m}$. These features prove that at least the base silicone coating and roots of nanofilaments remained attached to the surface.

The airfoil-mounted textile was exposed to icing conditions at -3°C at an airspeed of 50 m/s. After every 10 minutes of exposure, the textile was removed from the icing conditions for contact angle and

roll-off-angle measurements using water (Figure 47d). The water contact angle remained in excess of 160° for the full 40 min of icing exposure. However, the water roll-off angle of the pressure (P1, P2) and suction side (S1, S2) increased steadily to 40° after 20 min of exposure after which it remained constant, whereas the leading-edge region (LE) roll-off angle increased steadily to 15° after which it remained constant. This increase in RoA is an indication of damage to the coating, and the extent of damage increases with increasing RoA.

Therefore, ice accretion caused damage to areas subjected to aerodynamic shear, but not on the leading-edge area. The ice grains that formed on the leading edge were densely packed, forming a solid block of ice that protected a small area of the fabric from airflow and direct impact of droplets (pathline illustration in Figure 31b and experiment image in Figure 31c). A few millimeters downstream along the chord-length, ice grains were more dispersed. Boundary layer air could flow between ice grains, pulling them away from their anchor-point on the fabric. This pulling was most probably the main wear mechanism causing damage to the SNF coating (explained in greater detail below). Since the angle of attack of the airfoil was null, the wear on the suction and pressure side were observably equal in icing. For the icing conditions tested, the peak skin friction stress would be on the order of 10 Pa and located at 0.027 mm from the leading edge (based on data from (Abbott & Von Doenhoff, 1959)).

To summarize, the coating retained its superhydrophobic properties until a speed of 120 m/s, or after exposure to 10 consecutive minutes of icing in a turbulent airflow. Notably, exposure to icing conditions in which the textile was completely covered in ice actually protected the coating from impacting ice crystals or tearing of ice grains. Superhydrophobicity is typically an indicator of icephobicity, especially when a nanoscale roughness is present. Water CA and RoA tests are indicators of whether a microscale roughness has been

damaged, but only repeated ice adhesion strength tests will reveal whether the functional nanoscale roughness is mechanically durable.

A silicone nanofilament coating on a textile was stable in simulated icing conditions except in conditions far more aggressive than what is typically seen in an ice adhesion test. If they can be successfully grown on a metallic substrate, are mechanically durable enough for the ice adhesion test, and result in low ice adhesion strength, then the coating may be a viable alternative to UV-susceptible perfluoropolyether.

4.9 Ice Adhesion and Durability of Silicone Nanofilament Coatings on Aircraft Alloys¹³

Low ice adhesion strength on a surface can be obtained by decreasing the surface free energy, and by giving the surface a favorable topology (Meuler, McKinley, et al., 2010). A combination of microstructure and nanostructure yielded the most promising results for laser-patterned titanium coated with a perfluoropolyether (Vercillo et al., 2020). However, the transparency of the coating combined with the photoactivity of titanium dioxide makes such a coating unstable after exposure to UV-light (Diebold, 2003). Silicone is an inert compound, making it inherently chemical-resistant (Zimmermann, Artus, et al., 2007), as well as UV-exposure resistant. In bulk, it can be eroded and abraded rather easily, but at the molecular scale, it has potentially high resistance to erosion. Silicone nanofilaments are a promising alternative to perfluoropolyether since they also have low surface free energy, a nanostructure, and since they are composed of silicone, are resistant to UV (G. R. J. J. Artus et al., 2006).

Until recently, silicone nanofilament networks grown on surfaces have only been presented as superhydrophobic, rather than icephobic. Their applications mainly related to water and oil repellency (G. R. J. J. Artus et al., 2006), or CO₂ capture (Geyer et al., 2017). Their successful durability on micro-structured substrates such as textiles (Geyer et al., 2020) proved that they can be durable enough for year-round outdoor applications. The exposure conditions on textiles were pushed further in a controlled environment at high speed and in the presence of atmospheric icing

¹³ The contents of this section have been published in (Laroche et al., 2021).

conditions (Laroche, Ritzen, et al., 2020), as described in Section 4.8. Since they appear to be durable enough for icing conditions, the question still stands of whether they are effective as an icephobic coating, and if so, are they suitable for growth on surfaces relevant in aerospace.

Here silicone nanofilaments were grown on aircraft-relevant metal alloys: aluminum 2024, and Ti6Al4V. The coated substrates were put through at least 16 cycles of icing and de-icing in the in-situ ice adhesion test apparatus. Following the testing sequence, their water droplet contact angle and roll-off-angle were measured after each icing cycle to gauge their effective durability.

Aluminum alloy corrodes in an HCl environment, and therefore the silicone nanofilament growth procedure needed to be adjusted to minimize the amount of HCl generated during the reaction (see detailed procedure in Section 3.1.3.2). For the titanium alloy, it was first anodized such that a layer of TiO₂ nanotubes was present. Once a silicone nanofilament network was grown onto the metal alloys, they were superhydrophobic. A further step on some substrates was fluorination – a process in which oleophobic fluorine groups are chemically bonded to the nanofilaments. This step improved their hydrophobicity as evidenced by their increased water contact angle and decreased sliding angle listed in Table 15.

Table 15: Wettability and roughness characteristics of the SNF surfaces tested for ice adhesion strength. Fluorinated coatings are denoted “fSNF”. ^{a)}Contact angle and roll-off angle was not measurable since droplets were too mobile; ^{b)}Roughness profile is assumed to be the same as T4; ^{c)}Roughness profile is assumed to be the same as A3.

Name	Ra [μm]	Rz [μm]	CA [$^\circ$]	RoA [$^\circ$]
Ti6Al4V Ref	0.50 ± 0.03	3.97 ± 0.17	51 ± 1	Pinned
Ti6Al4V nTiO2 PFPE	0.58 ± 0.03	4.40 ± 0.17	166 ± 1	15 ± 6
Ti6Al4V SNF	- ^{b)}	- ^{b)}	167 ± 1	2 ± 1
Ti6Al4V fSNF	0.48 ± 0.03	3.90 ± 0.26	- ^{a)}	- ^{a)}
Ti6Al4V LubSNF	- ^{b)}	- ^{b)}	112 ± 0	9 ± 2
AA2024 Ref	0.01 ± 0.01	0.16 ± 0.02	59 ± 1	Pinned
AA2024 PFPE	0.02 ± 0.01	0.15 ± 0.04	122 ± 3	Pinned
AA2024 SNF	0.29 ± 0.00	5.58 ± 0.74	166 ± 1	13 ± 8
AA2024 fSNF	- ^{c)}	- ^{c)}	166 ± 1	5 ± 3

4.9.1 Dry Silicone Nanofilament Coatings on Aluminum

The ice adhesion strength measured on aluminum uncoated (AA2024 Ref), perfluoropolyether-coated (AA2024 PFPE), SNF-coated (AA2024 SNF), and fluorinated SNF-coated (AA2024 fSNF) are plotted in Figure 48. The slight improvement between AA2024 Ref and AA2024 PFPE was discussed in Section 4.3 above. Globally, for all icing conditions, AA2024 SNF and fSNF showed lower adhesion to ice than Ref and PFPE. The low adhesion to ice was enhanced with fluorinated SNF.

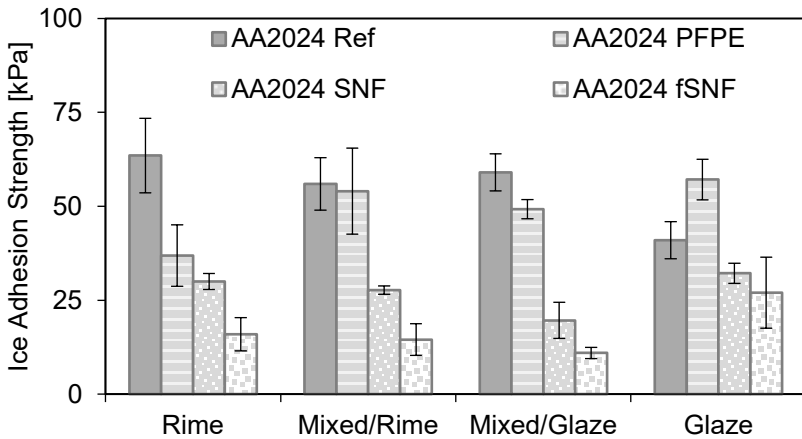


Figure 48: Ice adhesion strength on anodized aluminum with silicone nanofilaments, with and without fluorination.

The small uncertainty bars reveal that the measurements were repeatable for at least 4 repetitions under each condition, and for at least 16 icing/de-icing cycles overall. In other words, the surfaces were durable enough to retain their low ice-adhesion performance for that many cycles. During ice delamination, using the vibrating cantilever, the coatings are subjected to over 3600 compression/tension stress cycles applied by the ice accretion per test run. By the end of the 16 cycles, the coatings had experienced an estimated 58000 compressing/tension cycles. This type of loading has been shown to damage structured aluminum surfaces (Vercillo et al., 2019).

Further details on the durability of the coated aluminum under ice delamination testing are revealed by SEM in Figure 49. As a pre-treatment before the coating process the anodized aluminum substrates were exposed to a highly corrosive environment of HCl vapour. The anodic oxide layer was thereby etched to the

microstructural shape shown in Figure 49(a). The “fuzziness” on the oxide is from the SNF. Following ice adhesion tests, Figure 49(b) shows that the microstructure collapsed onto itself. The SNF coating, however, remained attached to the oxide, guaranteeing a low adhesion to atmospheric ice.

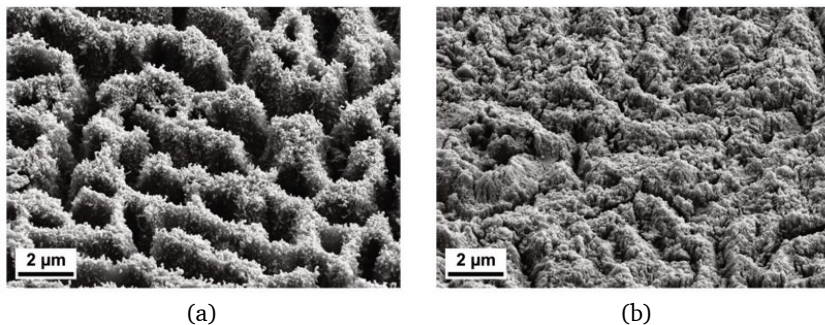


Figure 49: High magnification SEM image of the SNF-coated aluminum surface before (a) and after (b) 16 cycles of ice adhesion testing. Reprinted from (Laroche et al., 2021) under the Creative Commons License, CC BY 4.0.

Details of the effect of the coating process are given by the SEM images shown in Figure 50. The oxide layer appears to be peeling off in some areas of Figure 50(a). Exposure to HCl vapour tends to etch metal oxides. With the concentration and duration of exposure used for preparing the surfaces, evidence suggests that the oxide was etched down to the base passivation layer. Following ice adhesion tests (Figure 50(b)), one can observe that the loose oxide portions have been removed, and only a patchy coated oxide layer remains. Despite the removal of the coated oxide layer, the ice adhesion strength remained the lowest measured on an aluminum substrate in this study.

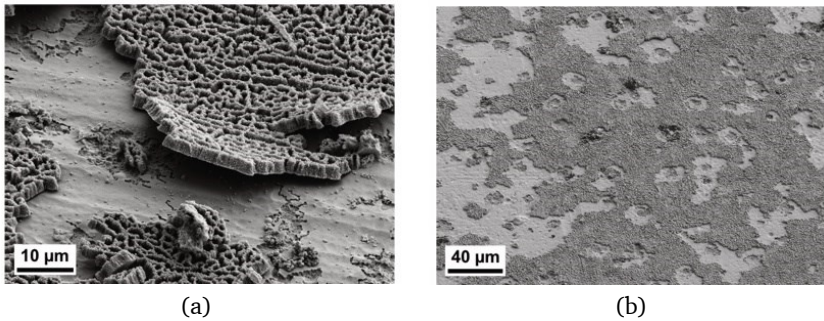


Figure 50: Low magnification SEM image of the SNF-coated aluminum surface before (a) and after (b) 16 cycles of ice adhesion testing. Reprinted from (Laroche et al., 2021) under the Creative Commons License, CC BY 4.0.

Since part of the preparation process prior to initiating chemical growth involved etching in a highly corrosive hydrochloric acid vapour, a thick initial oxide layer was needed. Tartaric sulfuric anodization, described in Section 3.4 above, was used to grow a thick alumina layer on the surface of the alloy before the coating process. Etchant managed to reach the oxide passivation layer, which is a thin uniform oxide layer at the base of an anodic oxide. Weakening of the passivation layer forced the collapse of many columnar pores, giving the oxide a microstructure. The microstructure is useful for protecting the coating between peaks. However, the weakening of the passivation layer also made the oxide more susceptible to delamination under the shearing and peeling stress of the ice adhesion test. The result was that the coating remained intact on the oxide layer, but the oxide layer detached from the bulk. On the exterior of an aircraft, the loss of the oxide layer can accelerate component failure. With only a native oxide, the metal alloy would be highly susceptible to erosive damage, and salt-fog corrosion, a common environment in warm, humid areas on the planet.

4.9.2 Dry and Lubricant-Infused Silicone Nanofilament Coatings on Titanium

Compared to a solid-solid interface, a solid-fluid interface is highly inefficient at transmitting stress. That is especially true for shear stress, where the fluid will likely slip. Theoretically, the interfacial shear strength of ice on a film of lubricant is near null. Under aerodynamic forces, excess lubricant is sheared away from a lubricant-infused surfaces and is forced into the depths of the surface pores, if present. When ice forms on such a surface, aerodynamic pressure can no longer push lubricant deep into a surface, allowing the lubricant to resurface. Lubricant may seep into porous ice due to strong capillary attraction. In this scenario, the ice would have very little bond strength with the lubricant infused surface but would have drained some lubricant out. Porous nanostructures have been shown to be able to retain some lubricant due to strong capillary forces.

The ice adhesion strength (IAS) on a silicone nanofilament coating infused with silicone oil was tested in the same way as aluminum substrates coated with silicone nanofilaments (Section 4.9) as described in Section 3.3.2. Results are plotted in Figure 51. The two control surfaces have been discussed in Section 4.3 above. The IAS on the fluorinated SNF (Ti6Al4V fSNF) coating was less than or equal to that of the PFPE-coated TiO₂-nanotubes (Ti6Al4V nTiO₂ PFPE). It was especially lower in the glaze ice condition. In the glaze ice condition, the impact energy of droplets was higher than in the rime and mixed conditions, suggesting that the lower IAS was related to the different droplet impact behaviour (a result of different impact speed, frequency, and temperature). Due to their high aspect ratio, the fact that each filament is fixed to the substrate at only one end, and the low elastic modulus of silicone, the silicone nanofilaments are likely flexible. It is therefore a reasonable assumption that the silicone coating provided a soft bed to cushion the impact of droplets and that reduced pore penetration. The IAS

on the lubricant infused silicone nanofilaments was slightly lower than on the dry fluorinated SNF. Notably, in the mixed/rime condition, bending due to thermal contraction seemed sufficient to cause partial delamination of the ice; an event that seldom occurs on most icephobic surfaces. The mechanism of ice detachment is discussed in Appendix A.

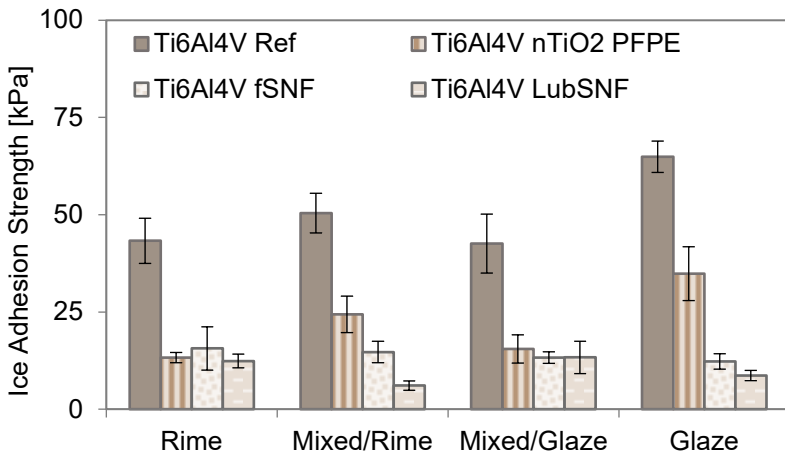


Figure 51: Ice adhesion strength on titanium as-received (Ti6Al4V Ref), with TiO₂ nanotubes and PFPE (nTiO₂ PFPE), with TiO₂ nanotubes coated with fluorinated silicone nanofilaments (fSNF), and with TiO₂ nanotubes coated with silicone nanofilaments and infused with 100 cSt silicone oil (LubSNF).

In terms of durability of Ti6Al4V LubSNF, there was no trend of ice adhesion strength with the number of consecutive icing cycles for all icing conditions. Only in the mixed/glaze condition did the ice adhesion strength begin to increase after the second icing cycle. The absence of a trend can be explained by the short amount of time that the substrate was in contact with ice. Other research groups have measured a trend with consecutive icing cycles, but their measurement procedure involved a time delay of over 16 hours between ice accretion and ice removal. That amount of time was

sufficient for lubricant to wick into porous ice, thus draining the lubricant reservoir from within the surface. Figure 52 shows the ice adhesion strength measured on the lubricant infused surface with cumulative ice exposure time. The ice exposure time was a consequence of ice accretion conditions. It was not a controlled independent variable. Glaze ice, which accreted the fastest, was in contact with the substrate surface for the least amount of time. Mixed/rime ice was the slowest to accrete, and therefore was in contact with the surface for the longest time. The contact time with the surface is considered here to begin at the beginning of ice formation (a few seconds after the supercooled droplet spray begins). The lubricant was replenished before every new icing condition so the abscissa in the figure starts at 0 for each condition. The relation between the lubrication state (overfilled, perfectly filled, underfilled, and any in-between states) and the apparent ice adhesion strength has not been firmly established, although it is believed that a correlation exists. A positive linear trend can be drawn for mixed glaze ice (increase in ice adhesion strength of 0.19 kPa/min. of contact time with ice).

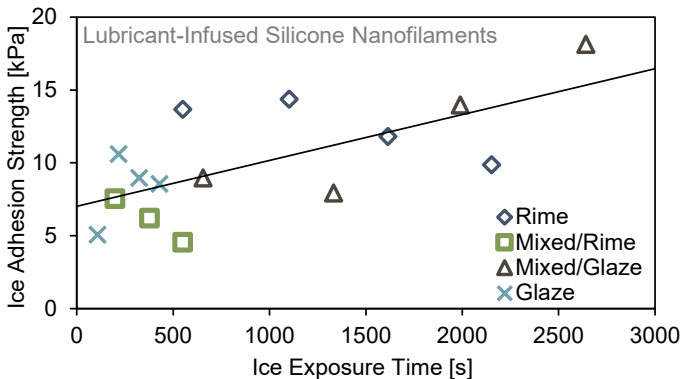


Figure 52: Development of ice adhesion strength with ice exposure time (which is a function successive icing cycles) of a lubricant-infused silicone nanofilament network grown on the anodic oxide of a Ti6Al4V.

The reason that the effect is more prominent for mixed/glaze ice is the temperature-dependant viscosity of the lubricant and the time that it takes to accrete the desired ice thickness. Glaze and mixed/glaze conditions were carried out at the same temperature, but high LWC and airspeed used for the glaze condition meant that exposure time was limited to under 200 s every cycle. Over 2500 s of icing exposure at -5 °C the ice adhesion strength nearly doubled from just under 10 kPa until 18 kPa. The ending IAS was still below that needed for aerodynamic ice delamination, but the increasing trend suggests some long-term instability. If the experiment were carried out for more icing cycles without replenishing the lubricant, a plateau of IAS near that measured for the underlying porous network is expected, but that remains to be measured.

In summary, the silicone nanofilaments (SNF) coating effectively reduced ice adhesion strength on both aluminium and titanium alloys. The coating process damaged the aluminium oxide, whereas the titanium substrate was unaffected. After 16 cycles of ice adhesion testing, the silicone nanofilaments were mechanically damaged, but a base silicone layer remained, ensuring continually low ice adhesion strength. The only surface that appeared undamaged by ice adhesion testing was the lubricant infused SNF network, but that may have been because the lubricant was replenished after every fourth icing/deicing cycle. A closer look at ice adhesion data of the lubricant infused surface shows that ice began to detach even before forced vibration of the substrate. Thus, consistently low ice adhesion strength was achieved on aircraft alloys.

5 Summary and Conclusions

In this thesis, two problems related to the design of icephobic surfaces for aerospace have been addressed. The first is the determination of the properties of a surface to which ice will not stick. The second is the method for measuring the adhesion strength of ice to a surface.

5.1 Improvements to the Method of Measurement of Ice Adhesion Strength

Systems for measuring ice adhesion strength exist for several levels of surface maturity – from rudimentary tests for the early development of icephobic surfaces to highly engineered systems that mimic real icing conditions. None of these methods is universal, nor accepted as a standard. For that reason, each testing facility performs their own version of a test method style that suits their target application. Here, a vibrating cantilever method was used to measure ice adhesion strength to surfaces in-situ within an icing wind tunnel capable of simulating a range of in-flight icing conditions. As opposed to a pure mode I or mode II adhesion test, this mixed-mode adhesion test resembles de-icing systems used on aircraft such as the inflatable pneumatic boot and experimental vibration systems.

The vibrating cantilever ice adhesion test method relies on the user's knowledge of several mechanical and geometrical material parameters of both ice and substrate. The relative importance of each of these parameters was unknown in the field. In this thesis, a comprehensive uncertainty analysis was performed according to the Guide to the Expression of Uncertainty in Measurement (GUM), revealing that ice thickness and ice Young's Modulus were the most important contributors to the uncertainty of interfacial shear stress.

Uncertainty related to ice thickness is inevitably due to the method of ice growth, which is by spray of supercooled water droplets. On the other hand, the uncertainty related to the Young's modulus of ice (typically assumed from literature) could be reduced by validating its value with experimental measurements.

A method was defined for the experimental measurement of the Young's modulus of ice using the ice adhesion strength measurement setup without any modification. By analyzing the ratio between strain measured and maximum deflection of the cantilever, one could deduce the Young's modulus of ice by iteratively solving a finite element model with the experimental geometric parameters. The measurement showed that the Young's modulus of ice grown under the same conditions used during ice adhesion strength tests was 20-50 % lower than the literature value.

5.2 Identification of a suitable Icephobic Surface for Aerospace

With the initiative of the aerospace industry to drastically reduce emissions, aircraft are being developed with novel emission-free propulsion systems. Whereas on conventional aircraft, hot air bled from turbofan engines is typically used to heat critical surfaces to prevent ice from forming, this air is not available on new types of aircraft, creating a demand for new, more efficient, ice protection systems. Icephobic surfaces could theoretically be the answer to that demand, or at least reduce the energy consumption of legacy ice protection systems.

Of the numerous icephobic surfaces produced over the years, none has passed the strict durability requirements imposed by the aerospace industry. In this thesis, the durability of coatings designed to be icephobic was tested before their icephobicity (or ice adhesion strength). Rain erosion tests of several superhydrophobic surfaces produced by laser patterning, thermal spray, physical vapour

deposition, or conventional painting showed that laser patterned surfaces were the most durable. Ice adhesion testing of these aluminum and stainless steel surfaces showed poor performance, and only those produced on titanium showed lower ice adhesion strength than the untreated control. Modified polyurethane aircraft paint showed a 30% reduction in ice adhesion strength compared to standard polyurethane aircraft paint. Although this result showed that it is possible to produce a low-ice adhesion polyurethane aircraft paint, a more significant reduction would be needed to motivate aircraft manufacturers to add a production step.

Evaluation of roughness effects on ice adhesion strength revealed that at the μm scale, ice adhesion strength increased linearly with Ra and Rz. The superposition of a nanometer-scale roughness with a hydrophobic chemistry produced the lowest ice adhesion strength among the surfaces tested.

Silicone nanofilament coatings provide nanoscale roughness with intrinsic hydrophobicity. In this thesis, these coatings have been tested in high-speed icing conditions for the first time. The nanofilament coating was grown on polyester fabric, placed on a solid airfoil shape in an icing wind tunnel, and exposed to high-speed airflow with liquid water droplets at temperatures above and below freezing. After exposure to droplet clouds moving at less than 120 m/s, the coated fabric showed water roll-off-angles below 20° , indicating it was a coating durable enough for airspeeds typically experienced during icing encounters. Following 30 minutes of icing exposure, the water droplet roll-off-angle increased to 40° in the periphery of the airfoil's leading-edge region. This result showed that the coating could partially withstand several icing/de-icing cycles.

The silicone nanofilament coating was also grown on aluminum alloy and titanium alloy. The aluminum alloy coating appeared to generate a microstructure in the underlying anodic oxide. The reduction in ice adhesion strength was 50% relative to the untreated

surface. When the silicone nanofilament coating was fluorinated, this reduction increased to 70%. On titanium alloy, the fluorinated silicone nanofilament coating achieved an ice adhesion strength reduction of 70% with respect to the untreated surface. When a silicone nanofilament coating on titanium was infused with lubricant, the ice adhesion strength dropped by 80% relative to the untreated titanium alloy. Moreover, this low ice adhesion strength on the lubricant-infused silicone nanofilaments endured 4 icing/de-icing cycles, showing the potential for short term durability in icing conditions.

5.3 Outlook

The contributions of this thesis are the advancement of the vibrating cantilever ice adhesion test method, and the durability and ice adhesion testing of a multitude of superhydrophobic surfaces, in particular silicone nanofilament surfaces. Recommendations for future work along the path toward ice adhesion test method standardization, and to improving the durability of low-ice-adhesion surfaces are given below.

The shape of ice plays a role in the calculation of interfacial shear stress. As a future work, it is recommended to analyse these shapes to come up with a correction factor for the factor, C . Additionally, a finite element analysis should be performed for the purpose of determining the maximum interfacial shear stress, and peeling stress along the interface of the beam. With sufficient understanding of the deterministic factors, one can then determine a pre-factor to apply to the average interfacial shear stress calculated analytically. These maximum stress values could be used as input for the design of mechanical de-icing systems.

The silicone nanofilament surfaces showed ice adhesion strength ~80% lower than untreated surfaces considering titanium substrates. On aluminum substrates, the advantage was slightly

lower at 50-75%. Despite slightly poorer advantages on aluminum, it is generally preferred over titanium because of the relative cost. A disadvantage of the coating method was damage to the anodic oxide of aluminum, which is needed for corrosion protection. It is expected that the etching process prior to coating with silicone nanofilaments can be optimized to minimize damage to the protective oxide. Another improvement to durability can be made by fluorination with a non-halogenated silane such as 1H,1H,2H,2H-perfluoro(decyl)triethoxysilane instead of the trichlorosilane. This substitution would prevent the further dissolution of alumina due to processing but would still provide an enhanced chemical hydrophobicity.

The lubricant infused coating was sufficiently durable for low-cycle tests – ice adhesion strength remained below 20 kPa after 4 de-icing cycles. The natural progression of this durability study would be to expose the coating to ice for a longer time, and for more de-icing cycles. Lubricant infiltration rate is inversely dependent on lubricant viscosity. The current understanding is that lubricant depletion from the SNF coating is caused by competing infiltration of ice. Therefore, it is hypothesized that if the lubricant viscosity were increased, the infiltration of lubricant into ice would be slowed, thereby increasing the time before lubricant needs to be replenished. Since this coating performed exceptionally well in ice adhesion tests, the next step would be to test in on an aircraft component. It would be most appropriate for a component which is not in directly on the exterior of the aircraft, but rather within the contours of an engine intake, for example, on a turboprop aircraft.

The combination of surface modification techniques such as thermal spray with laser-patterning can produce durable and superhydrophobic surfaces (Toma et al., 2021). In addition, recent advancements to conventional thermal spray techniques have shown low ice adhesion for sessile ice (Mohseni et al., 2021). It would be

beneficial to study their behaviour under atmospheric icing as was done in this thesis.

In the end, the decision of the icephobic surface technology to use depends largely on the environment that a component is in. The natural forces that the surface is subjected to, and the type of ice that typically accretes can vary by position on an aircraft. In the selection of a surface, one must consider that the surface has passed the most relevant ice adhesion test and durability tests. Therefore, ice adhesion test standardization should include a consideration for the most relevant fracture modes and the selection of an appropriate ice formation method.

6 Bibliography

- Abbott, I. H., & Von Doenhoff, A. E. (1959). *Theory of Wing Sections*. Dover Publications, Inc.
- Akitegetse, C., Volat, C., & Farzaneh, M. (2008). Measuring bending stress on an ice/aluminium composite beam interface using an embedded piezoelectric PVDF (polyvinylidene-fluoride) film sensor. *Measurement Science and Technology*, 19(6). <https://doi.org/10.1088/0957-0233/19/6/065703>
- Aliotta, F., Giaquinta, P. V., Ponterio, R. C., Prestipino, S., Saija, F., Salvato, G., & Vasi, C. (2014). Supercooled water escaping from metastability. *Scientific Reports*, 4, 1–5. <https://doi.org/10.1038/srep07230>
- Antonini, C., Innocenti, M., Horn, T., Marengo, M., & Amirfazli, A. (2011). Understanding the effect of superhydrophobic coatings on energy reduction in anti-icing systems. *Cold Regions Science and Technology*, 67(1–2), 58–67. <https://doi.org/10.1016/j.coldregions.2011.02.006>
- Artus, G. R. J. J., Jung, S., Zimmermann, J., Gautschi, H.-P. H. P., Marquardt, K., & Seeger, S. (2006). Silicone Nanofilaments and Their Application as Superhydrophobic Coatings. *Advanced Materials*, 18(20), 2758–2762. <https://doi.org/10.1002/adma.200502030>
- Artus, G. R. J., Oliveira, S., Patra, D., & Seeger, S. (2017). Directed In Situ Shaping of Complex Nano- and Microstructures during Chemical Synthesis. *Macromolecular Rapid Communications*, 38(4), 1600558. <https://doi.org/10.1002/marc.201600558>

- Balakumar, P. (2017). Direct numerical simulation of flows over a NACA-0012 airfoil at low and moderate reynolds numbers. *47th AIAA Fluid Dynamics Conference, June*, 1–19. <https://doi.org/10.2514/6.2017-3978>
- Balordi, M., Cammi, A., Chemelli, C., & Magistris, G. S. De. (2019). *Effect of micro-roughness of Aluminum alloy surface on anti-ice and durability properties of hierarchical structured coatings*. 6082, 1–5.
- Blackburn, C., Laforte, C., & Laforte, J.-L. (2000). Apparatus for Measuring the Adhesion Force of a Thin Ice Sheet on a substrate. *International Workshop of Atmospheric Ice on Structures*, 5.
- Bohren, C. F. (2004). The Freezing of Streams and Ponds: A Simple—But Uncomfortable—Experiment. *The Physics Teacher*, 42(9), 522–525. <https://doi.org/10.1119/1.1828721>
- Boinovich, L., Emelyanenko, A. M., Korolev, V. V., & Pashinin, A. S. (2014). Effect of wettability on sessile drop freezing: When superhydrophobicity stimulates an extreme freezing delay. *Langmuir*, 30(6), 1659–1668. <https://doi.org/10.1021/la403796g>
- Bragg, M. B., Gregorek, G. M., & Lee, J. D. (1986). Airfoil Aerodynamics in Icing Conditions. *Journal of Aircraft*, 23(1), 76–81. <https://doi.org/10.2514/3.45269>
- Brassard, J. D., Laforte, C., Guerin, F., & Blackburn, C. (2019). Icephobicity: Definition and measurement regarding atmospheric icing. *Advances in Polymer Science*, 284, 123–143. https://doi.org/10.1007/12_2017_36
- Brown, S., Lengaigne, J., Sharifi, N., Pugh, M., Moreau, C., Dolatabadi,

-
- A., Martinu, L., & Klemberg-Sapieha, J. E. (2020). Durability of superhydrophobic duplex coating systems for aerospace applications. *Surface and Coatings Technology*, 401(April). <https://doi.org/10.1016/j.surfcoat.2020.126249>
- Bureau d'Enquêtes et d'Analyses. (2012). *Rapport final: Accident survenu le 1er juin 2009 à l'Airbus A330-203 immatriculé F-GZCP exploité par Air France vol AF 447 Rio de Janeiro - Paris*.
- Busch, A. H., Hoff, G., Langbein, G., Taylor, G., Jenkins, D. C., Fyall, A. A., Jones, R. F., & Harper, T. W. (1966). Rain Erosion Properties of Materials. *Philosophical Transactions of the Royal Society of London. Series A, Mathematical and Physical Sciences*, 260(1110), 168–181.
- Cao, Y., Wu, Z., Su, Y., & Xu, Z. (2015). Aircraft flight characteristics in icing conditions. *Progress in Aerospace Sciences*, 74, 62–80. <https://doi.org/10.1016/j.paerosci.2014.12.001>
- Cassie, A. B. D., & Baxter, S. (1944). Wettability of porous surfaces. *Transactions of the Faraday Society*, 40(5), 546. <https://doi.org/10.1039/tf94444000546>
- Cole, J., & Sand, W. (1991). Statistical Study of Aircraft Icing Accidents. *29th Aerospace Sciences Meeting*, 0558. <https://doi.org/10.2514/6.1991-558>
- Deng, T., Varanasi, K. K., Hsu, M., Bhate, N., Keimel, C., Stein, J., & Blohm, M. (2009). Nonwetting of impinging droplets on textured surfaces. *Applied Physics Letters*, 94(13), 1–4. <https://doi.org/10.1063/1.3110054>
- Diebold, U. (2003). The surface science of titanium dioxide. *Surface*

Science Reports, 48(5–8), 53–229.
[https://doi.org/10.1016/S0167-5729\(02\)00100-0](https://doi.org/10.1016/S0167-5729(02)00100-0)

Donadei, V., Koivuluoto, H., Sarlin, E., & Vuoristo, P. (2020). Icephobic Behaviour and Thermal Stability of Flame-Sprayed Polyethylene Coating: The Effect of Process Parameters. *Journal of Thermal Spray Technology*, 29(1–2), 241–254.
<https://doi.org/10.1007/s11666-019-00947-0>

Dupigny-Giroux, L. A. (2000). Impacts and consequences of the ice storm of 1998 for the North American north-east. *Weather*, 55(1), 7–15. <https://doi.org/10.1002/j.1477-8696.2000.tb04012.x>

EASA. (2011). *Type-Certificate Data Sheet EASA.IM.A.018 Maule M-4* (Issue 6).

Extrand, C. W., & Kumagai, Y. (1996). Contact angles and hysteresis on soft surfaces. *Journal of Colloid and Interface Science*, 184(1), 191–200. <https://doi.org/10.1006/jcis.1996.0611>

FAA. (2009). *Electronic Code of Federal Regulations - Title 14 - Chapter 1 - Subchapter F - Part 91*. https://www.ecfr.gov/cgi-bin/text-idx?c=ecfr&sid=3efaad1b0a259d4e48f1150a34d1aa77&rgn=div5&view=text&node=14:2.0.1.3.10&idno=14#se14.2.91_1527

FAA. (2012). Aviation Maintenance Technician Handbook. In *Aviation Maintenance Technician Handbook* (Vol. 1, Issue 5). U.S. Department of Transportation.
<https://doi.org/10.1017/CBO9781107415324.004>

Feher, L., & Thumm, M. (2006). Design of avionic microwave de-/anti-icing systems. *Advances in Microwave and Radio Frequency*

Processing - Report from the 8th International Conference on Microwave and High Frequency Heating, 695–702.
https://doi.org/10.1007/978-3-540-32944-2_76

- Fyall, A. A. (1966). Practical Aspects of Rain Erosion of Aircraft and Missiles. *Philosophical Transactions of the Royal Society of London. Series A, Mathematical and Physical Sciences*, 260(1110), 161–167.
- Gammon, P. H., Kieft, H., Clouter, M. J., & Denner, W. W. (1983). Elastic constants of artificial and natural ice samples by Brillouin spectroscopy. *Journal of Glaciology*, 29(103), 433–460.
<https://doi.org/10.1017/S0022143000030355>
- Gayer, K. H., Thompson, L. C., & Zajicek, O. T. (1958). The Solubility of Aluminum Hydroxide in Acidic and Basic Media at 25 °C. *Canadian Journal of Chemistry*, 36(9), 1268–1271.
<https://doi.org/10.1139/v58-184>
- Geyer, F., D'Acunzi, M., Sharifi-Aghili, A., Saal, A., Gao, N., Kaltbeitzel, A., Sloop, T.-F., Berger, R., Butt, H.-J., & Vollmer, D. (2020). When and how self-cleaning of superhydrophobic surfaces works. *Science Advances*, 6(3), 1–11.
<https://doi.org/10.1126/sciadv.aaw9727>
- Geyer, F., Schönecker, C., Butt, H. J., & Vollmer, D. (2017). Enhancing CO₂ Capture using Robust Superomniphobic Membranes. *Advanced Materials*, 29(5), 1–6.
<https://doi.org/10.1002/adma.201603524>
- Golovin, K. (2017). *Design and Application of Surfaces with Tunable Adhesion to Liquids and Solids*.

- Golovin, K., Boban, M., Mabry, J. M., & Tuteja, A. (2017). Designing Self-Healing Superhydrophobic Surfaces with Exceptional Mechanical Durability. *ACS Applied Materials and Interfaces*, 9(12), 11212–11223. <https://doi.org/10.1021/acsami.6b15491>
- Golovin, K., Dhyani, A., Thouless, M. D., & Tuteja, A. (2019). Low-interfacial toughness materials for effective large-scale deicing. *Science*, 364(6438), 371–375. <https://doi.org/10.1126/science.aav1266>
- Golovin, K., & Tuteja, A. (2017). A predictive framework for the design and fabrication of icephobic polymers. *Science Advances*, 3(9), 1–10. <https://doi.org/10.1126/sciadv.1701617>
- Goraj, Z. (2004). An overview of the deicing and anti-icing technologies with prospects for the future. *24th International Congress of the Aeronautical Sciences*, 1–11.
- Greenly, K. H. (1963). Recent Developments in Aircraft Ice Protection. *Aircraft Engineering and Aerospace Technology*, 35(4), 92–96. <https://doi.org/10.1108/eb033713>
- Hassan, M. F., Lee, H. P., & Lim, S. P. (2010). The variation of ice adhesion strength with substrate surface roughness. *Measurement Science and Technology*, 21(7). <https://doi.org/10.1088/0957-0233/21/7/075701>
- Hauer, L., Wong, W. S. Y., Donadei, V., Hegner, K. I., Kondic, L., & Vollmer, D. (2021). How Frost Forms and Grows on Lubricated Micro- And Nanostructured Surfaces. *ACS Nano*. <https://doi.org/10.1021/acsnano.0c09152>
- Heinrich, A., Ross, R., Zumwalt, G., Provorse, J., Padmanabhan, V.,

-
- Thompson, J., & Riley, J. (1991a). *Aircraft Icing Handbook Volume 3 of 3*.
<http://www.dtic.mil/dtic/tr/fulltext/u2/a238041.pdf>
- Heinrich, A., Ross, R., Zumwalt, G., Provorse, J., Padmanabhan, V., Thompson, J., & Riley, J. (1991b). *Aircraft Icing Handbook Volume 1 of 3*. ADA238040
- Heymann, F. J. (1970, December). Erosion by liquids. *Machine Design*, 118–124.
- Howell, C., Vu, T. L., Johnson, C. P., Hou, X., Ahanotu, O., Alvarenga, J., Leslie, D. C., Uzun, O., Waterhouse, A., Kim, P., Super, M., Aizenberg, M., Ingber, D. E., & Aizenberg, J. (2015). Stability of Surface-Immobilized Lubricant Interfaces under Flow. *Chemistry of Materials*, 27(5), 1792–1800.
<https://doi.org/10.1021/cm504652g>
- Huang, X., Tepylo, N., Pommier-Budinger, V., Budinger, M., Bonaccorso, E., Villedieu, P., & Bennani, L. (2019). A survey of icephobic coatings and their potential use in a hybrid coating/active ice protection system for aerospace applications. *Progress in Aerospace Sciences*, 105, 74–97.
<https://doi.org/10.1016/j.paerosci.2019.01.002>
- Isaac, G. A., Cober, S. G., Strapp, J. W., Korolev, A. V., Tremblay, A., & Marcotte, D. L. (2001). Recent Canadian research on aircraft in-flight icing. *Canadian Aeronautics and Space Journal*, 47(3), 213–221.
- Javan-Mashmool, M., Volat, C., & Farzaneh, M. (2006a). A new method for measuring ice adhesion strength at an ice-substrate interface. *Hydrological Processes*, 20(4), 645–655.

<https://doi.org/10.1002/hyp.6110>

Javan-Mashmool, M., Volat, C., & Farzaneh, M. (2006b). A new method for measuring ice adhesion strength at an ice–substrate interface. *Hydrological Processes*, 20(4), 645–655. <https://doi.org/10.1002/hyp.6110>

Javan-Mashmool, M., Volat, C., & Farzaneh, M. (2005). A Theoretical Model for Measuring Stress Induced by a Vibrating load at Ice/Material Interface. *International Workshop on Atmospheric Icing of Structures XI, June*.

Jones, S. M., Reveley, M. S., Evans, J. K., & Barrientos, F. (2008). *Subsonic Aircraft Safety Icing Study. NASA/TM-2008-215107*.

Jonsson, R. (2007). *Characterisation and Validation of a Pulsating Jet Erosion Test*. Luleå University of Technology.

Jung, S., Dorrestijn, M., Raps, D., Das, A., Megaridis, C. M., & Poulidakos, D. (2011). Are superhydrophobic surfaces best for icephobicity? *Langmuir*, 27(6), 3059–3066. <https://doi.org/10.1021/la104762g>

Kepler, J. (1611). *On the Six-Cornered Snowflake*. Godfried Tampach.

Koishi, T., Yasuoka, K., Fujikawa, S., Ebisuzaki, T., & Xiao, C. Z. (2009). Coexistence and transition between Cassie and Wenzel state on pillared hydrophobic surface. *Proceedings of the National Academy of Sciences of the United States of America*, 106(21), 8435–8440. <https://doi.org/10.1073/pnas.0902027106>

Koivuluoto, H., Hartikainen, E., & Niemelä-Anttonen, H. (2020). Thermally sprayed coatings: Novel surface engineering strategy towards icephobic solutions. *Materials*, 13(6).

<https://doi.org/10.3390/ma13061434>

- Kreder, M. J., Alvarenga, J., Kim, P., & Aizenberg, J. (2016). Design of anti-icing surfaces: smooth, textured or slippery? *Nature Reviews Materials*, *1*(1), 15003. <https://doi.org/10.1038/natrevmats.2015.3>
- Kulinich, S. A. A., & Farzaneh, M. (2009). Ice adhesion on superhydrophobic surfaces. *Applied Surface Science*, *255*(18), 8153–8157. <https://doi.org/10.1016/j.apsusc.2009.05.033>
- Kulinich, S. A., Farhadi, S., Nose, K., & Du, X. W. (2011). Superhydrophobic surfaces: Are they really ice-repellent? *Langmuir*, *27*(1), 25–29. <https://doi.org/10.1021/la104277q>
- Kulinich, S. A., & Farzaneh, M. (2009). How wetting hysteresis influences ice adhesion strength on superhydrophobic surfaces. *Langmuir*, *25*(16), 8854–8856. <https://doi.org/10.1021/la901439c>
- Laforte, C. (2001). Étude de l'adhérence de la glace sur des solides à caractère glaciophobe [Université du Québec à Chicoutimi]. In *Étude de l'Adhérence de la glace sur des solides à caractère glaciophobe*. <https://doi.org/10.1522/12599107>
- Laforte, C. (2002). How a solid coating can reduce the adhesion of ice on a structure. *IWAIS, January 2002*, 1–6.
- Laforte, J. L., Allaire, M. A., & Laflamme, J. (1998). State-of-the-art on power line de-icing. *Atmospheric Research*, *46*(1–2), 143–158. [https://doi.org/10.1016/S0169-8095\(97\)00057-4](https://doi.org/10.1016/S0169-8095(97)00057-4)
- Landy, M., & Freiburger, A. (1967). Studies of ice adhesion. I. Adhesion

- of ice to plastics. *Journal of Colloid And Interface Science*, 25(2), 231–244. [https://doi.org/10.1016/0021-9797\(67\)90026-4](https://doi.org/10.1016/0021-9797(67)90026-4)
- Laroche, A. (2018, April). Ice Adhesion Test Data for Ice-Phobic and Durability Testing of Lubricant Impregnated Slippery Surfaces. *14th Zsigmondy Colloquium of the German Colloid Society*.
- Laroche, A., Bottone, D., Seeger, S., & Bonaccuso, E. (2021). Silicone nanofilaments grown on aircraft alloys for low ice adhesion. *Surface and Coatings Technology*, 410(January), 126971. <https://doi.org/10.1016/j.surfcoat.2021.126971>
- Laroche, A., Grasso, M. J., Dolatabadi, A., & Bonaccuso, E. (2020). Tensile and Shear Test Methods for Quantifying the Ice Adhesion Strength to a Surface. In K. L. Mittal & C.-H. Choi (Eds.), *Ice Adhesion: Mechanism, Measurement and Mitigation* (1st ed., pp. 237–284). Wiley. <https://doi.org/10.1002/9781119640523.ch9>
- Laroche, A., Ritzen, L., Guillén, J. A. M., Vercillo, V., D’Acunzi, M., Sharifi Aghili, A., Hussong, J., Vollmer, D., & Bonaccuso, E. (2020). Durability of Superamphiphobic Polyester Fabrics in Simulated Aerodynamic Icing Conditions. *Coatings*, 10(11), 1058. <https://doi.org/10.3390/coatings10111058>
- Laroche, A., Vercillo, V., Karpen, N., & Bonaccuso, E. (2019). Novel Setup for Measuring Ice Adhesion Strengths in an Icing Wind Tunnel. *SAE 2019 International Conference on Icing of Aircraft, Engines, and Structures*.
- Lau, K. K. S., Bico, J., Teo, K. B. K., Chhowalla, M., Amaratunga, G. A. J., Milne, W. I., McKinley, G. H., & Gleason, K. K. (2003). Superhydrophobic Carbon Nanotube Forests. *Nano Letters*, 3(12), 1701–1705. <https://doi.org/10.1021/nl034704t>

-
- Leary, W. M. (2002). We Freeze to Please: A History of NASA's Icing Research Tunnel and the Quest for Flight Safety. In *The NASA History Series*. National Aeronautics and Space Administration.
- Lengaigne, J., Bousser, E., Brown, S., Batory, D., Dolatabadi, A., Martinu, L., & Klemberg-Sapieha, J. E. (2019). Impact dynamics of supercooled microdroplets on water-repellent coatings. *Thin Solid Films*, 688(May), 137309. <https://doi.org/10.1016/j.tsf.2019.05.028>
- Lewis, W. (1947). *Technical Note No. 1393: A Flight Investigation of the Meteorological Conditions Conducive to the Formation of Ice on Airplanes*.
- Maitra, T., Jung, S., Giger, M. E., Kandrical, V., Ruesch, T., & Poulidakos, D. (2015). Superhydrophobicity vs. Ice Adhesion: The Quandary of Robust Icephobic Surface Design. *Advanced Materials Interfaces*, 2(16). <https://doi.org/10.1002/admi.201500330>
- Makkonen, L. (2000). Models for the growth of rime, glaze, icicles and wet snow on structures. *Philosophical Transactions of the Royal Society A: Mathematical, Physical and Engineering Sciences*, 358(1776), 2913–2939. <https://doi.org/10.1098/rsta.2000.0690>
- Mankins, J. C. (1995). *Technology Readiness Levels*.
- Marmur, A. (2004). The lotus effect: Superhydrophobicity and metastability. *Langmuir*, 20(9), 3517–3519. <https://doi.org/10.1021/la036369u>
- Mason, J. G., Strapp, J. W., & Chow, P. (2006). The ice particle threat to engines in flight. *44th AIAA Aerospace Sciences Meeting*,

4(January), 2445–2465. <https://doi.org/10.2514/6.2006-206>

Maule Aerospace Technology Inc. (2016). *Maintenance Manual for Maule MX-7-235* (Rev. B).

McDevitt, J. B., & Okuno, A. F. (1985). *Static and Dynamic Pressure Measurements on a NACA 0012 Airfoil in the AMES High Reynolds Number Facility*.

Méndez-Vilas, A., Jódar-Reyes, A. B., & González-Martín, M. L. (2009). Ultrasmall Liquid Droplets on Solid Surfaces: Production, Imaging, and Relevance for Current Wetting Research. *Small*, 5(12), 1366–1390. <https://doi.org/10.1002/sml.200800819>

Mertens, T., Raps, D., & Wehr, J. (2015). *Self-Cleaning and Superhydrophobic Surfaces Based on TiO₂ Nanotubes* (Patent No. 2015/0299889 A1). <https://patents.google.com/patent/US20150299889A1/en>

Messinger, B. L. (1953). Equilibrium Temperature of an Unheated Icing Surface as a Function of Air Speed. *Journal of the Aeronautical Sciences*, 20(1), 29–42. <https://doi.org/10.2514/8.2520>

Meuler, A. J., McKinley, G. H., & Cohen, R. E. (2010). Exploiting topographical texture to impart icephobicity. *ACS Nano*, 4(12), 7048–7052. <https://doi.org/10.1021/nn103214q>

Meuler, A. J., Smith, J. D., Varanasi, K. K., Mabry, J. M., McKinley, G. H., & Cohen, R. E. (2010). Relationships between Water Wettability and Ice Adhesion. *ACS Applied Materials & Interfaces*, 2(11), 3100–3110. <https://doi.org/10.1021/am1006035>

Miller, R. H., & Ribbens, W. B. (1999a). Detection of the loss of elevator effectiveness due to aircraft icing. *37th AIAA Aerospace*

Sciences Meeting and Exhibit, AIAA-99-0637, 1–7.
<https://doi.org/10.2514/6.1999-637>

Miller, R. H., & Ribbens, W. B. (1999b). The effects of icing on the longitudinal dynamics of an icing research aircraft. *37th Aerospace Sciences Meeting and Exhibit, 0636.*
<https://doi.org/10.2514/6.1999-636>

Milles, S., Vercillo, V., Alamri, S., Aguilar-Morales, A. I., Kunze, T., Bonaccorso, E., & Lasagni, A. F. (2021). Icephobic performance of multi-scale laser-textured aluminum surfaces for aeronautic applications. *Nanomaterials, 11(1), 1–17.*
<https://doi.org/10.3390/nano11010135>

Mohseni, M., Recla, L., Mora, J., Gallego, P. G., Agüero, A., & Golovin, K. (2021). Quasicrystalline Coatings Exhibit Durable Low Interfacial Toughness with Ice. *ACS Applied Materials and Interfaces, 13(30), 36517–36526.*
<https://doi.org/10.1021/acsami.1c08740>

Mora, J., García, P., Muelas, R., & Agüero, A. (2020). Hard Quasicrystalline Coatings Deposited by HVOF Thermal Spray to Reduce Ice Accretion in Aero-Structures Components. *Coatings, 10(3), 1–23.* <https://doi.org/10.3390/coatings10030290>

Morita, K., Kimura, S., & Sakaue, H. (2020). Hybrid system combining ice-phobic coating and electrothermal heating for wing ice protection. *Aerospace, 7(8).*
<https://doi.org/10.3390/AEROSPACE7080102>

Myers, T. G. (2001). Extension to the Messinger model for aircraft icing. *AIAA Journal, 39(2), 211–218.*
<https://doi.org/10.2514/2.1312>

- NASA. (1978). Aircraft Icing. *Journal of Glaciology*, 1(July), 151. <https://doi.org/10.3189/s0022143000007632>
- Niemelä-Anttonen, H., Koivuluoto, H., Tuominen, M., Teisala, H., Juuti, P., Haapanen, J., Harra, J., Stenroos, C., Lahti, J., Kuusipalo, J., Mäkelä, J. M., & Vuoristo, P. (2018). Icephobicity of Slippery Liquid Infused Porous Surfaces under Multiple Freeze–Thaw and Ice Accretion–Detachment Cycles. *Advanced Materials Interfaces*, 5(20), 1–8. <https://doi.org/10.1002/admi.201800828>
- Nilsson, A., & Pettersson, L. G. M. (2015). The structural origin of anomalous properties of liquid water. *Nature Communications*, 6. <https://doi.org/10.1038/ncomms9998>
- Nosonovsky, M., & Hejazi, V. (2012). Why Superhydrophobic Surfaces Are Not Always Icephobic. *ACS Nano*, 6(10), 8488–8491. <https://doi.org/10.1021/nn302138r>
- Parent, O., & Ilinca, A. (2011). Anti-icing and de-icing techniques for wind turbines: Critical review. *Cold Regions Science and Technology*, 65(1), 88–96. <https://doi.org/10.1016/j.coldregions.2010.01.005>
- Patankar, N. A. (2004). Transition between superhydrophobic states on rough surfaces. *Langmuir*, 20(17), 7097–7102. <https://doi.org/10.1021/la049329e>
- Pericet-Cámara, R., Best, A., Butt, H. J., & Bonaccorso, E. (2008). Effect of capillary pressure and surface tension on the deformation of elastic surfaces by sessile liquid microdrops: An experimental investigation. *Langmuir*, 24(19), 10565–10568. <https://doi.org/10.1021/la801862m>

-
- Pervier, M. (2012). *Mechanics of Ice Detachment Applied To Turbomachinery*. Cranfield University.
- Pervier, M. A., Pervier, H., & Hammond, D. W. (2017). Observation of microstructures of atmospheric ice using a new replica technique. *Cold Regions Science and Technology*, 140(February), 54–57. <https://doi.org/10.1016/j.coldregions.2017.05.002>
- Pervier, M. L. A., Gurrutxaga Lerma, B., Piles Moncholi, E., & Hammond, D. W. (2019). A new test apparatus to measure the adhesive shear strength of impact ice on titanium 6Al-4V alloy. *Engineering Fracture Mechanics*, 214, 212–222. <https://doi.org/10.1016/j.engfracmech.2019.01.039>
- Peterson, A., & Dadone, L. (1980). *Helicopter icing review 1980*.
- Politovich, M. K. (1989). Aircraft Icing Caused by Large Supercooled Droplets. *Journal of Applied Meteorology*, 28(9), 856–868.
- Pommier-Budinger, V., Budinger, M., Rouset, P., Dezitter, F., Huet, F., Wetterwald, M., & Bonaccorso, E. (2018). Electromechanical resonant ice protection systems: Initiation of fractures with piezoelectric actuators. *AIAA Journal*, 56(11), 4400–4411. <https://doi.org/10.2514/1.J056662>
- Przybyszewski, B., Boczkowska, A., Kozera, R., Mora, J., Garcia, P., Agüero, A., & Borrás, A. (2019). Hydrophobic and icephobic behaviour of polyurethane-based nanocomposite coatings. *Coatings*, 9(12), 1–12. <https://doi.org/10.3390/coatings9120811>
- Raps, D., Jung, S., & Strobl, T. (2012). Comparative Evaluation of Icing on Aerodynamic Surfaces. *28th Congress of the International Council of the Aeronautical Sciences*, 23–28.

http://www.icas.org/ICAS_ARCHIVE/ICAS2012/PAPERS/953.PDF

Ratvasky, T. P., & Ranaudo, R. J. (1993). Icing effects on aircraft stability and control determined from flight data - Preliminary results. *31st Aerospace Sciences Meeting & Exhibit*, 0398. <https://doi.org/10.2514/6.1993-398>

Rice, J. R. (1988). Elastic Fracture Mechanics Concepts for Interfacial Cracks. *Journal of Applied Mechanics*, 55(1), 98–103. <https://doi.org/10.1115/1.3173668>

Rico, V. J., López-Santos, C., Villagrà, M., Espinós, J. P., De La Fuente, G. F., Angurel, L. A., Borrás, A., & González-Elipe, A. R. (2019). Hydrophobicity, Freezing Delay, and Morphology of Laser-Treated Aluminum Surfaces. *Langmuir*, 35(19), 6483–6491. <https://doi.org/10.1021/acs.langmuir.9b00457>

Rico, V., Mora, J., García, P., Agüero, A., Borrás, A., González-Elipe, A. R., & López-Santos, C. (2020). Robust anti-icing superhydrophobic aluminum alloy surfaces by grafting fluorocarbon molecular chains. *Applied Materials Today*, 21. <https://doi.org/10.1016/j.apmt.2020.100815>

Rouset, P., Budinger, M., & Pommier-Budinger, V. (2016). Comparison of extensional and flexural modes for the design of piezoelectric ice protection systems. *7th European Conference for Aeronautics and Space Sciences (EUCASS)*, 52(3), 31077.

Rybicki, E. F., Shadley, J. R., Xiong, Y., & Greving, D. (1995). A cantilever beam method for evaluating Young's modulus and Poisson's ratio of thermal spray coatings. *Journal of Thermal Spray Technology*, 4(4), 377–383.

<https://doi.org/10.1007/BF02648639>

- Ryerson, C. C. (2011). Ice protection of offshore platforms. *Cold Regions Science and Technology*, 65(1), 97–110. <https://doi.org/10.1016/j.coldregions.2010.02.006>
- SAE Aerospace. (2003). *Calibration and Acceptance of Icing Wind Tunnels*.
- Sharifi, N., Dolatabadi, A., Pugh, M., & Moreau, C. (2019). Anti-icing performance and durability of suspension plasma sprayed TiO₂ coatings. *Cold Regions Science and Technology*, 159(July 2018), 1–12. <https://doi.org/10.1016/j.coldregions.2018.11.018>
- Sharifi, N., Pugh, M., Moreau, C., & Dolatabadi, A. (2016). Developing hydrophobic and superhydrophobic TiO₂ coatings by plasma spraying. *Surface and Coatings Technology*, 289, 29–36. <https://doi.org/10.1016/j.surfcoat.2016.01.029>
- Stallabrass, J. R., & Price, R. D. (1963). On the adhesion of ice to various materials. *Canadian Aeronautics and Space Journal*, 9, 199–204.
- Stone, A. J. (2007). Water from first principles. *Science*, 315(5816), 1228–1229. <https://doi.org/10.1126/science.1140758>
- Strobl, T., Raps, D., & Hornung, M. (2012). Comparative Evaluation of Ice Adhesion Behavior. *World Academy of Science, Engineering and Technology*, 68, 1673–1678. <http://www.waset.org/journals/waset/v68/v68-298.pdf>
<http://www.waset.org/journals/waset/v68.php>
- Strobl, T., Storm, S., Thompson, D., Hornung, M., & Thielecke, F.

- (2015). Feasibility Study of a Hybrid Ice Protection System. *Journal of Aircraft*, 52(6), 2064–2076. <https://doi.org/10.2514/1.C033161>
- Strobl, Tobias, Raps, D. M., Paulus, D., & Hornung, M. (2013). Evaluation of Roughness Effects on Ice Adhesion. *5th AIAA Atmospheric and Space Environments Conference*, 1–8. <https://doi.org/10.2514/6.2013-2547>
- Ta, D. V., Dunn, A., Wasley, T. J., Kay, R. W., Stringer, J., Smith, P. J., Connaughton, C., & Shephard, J. D. (2015). Nanosecond laser textured superhydrophobic metallic surfaces and their chemical sensing applications. *Applied Surface Science*, 357, 248–254. <https://doi.org/10.1016/j.apsusc.2015.09.027>
- Tetteh, E., & Loth, E. (2020). Reducing static and impact ice adhesion with a self-lubricating icephobic coating (SLIC). *Coatings*, 10(3), 262. <https://doi.org/10.3390/coatings10030262>
- Tobin, E. F., Young, T. M., Raps, D., & Rohr, O. (2011). Comparison of liquid impingement results from whirling arm and water-jet rain erosion test facilities. *Wear*, 271(9–10), 2625–2631. <https://doi.org/10.1016/j.wear.2011.02.023>
- Tobin, Edmond F., Young, T. M., & Raps, D. (2012). Evaluation and correlation of inter-laboratory results from a rain erosion test campaign. *28th Congress of the International Council of the Aeronautical Sciences*, 6, 4957–4966.
- Toma, F. L., Alamri, S., Leupolt, B., Kunze, T., & Barbosa, M. (2021). Functionalization of Suspension Sprayed HVOF TiO₂ Coatings by Direct Laser Interference Patterning. *Journal of Thermal Spray Technology*, 30(5), 1159–1173. <https://doi.org/10.1007/s11666->

021-01181-3

- Tourkine, P., Merrer, M. Le, & Quéré, D. (2009). Delayed freezing on water repellent materials. *Langmuir*, 25(13), 7214–7216. <https://doi.org/10.1021/la900929u>
- Transportation Safety Board of Canada. (2014). *Aviation Investigation Report A14W0181: Severe icing encounter and forced landing* (Issue November).
- Vercillo, V. (2020). *Durable Laser Patterned Metal Surfaces with Enhanced Icephobic Properties for Aerospace Applications*. Technische Universität Dresden.
- Vercillo, V., Cardoso, J. T., Huerta-Murillo, D., Tonnichia, S., Laroche, A., Mayén Guillén, J. A., Ocaña, J. L., Lasagni, A. F., & Bonaccorso, E. (2019). Durability of superhydrophobic laser-treated metal surfaces under icing conditions. *Materials Letters: X*, 3, 100021. <https://doi.org/10.1016/j.mlblux.2019.100021>
- Vercillo, V., Tonnichia, S., Romano, J.-M., García-Girón, A., Aguilar-Morales, A. I., Alamri, S., Dimov, S. S., Kunze, T., Lasagni, A. F., & Bonaccorso, E. (2020). Design Rules for Laser-Treated Icephobic Metallic Surfaces for Aeronautic Applications. *Advanced Functional Materials*, 30(16), 1910268. <https://doi.org/10.1002/adfm.201910268>
- Vukits, T. J. (2002). Overview and risk assessment of icing for transport category aircraft and components. *40th AIAA Aerospace Sciences Meeting and Exhibit, March*, 0811. <https://doi.org/10.2514/6.2002-811>
- Wachsmann, R. (2019). *Aerodynamic Optimization of an In-Situ*

Vibrating Cantilever Ice Adhesion Test. Technical University of Munich.

Waki, H., Oikawa, A., Kato, M., Takahashi, S., Kojima, Y., & Ono, F. (2014). Evaluation of the Accuracy of Young's Moduli of Thermal Barrier Coatings Determined on the Basis of Composite Beam Theory. *Journal of Thermal Spray Technology*, 23(8), 1291–1301. <https://doi.org/10.1007/s11666-014-0145-7>

Wenzel, R. N. (1936). Resistance of solid surfaces to wetting by water. *Industrial and Engineering Chemistry*, 28(8), 988–994. <https://doi.org/10.1021/ie50320a024>

Wermuth, L., Kolb, M., Mertens, T., Strobl, T., & Raps, D. (2015). Superhydrophobic surfaces based on self-organized TiO₂-nanotubes. *Progress in Organic Coatings*, 87, 242–249. <https://doi.org/10.1016/j.porgcoat.2015.05.010>

Wong, W. S. Y., Hegner, K. I., Donadei, V., Hauer, L., Naga, A., & Vollmer, D. (2020). Capillary Balancing: Designing Frost-Resistant Lubricant-Infused Surfaces. *Nano Letters*, 20(12), 8508–8515. <https://doi.org/10.1021/acs.nanolett.0c02956>

Working Group 1 of the Joint Committee for Guides in Metrology. (2008). *Evaluation of measurement data - Guide to the expression of uncertainty in measurement* (1st ed., Issue 100:2008). <http://www.bipm.org/en/publications/guides/gum.html>

Yang, G., Guo, K., & Li, N. (2011). Freezing mechanism of supercooled water droplet impinging on metal surfaces. *International Journal of Refrigeration*, 34(8), 2007–2017. <https://doi.org/10.1016/j.ijrefrig.2011.07.001>

-
- Yeong, Y. H., Milionis, A., Loth, E., & Sokhey, J. (2018). Self-lubricating icephobic elastomer coating (SLIC) for ultralow ice adhesion with enhanced durability. *Cold Regions Science and Technology*, 148(December 2017), 29–37. <https://doi.org/10.1016/j.coldregions.2018.01.005>
- Young, T. (1805). III. An essay on the cohesion of fluids. *Philosophical Transactions of the Royal Society of London*, 95, 65–87. <https://doi.org/10.1098/rstl.1805.0005>
- Zhang, J., Wang, A., & Seeger, S. (2014). Nepenthes Pitcher Inspired Anti-Wetting Silicone Nanofilaments Coatings: Preparation, Unique Anti-Wetting and Self-Cleaning Behaviors. *Advanced Functional Materials*, 24(8), 1074–1080. <https://doi.org/10.1002/adfm.201301481>
- Zhuo, Y., Xiao, S., Amirfazli, A., He, J., & Zhang, Z. (2021). Polysiloxane as icephobic materials – The past, present and the future. *Chemical Engineering Journal*, 405(September 2020), 127088. <https://doi.org/10.1016/j.cej.2020.127088>
- Zimmermann, J., Artus, G. R. J. J., & Seeger, S. (2008). Superhydrophobic Silicone Nanofilament Coatings. *Journal of Adhesion Science and Technology*, 22(3–4), 251–263. <https://doi.org/10.1163/156856108X305165>
- Zimmermann, J., Artus, G. R. J., & Seeger, S. (2007). Long term studies on the chemical stability of a superhydrophobic silicone nanofilament coating. *Applied Surface Science*, 253(14), 5972–5979. <https://doi.org/10.1016/j.apsusc.2006.12.118>
- Zimmermann, J., Rabe, M., Artus, G. R. J., & Seeger, S. (2008). Patterned superfunctional surfaces based on a silicone

nanofilament coating. *Soft Matter*, 4(3), 450–452.
<https://doi.org/10.1039/b717734h>

Zimmermann, J., Reifler, F. A., Fortunato, G., Gerhardt, L.-C., & Seeger, S. (2008). A Simple, One-Step Approach to Durable and Robust Superhydrophobic Textiles. *Advanced Functional Materials*, 18(22), 3662–3669.
<https://doi.org/10.1002/adfm.200800755>

Zimmermann, J., Reifler, F. A., Schrade, U., Artus, G. R. J., & Seeger, S. (2007). Long term environmental durability of a superhydrophobic silicone nanofilament coating. *Colloids and Surfaces A: Physicochemical and Engineering Aspects*, 302(1–3), 234–240. <https://doi.org/10.1016/j.colsurfa.2007.02.033>

Zimmermann, J., Seeger, S., Artus, G., & Jung, S. (2004). *Superhydrophobic Coating* (Patent No. WO 2004/113456 A2). World Intellectual Property Organization.

Zisman, W. A. (1964). Relation of the Equilibrium Contact Angle to Liquid and Solid Constitution. In F. M. Fowkes (Ed.), *Contact Angle, Wettability, and Adhesion* (43rd ed., pp. 1–51). American Chemical Society. <https://doi.org/10.1021/ba-1964-0043.ch001>

Appendix A - Determination of Thermal Stress in the Ice Adhesion Test

A.1 Context:

The phase change of water from liquid to solid is an exothermic process. An impacting supercooled droplet will locally increase its temperature before cooling down to the ambient temperature, thus releasing heat into the surface. For a microdroplet, the heat transfer is negligible, but for a high frequency of droplet impacts over an entire surface area, the effect can be noticeable. The presence or absence of a supercooled droplet cloud can therefore influence the temperature of a substrate in an airflow. What is the effect, then of a change in temperature on an iced substrate?

A strain gauge mounted to the back of the cantilever is sensitive to temperature change due to the thermal expansion of the substrate. On a bi-material substrate where the coefficients of thermal expansion of both materials are unequal, the substrate will tend to bend, which is also detected by a strain gauge.

A.2 Results:

Following ice accretion, on a lubricant-infused surface, bending due to thermal contraction leads to ice delamination. Initially, once the icing cloud has stopped, a sudden increase in strain was detected, indicating contraction of the ice relative to the substrate. The strain steadily decreased until a sudden drop, indicating relaxation of bending due to partial interfacial separation. The steady drop in strain is explained by the force from aerodynamic drag. The more the substrate tends to bend, the higher the aerodynamic drag force resisting it. The constraint caused by aerodynamic drag resulted in interfacial stress, and eventual delamination.

The accretion of impact ice onto an unheated surface is a complex heat-transfer problem. Impacting droplets carry with them some kinetic energy, but due to their small mass, that quantity can be negligible. When they impact, they begin to solidify. The phase

change releases heat to the environment, mostly by conduction to the surface on which they impact. That heat is also lost by convective cooling due to airflow. The effect is multiplied by the rate of supercooled droplet impact. If the impact of supercooled droplets is suddenly stopped, then the main contributor to heat input into the system is lost, resulting in a sudden drop in temperature albeit small.

From the instant supercooled water solidifies, it begins to cool to the ambient temperature. This cooling is inhibited by heat input from subsequent impacting supercooled water droplets, but if that flux is stopped, then the ice is free to cool to the ambient temperature. In the icing setup used in this study, the substrates were metallic. The thermal mismatch between ice and the metal substrate produced a bending moment as the temperature changed. For decreasing temperature, ice will tend to contract nearly twice as much as aluminum, resulting in measurable bending. If the adhesion strength between a substrate and ice is very low, as was the case with lubricant-infused surfaces, thermal contraction could lead to spontaneous ice detachment.

Figure 53 shows an example of the progression of strain on a titanium substrate coated with silicone nanofilaments during mixed/rime icing conditions. At the beginning of ice accretion, a sudden increase in strain was detected. An increase in strain is indicative of an increase in temperature. The heat added to the substrate comes mostly from the latent heat of fusion of the impacting supercooled microdroplets. As the ice thickness increases, the heat transfer front gets further from the substrate, allowing the bare side where the strain gauge is to cool and shrink. When the icing cloud is suddenly stopped, another sudden jump in strain was measured. This jump also came from a temperature change, as the first one had, but instead of an increase in temperature, it decreased. The reason that the strain increased with decreasing temperature was due to the coefficient of thermal expansion mismatch between

ice and titanium. During the four test runs plotted in Figure 53, thermal bending was insufficient to initiate ice delamination.

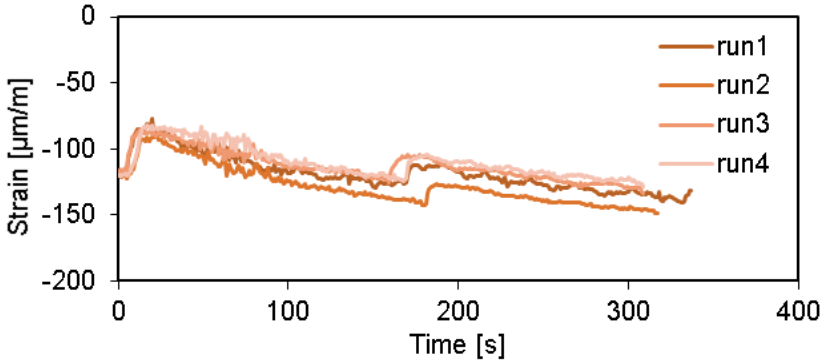


Figure 53: Strain progression during mixed/rime ice accretion on a titanium substrate coated with silicone nanofilaments. Time starts when the icing cloud was introduced into the airflow.

The thermal effects discussed in Figure 53 were also present in Figure 54. The difference in the two scenarios was only in the type of coating; in Figure 54 the surface was infused with silicone oil. Soon after the thermal bending effect at 200s, there was a sudden drop in strain reading, indicative of relaxation from a pre-stressed state, specifically, partial delamination of ice. As the iced beam cooled, the curvature increased, but it was being pushed back by aerodynamic drag. This constraint meant that the interfacial stress was increasing the more the iced beam cooled. When the temperature reached a certain point, the interfacial stress was sufficient to initiate partial delamination of the ice. Using the difference in strain between when the ice accretion stopped, to the point where delamination happened, one can calculate the interfacial shear stress at the moment of delamination, yielding an ice adhesion strength. This method of analysis was used for the results in Section 4.9.2.

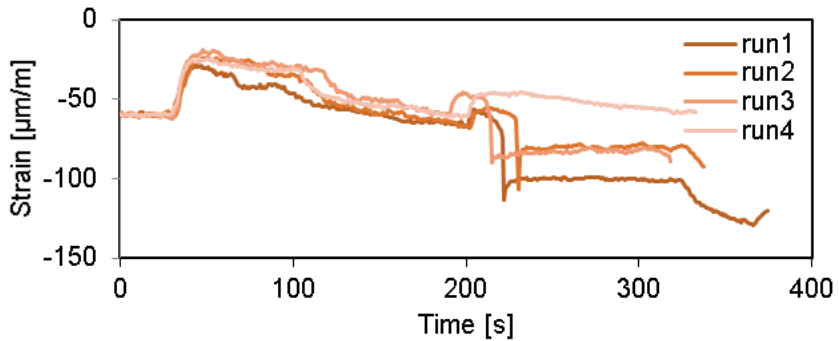


Figure 54: Strain progression during mixed/rime ice accretion on a titanium substrate coated with silicone nanofilaments infused with silicone oil. Time starts when the icing cloud was introduced into the airflow.

A.3 Summary:

Lubricant-infused surfaces had such low adhesion strength to ice, that ice peeled off without forced vibration of the cantilever. An understanding of the temperature fluctuation between ice accretion and forced vibration in the testing protocol revealed that the ice adhesion strength could still be determined by strain measurement.